
CMS Internal Note

The content of this note is intended for CMS internal use and distribution only

Technical Proposal

A GEM Detector System for an Upgrade of the CMS Muon Endcaps

Submitted to CMS upgrade committee for approval
February 10, 2012

Contact person: Archana Sharma (archana.sharma@cern.ch)
on behalf of the GEM Collaboration (GEMs for CMS)*

* For this document the author list has been broadened to include collaborators who support the proposal and may join the project in future, while the structure and size of the collaboration that has carried out the feasibility studies so far is described in Section 10.

D. Abbaneo¹⁾, M. Abbrescia²⁾, I. Ahmed¹⁾, W. Ahmed⁴⁾, M. Alfonsi¹⁾, T. Andrzejewski⁶⁾, C. Armaingaud¹⁾, M. I. Asghar⁴⁾, Y. Assran⁵⁾, P. Aspell¹⁾, A. d'Auria¹⁾, C. Avila³⁾, I. Awan⁴⁾, M. G. Bagliesi⁷⁾, S. Bally¹⁾, Y. Ban⁸⁾, S. Banerjee⁹⁾, D. Bartkiewicz⁶⁾, L. Benussi¹⁰⁾, A. C. Benvenuti¹¹⁾, U. Berzano¹⁾, A. Bhardwaj³⁴⁾, V. Bhatnagar¹²⁾, S. Bhattacharya⁹⁾, P. Bhattacharya⁹⁾, A. Bhattacharyya¹³⁾, H. Bialkowska¹⁴⁾, S. Bianco¹⁰⁾, B. Boimska¹⁴⁾, R. Boniecki⁶⁾, J. Bos¹⁾, O. Bouhali¹⁵⁾, G. Brona⁶⁾, K. Bunkowski¹⁾, S. Buontempo¹⁶⁾, J. Cai⁸⁾, R. Cecchi⁷⁾, J. P. Chatelain¹⁾, J. Christiansen¹⁾, S. Colafranceschi¹⁰⁾, A. Colaleo²⁾, A. Conde Garcia¹⁾, T. Cornelis¹⁷⁾, G. Croci¹⁾, I. Crotty¹⁾, M. Cwiok⁶⁾, H. Czyrkowski⁶⁾, M. Dallavalle¹¹⁾, E. David¹⁾, R. De Oliveira¹⁾, G. de Robertis²⁾, S. Dildick¹⁷⁾, A. Dimitrov¹⁸⁾, W. Dominik⁶⁾, W. van Doninck¹⁹⁾, K. Doroba⁶⁾, D. Druzhkin¹⁾, S. Duarte Pinto¹⁾, F. Fabbri¹¹⁾, S. Ferry¹⁾, F. Formenti¹⁾, L. Franconi¹⁾¹¹⁾, T. Frueboes¹⁴⁾, A. Gaddi¹⁾, K. Gnanvo²⁰⁾²¹⁾, B. Gómez³⁾, M. Gorski¹⁴⁾, R. Guida¹⁾, S. Guragain²³⁾, A. Gutierrez²⁴⁾, R. Hadjiiska¹⁸⁾, K. Hoepfner²⁶⁾, M. Hohlmann²⁰⁾, H. Hoorani⁴⁾, G. Iaselli²⁾, C. Jiang²⁷⁾, A. Kalinowski⁶⁾, A. Y. E. Kamel²²⁾, P. E. Karchin²⁴⁾, M. Kazana¹⁴⁾, V. Khotilovich²⁵⁾, K. Kierzkowski⁶⁾, M. Konecki⁶⁾, A. Kotarba¹⁾, V. Kozhuharov¹⁸⁾, J. Krolikowski⁶⁾, M. I. Kudla¹⁴⁾, A. Kumar³⁴⁾, S. Lami⁷⁾, G. De Lentdecker²⁹⁾, W. Li⁸⁾, L. Lista¹⁶⁾, L. Litov¹⁸⁾, F. Loddo²⁾, M. Mackowski⁶⁾, G. Magazzù⁷⁾, M. Maggi²⁾, N. Majumdar⁹⁾, A. Marchioro¹⁾, A. Marinov¹⁷⁾, S. Martou¹⁾, K. Mehta¹⁾, J. Merlin¹⁾, M. Misiura⁶⁾, A. K. Mohanty¹³⁾, A. Mohapatra³⁰⁾, A. Montanari¹¹⁾, T. Moulik³⁰⁾, S. Muhammad⁴⁾, S. Mukhopadhyay⁹⁾, H. Muller¹⁾, M. Naimuddin³⁴⁾, F. L. Navarria¹¹⁾, K. Nawrocki¹⁴⁾, K. Nesteruk⁶⁾, K. Niemkiewicz⁶⁾, S. Nuzzo²⁾, L. Obara⁶⁾, P. Olejniczak⁶⁾, E. Oliveri⁷⁾, A. Osorio³⁾, L. M. Pant¹³⁾, P. Paolucci¹⁶⁾, N. Parashar²³⁾, S. Park³¹⁾, B. Pavlov¹⁸⁾, P. Petkov¹⁸⁾, D. Piccolo¹⁰⁾, M. Pietrusinski⁶⁾, H. Postema¹⁾, K. Pozniak⁶⁾, G. Pugliese²⁾, S. Qian⁸⁾, A. Radi³²⁾, G. Raffone¹⁰⁾, A. Ranieri¹⁾, K. Ranjan³⁴⁾, A. Rodrigues¹⁾, K. Romanowska-Rybinska¹⁴⁾, L. Ropelewski¹⁾, D. Rybka¹⁴⁾, A. Safonov²⁵⁾, Z. Salapa⁶⁾, J. Samarati¹⁾, J. C. Sanabria³⁾, G. Saviano¹⁰⁾, A. Scribano⁷⁾, H. Shahzad⁴⁾, A. Sharma¹⁾, R. K. Shivpuri³⁴⁾, G. Siemczuk⁶⁾, J. B. Singh¹²⁾, N. Smiljkovic¹⁾, A. Smykiewicz⁶⁾, W. Snoeys¹⁾, M. J. Staib²⁰⁾, M. van Stenis¹⁾, M. Szleper¹⁴⁾, H. Taureg¹⁾, H. Teng⁸⁾, R. G. Thomas¹³⁾, P. Tropea¹⁾, S. A. Tuppiti²⁾³³⁾, N. Turini⁷⁾, M. Tytgat¹⁷⁾, E. Verhagen²⁹⁾, M. Villa¹⁾, P. Vitulo²⁸⁾, M. Wolszczak⁶⁾, G. Wrochna¹⁴⁾, Y. Yang²⁹⁾, L. Yuanjing³⁵⁾, L. Yulan³⁵⁾, W. Zabolotny⁶⁾, N. Zaganidis¹⁷⁾, P. Zalewski¹⁴⁾, M. Zielenkiewicz⁶⁾, M. Zientek¹⁾.

1) CERN, Geneva, Switzerland.

2) Politecnico di Bari, Università di Bari, and INFN Sezione di Bari, Bari, Italy.

3) Universidad de los Andes (UNIANDÉS), Bogotá, Colombia.

4) National Center for Physics, Quaid-i-Azam University Campus, Islamabad, Pakistan.

5) Suez Canal University, Suez, Egypt.

6) Institute of Experimental Physics, Faculty of Physics, University of Warsaw, Poland.

7) Università di Siena and INFN Sezione di Pisa, Pisa, Italy.

8) Peking University, Beijing, China.

9) Saha Institute of Nuclear Physics (SINP), Kolkata, India.

10) Laboratori Nazionali di Frascati (LNF) INFN, Frascati, Italy.

11) Università di Bologna and INFN sezione di Bologna, Italy.

12) Department of Physics, Panjab University Chandigarh, India.

13) Bhabha Atomic Research Center (BARC), Mumbai, India.

14) National Centre for Nuclear Research, Otwock-Swierk, Poland.

15) Texas A&M University at Qatar, Doha, Qatar.

16) INFN, Sezione di Napoli, Napoli, Italy.

17) Department of Physics and Astronomy, Ghent University, Ghent, Belgium.

18) University of Sofia, Sofia, Bulgaria.

19) Vrije Universiteit Brussel, Brussel, Belgium.

20) Florida Institute of Technology, Melbourne, USA.

21) University of Virginia, Department of Physics, Charlottesville, USA.

22) Cairo University, Cairo, Egypt.

23) Purdue University, Calumet, USA.

24) Wayne State University, Detroit, USA.

25) Texas A&M University, Department of Physics and Astronomy, College Station, Texas, USA.

26) RWTH Aachen, III. Physics Institute, Aachen, Germany.

27) Institute of High Energy Physics, China.

28) University of Pavia and INFN Pavia, Pavia, Italy.

29) Université Libre de Bruxelles, Bruxelles, Belgium.

30) NISER, Bhubaneswar, India.

31) KODEL, Korea University, Seoul, South Korea.

32) Ain Shams University, Cairo, Egypt.

33) now at Universitaet Zurich, Switzerland.

34) Department of Physics, University of Delhi, India.

35) The Engineering Physics Dept, Tsinghua University.

Abstract

This technical proposal aims at instrumenting the $1.6 < |\eta| < 2.4$ region of the CMS forward muon system with a Gas Electron Multiplier (GEM) detector system to enhance the muon tracking and triggering capabilities of CMS in the high-luminosity conditions expected after the second long LHC shutdown (LS2). Currently, the $|\eta| > 1.6$ region of the muon endcaps is not instrumented with any of the Resistive Plate Chambers (RPCs) that were originally foreseen in the CMS Technical Design Report; it is proposed to instrument this vacant space with Triple-GEM detectors.

For the last two years, an international collaboration of CMS institutions has been studying the expected GEM detector performance and its impact on future physics capabilities with muons in CMS. The collaboration has been evaluating the technological feasibility of such an upgrade with detector prototypes and simulations. The results presented here show that a system with Triple-GEM detectors is a near ideal answer to the stringent muon tracking and triggering requirements in the expected hostile post-LS2 environment. This is due to the good position and time resolutions, high rate capability, and radiation hardness of these micropattern gas detectors.

Specifically, feasibility and performance studies for two GEM stations (GE1/1 and GE2/1) installed on the YE1 yoke disk are presented. The design, construction, and performance of small and full-scale trapezoidal Triple-GEM prototypes is described. Results on efficiency, space and time resolutions of these prototypes from detector simulations, laboratory measurements, and muon/pion beam tests including measurements in a magnetic field demonstrate a performance fully adequate for the high background environment expected in the CMS muon endcaps during the high-luminosity LHC phase. Preliminary studies on the extension of an RPC-like trigger into $|\eta| > 1.6$ using a GEM system show significant sharpening of trigger turn-on curves and improved trigger effectiveness compared with an RPC-only trigger.

Based on these results, a baseline CMS Triple-GEM detector is proposed in detail for the upgrade. Large-scale chamber production scenarios are discussed, followed by integration and installation studies given the existing CMS muon high- η envelope. The needed technical services have been studied and the preliminary understanding of cooling, cabling and gas distribution is presented. An initial design of on- and off-detector electronics for the readout of the GEM detector system is presented with a schedule for design and production. Project schedule and milestones towards installation in LS2 (2017/2018) are projected; a budget draft and an outlay of resources are presented. The organisational structure of the collaboration that proposes to take on this project is discussed.

Given the success of the feasibility studies and with the organisation of the GEM Collaboration in place, the project is ready to move ahead. Consequently, formal review and approval by CMS are requested. This will permit the project to be integrated into the official CMS upgrade program enabling the participating institutions to approach their respective national agencies with funding requests for the project.

Contents

1	Endcap muon system	9
1.1	Introduction	9
1.2	CSC (Cathode Strip Chambers)	9
1.3	RPC (Resistive Plate Chambers)	10
1.4	Muon system redundancy and extension up to $\eta = 2.4$	10
1.5	Performance requirements for high- η muon detectors	10
1.6	Present experience with MPGDs in experiments	11
1.7	High- η muon detectors proposed for LS2 (2017-2018)	12
2	Impact of high-η upgrade on muon reconstruction	15
2.1	Muon system redundancy and extension up to $\eta = 2.4$	15
2.2	Multiple scattering	16
2.3	Muon track reconstruction	17
3	Studies of small and full-scale GEM prototypes	20
3.1	Initial prototypes for choosing among MPGD technologies	20
3.2	Triple-GEM prototypes	20
3.3	Single-mask GEM production technology	21
3.4	Test beam measurements	21
3.4.1	Data analysis and results	22
3.4.2	Standard double-mask Triple-GEM	22
3.4.3	Single-mask Triple-GEM	24
3.4.4	Performance summary for small prototypes	24
3.5	Full-size Triple-GEM prototype	25
3.5.1	Prototype description	25
3.5.2	Test beam setups	26
3.5.3	Prototype performances in beam test	28
3.5.4	Conclusion from measurements with full-size prototypes	31
3.6	Present status and improved detector assembly technique	31
4	Simulation studies	35
4.1	The GEM detector	35
4.2	Study of the transport parameters	36
4.3	Gain studies	38
4.4	Avalanche simulation	39
5	Muon triggering with GEM detectors in the high-η region	43
5.1	Trigger emulation	43
5.2	GEM geometry	44

5.3	Simulated chamber properties	45
5.4	Results	45
5.5	Assembly laboratory (TIF - Tracker Integration Facility, building 186)	53
5.6	Production of GEM foils and assembly of GE1/1 detector	54
6	Electronics system	56
6.1	Introduction	56
6.2	On-detector electronics	56
6.2.1	The GEM chamber (from an electrical perspective)	56
6.2.2	The front-end ASIC development - VFAT2 to VFAT3 and GdSP	57
6.3	Off-detector electronics	60
6.4	System considerations	62
6.4.1	General system view	62
6.4.2	Segmentation	63
6.4.3	Electronics power consumption for a 3·10 chamber.	63
6.5	Project planning	63
6.6	Cost:	65
6.6.1	On-detector costs	65
6.6.2	Off-detector: components for a μ TCA crate	66
6.6.3	GE1/1 system cost estimate (on and off-detector)	67
7	Cooling, gas and cabling services	68
7.1	Gas	68
7.2	Cooling	69
8	Schedule and milestones toward GE1/1 and 2/1 installation in LS2	73
9	Budget and resources	75
10	Collaboration structure	77
11	Summary and conclusion	79
12	Publications	80
13	Conference contributions	80
	Appendices	84
A	Parameters describing the GEi/1 systems	85
B	Integration and installation within CMS high-η envelope	87
B.1	Scope	87

B.2	General description	87
B.3	Documents	87
B.3.1	Applicable documents	88
B.3.2	Drawings	88
B.3.3	Reference documents	88
B.3.4	Super-chamber characteristics	88
B.3.5	Super-chambers referential definition	88
B.3.6	Envelope and location	89
B.3.7	Assembly sequence of a chamber	89
B.4	Assembly and installation	89
B.5	Preliminary considerations GE2/1	90
C	Project organization	91
C.1	Project organization for retrieval & DB	91
C.2	Task(s)	91
C.3	Electronics system	91
C.4	Product(s) involved	92
D	Full simulation results for trigger studies with GEM	93

List of Figures

1	CMS transverse section showing the existing gaseous detector for muon tracking and triggering namely RPCs, DTs and CSCs and the locations of the proposed GEM detectors GE1/1 and GE2/1.	9
2	The CMS Endcap YE1 disk showing the “nose”, namely the high- η region.	13
3	CATIA model of the CMS endcap structure for GE1/1 chambers (top) and GE2/1 Chambers (bottom). For the GE1/1 station the chambers will be installed on the YE1 “nose”. For the GE2/1 station, which sits exactly on the backside of YE1 “nose”, there will be two sets of chambers long and short due to the neutron shielding that sits between $2.1 < \eta < 2.4$. Since there is room for long chambers in z, the 2/1 station offers 4 measurements points from eta $1.6 < \eta < 2.1$ and two measurements points from $2.1 < \eta < 2.4$.	14
4	Muon momentum resolution as a function of momentum for barrel (a), overlap (b), and endcap (c) regions using the muon system only (blue), the inner tracking only (green) and both system together (red).	15
5	MultipleScattering	16
6	HitTrackResiduals	17
7	MomResSummary	18
8	GEMTracking	19
9	The standard double-mask Triple-GEM prototype. Left: Detector during assembly. Right: Configuration of gaps between electrodes.	20
10	Overview of single-mask etching process for GEM foils.	21
11	Positions of small Triple-GEM prototypes (green) within the RD51 beam telescope during tests at the CERN SPS H4 beam line. The Triple-GEMs of the telescope are labeled “Tracker GEM”.	22
12	Beam profiles for muons and pions obtained with the tracker GEMs in the beam telescope.	22
13	Residual distribution for the standard Triple-GEM, fitted with a Gaussian of the form $p_0 \cdot \exp(-0.5 \cdot ((x - p_1)/p_2)^2)$, plus a first-order polynomial of the form $p_3 + p_4 \cdot x$ to account for noise hits.	23
14	Detector efficiency (left) and strip cluster size (right) for the standard Triple-GEM with different gas mixtures and gap size configurations.	23
15	Detector timing resolution as function of the induction field (left) and drift field (right) for the standard Triple-GEM with different gas mixtures and gap size configurations.	23
16	VFAT2 threshold scan for the standard Triple-GEM with the 3/1/2/1 mm gap size configuration and Ar/CO ₂ /CF ₄ (45:15:40) gas mixture.	24
17	Detector efficiency (left) and strip cluster size (right) for the single-mask Triple-GEM.	25
18	The first prototype of a full-size Triple-GEM detector for CMS. Left: Completed detector. Right: Glueing of spacer frames during detector assembly.	25
19	(a) Exploded view of the first full-size Triple-GEM prototypes for CMS. (b) Electrode layout and gap size configurations of the two full-size prototypes GE1/1-I (left) and GE1/1-II (right).	26
20	Assembly procedure of the full-size CMS prototypes: (a) foil stretching in the oven; (b) glueing the spacer frames; (c) curing the glue; (d) mounting the readout plane.	27
21	Gain curve for the GE1/1-I measured with x-rays in the RD51 lab.	27
22	(a) The GE1/1-I detector installed in the SPS H4 beam line. (b) The GE1/1-II detector installed inside the CMS M1 magnet at the SPS H2 beam line.	28
23	The RD51 telescope used during all test beams at the RD51 H4, H6, and H8 beam area.	28
24	Typical muon beam profile obtained with tracker GEM detectors.	29

25	Results obtained with GE1/1-I during the Oct. 2010 test beam campaign: (a) residual distribution; (b) detector hit efficiency as function of the current in the HV divider, which is proportional to the electric fields in the GEM.	29
26	GE1/1-II performance: cluster size (left) and space resolution (right) at high and low η measured with VFAT2 binary electronics.	29
27	GE1/1-II efficiency performance at high and low η ends. Efficiency reaches 96.5% at gain 7000.	30
28	Results for GE1/1-II using pulse height measurements with APV25/SRS during the Aug. 2011 test beam campaign: (a) strip cluster size distribution; (b) difference Δx between hit positions measured with GE1/1-II and with a reference GEM in the tracker.	30
29	Left: Δy distribution for TR_5 and TR_1 . Right: Δx distribution for TR_5 and GE1/1-II using central tracks in a pion beam.	30
30	Left: GE1/1-II cluster sizes inside a strong magnetic field. Right: Comparison of measured and simulated strip cluster position displacement in GE1/1-II due to an external magnetic field.	31
31	The <i>self-stretching</i> Triple-GEM assembly technique: (a) GEM foil before assembly; (b) external frame for foil stretching; (c) mounting the GEM foils; (d) stretching the foils; (e) stretched GEM; (f) completed detector including readout board.	32
32	Gain curve of the 30 cm \times 30 cm self-stretched GEM prototype detector.	33
33	The electric field as seen in Garfield at the center of the GEM	35
34	Exploded view of a Triple-GEM arrangement (Distances are not to scale)	36
35	Diffusion coefficient for two different gas mixtures under study in presence of magnetic field and with angle $\theta(E, B) = 8^\circ$	37
36	Diffusion coefficients for magnetic fields = 0T and 3T with $\theta(E, B) = 90^\circ$	37
37	Lorentz angles for the gas mixture Ar/CO ₂ /CF ₄ for the angles $\theta(E, B) = 8^\circ$ (left) and $\theta(E, B) = 90^\circ$ (right) for a magnetic field of 3 T.	38
38	The drift velocities for various gas mixtures from simulation and the experimental values from LHCb studies. The simulation shows a good agreement with the experimental results	38
39	Loss rate for primary electrons for $r_p = 0.6$. The losses occur due to attachment to the quencher gas molecules (left) and due to the electrons hitting the surface of copper metal or polyimide walls (right)	39
40	Loss rate for secondary electrons. The losses occur due to attachment to the quencher gas molecules (left) and due to the electrons hitting the surface of copper metal or polyimide (right)	40
41	Overall Loss rate for primary (left) and secondary (right) electrons for penning parameter $r_p = 0.6$	40
42	Effective gain (G_{eff}) and the total gain (G_{tot}) for different penning parameters.	41
43	Effective gain comparison for Ar/CO ₂ /CF ₄ and Ar/CO ₂ for penning parameter of 0.6	41
44	Triple-GEM effective gain compared with data	42
45	Time resolution for single electrons in the case of Ar/CO ₂ /CF ₄ (left) and Ar/CO ₂ (right)	42
46	Longitudinal view of the current RPC trigger towers in one quadrant of the CMS detector. Chambers in areas marked with green (RE1/1, RE2/1) were modified to have increased number of strips to simulate the use of GE1/1 and GE2/1 GEM stations in those locations.	44
47	Simulated L1 GEM+RPC trigger output rates summed over trigger towers -16 to -13 and 13 to 16 vs. p_T cut for ideal chamber model (top left: base, top right: 2 \times , bottom left: 4 \times , bottom right: 8 \times strip granularity).	46
48	Simulated L1 GEM+RPC trigger output rates summed over trigger towers -16 to -13 and 13 to 16 vs. p_T cut for realistic chamber model (top left: base, top right: 2 \times , bottom left: 4 \times , bottom right: 8 \times strip granularity).	47

49	Simulated total L1 GEM+RPC trigger output rates as function of different geometries for ideal (left) and realistic (right) chamber models. Rows correspond to three different p_T thresholds of 16, 50, and $140 \frac{\text{GeV}}{c}$. Only the contribution from muon candidates of quality 1 or 2 is shown.	48
50	L1 GEM+RPC trigger efficiency curves in trigger tower 13 for base geometry. Rows correspond to 3 different p_T thresholds of 16, 50, and $140 \frac{\text{GeV}}{c}$, respectively. Left column shows results for ideal chamber model, right for realistic chamber model.	49
51	L1 GEM+RPC trigger efficiency curves in trigger tower 13 for $2\times$ geometry. Rows correspond to 3 different p_T thresholds of 16, 50, and $140 \frac{\text{GeV}}{c}$, respectively. Left column shows results for ideal chamber model, right for realistic chamber model.	50
52	L1 GEM+RPC trigger efficiency curves in trigger tower 13 for $4\times$ geometry. Rows correspond to 3 different p_T thresholds of 16, 50, and $140 \frac{\text{GeV}}{c}$, respectively. Left column shows results for ideal chamber model, right for realistic chamber model.	51
53	L1 GEM+RPC trigger efficiency curves in trigger tower 13 for $8\times$ geometry. Rows correspond to 3 different p_T thresholds of 16, 50, and $140 \frac{\text{GeV}}{c}$, respectively. Left column shows results for ideal chamber model, right for realistic chamber model.	52
54	Building 186 view.	53
55	TIF clean room view.	53
56	TIF gas system.	54
57	New building 107.	54
58	Block diagram showing the main components of an electronic control and readout system suitable for GEMs within CMS.	56
59	Strip dimensions for GEM prototype GE1/1.	57
60	The electrical characteristics of GEM prototype GE1/1.	57
61	VFAT2, A 128 channel front-end ASIC with trigger and tracking capabilities. This ASIC is currently used for the prototype systems.	58
62	The VFAT2 architecture, shown for 1 channel.	58
63	VFAT3 architecture.	59
64	Gdsp architecture.	60
65	Off-detector Electronics option using the current RPC PAC trigger.	61
66	Off-detector Electronics option using new AMC GEM Trigger Boards (GemTB).	61
67	Block diagram for the electronics system (control and readout) as foreseen for the CMS forward high- η region.	62
68	The GEM segmentation into columns and eta partitions.	63
69	Time line for the front-end ASIC development and readout systems.	65
70	Layout of the mixer unit.	68
71	Layout of the pump compressor.	70
72	Layout of the gas distribution rack.	71
73	Endcap cooling system.	71
74	Endcap cooling system, main manifolds.	72
75	Endcap cooling system layout.	72
76	Schedule and milestone for GE1/1 and GE2/1, construction, installation and project.	74
77	Current organigram of the proto-collaboration.	77

78	According to the integration studies there is enough space to insert a sandwich of two Triple-GEM detectors (Super-Chamber).	88
79	Installation sequence studies.	89
80	L1 GEM+RPC trigger efficiency curves in trigger tower 14 for base geometry. Rows correspond to 3 different p_T thresholds of 16, 50, and $140 \frac{\text{GeV}}{c}$, respectively. Left column shows results for ideal chamber model, right for realistic chamber model.	93
81	L1 GEM+RPC trigger efficiency curves in trigger tower 14 for $2\times$ geometry. Rows correspond to 3 different p_T thresholds of 16, 50, and $140 \frac{\text{GeV}}{c}$, respectively. Left column shows results for ideal chamber model, right for realistic chamber model.	94
82	L1 GEM+RPC trigger efficiency curves in trigger tower 14 for $4\times$ geometry. Rows correspond to 3 different p_T thresholds of 16, 50, and $140 \frac{\text{GeV}}{c}$, respectively. Left column shows results for ideal chamber model, right for realistic chamber model.	95
83	L1 GEM+RPC trigger efficiency curves in trigger tower 14 for $8\times$ geometry. Rows correspond to 3 different p_T thresholds of 16, 50, and $140 \frac{\text{GeV}}{c}$, respectively. Left column shows results for ideal chamber model, right for realistic chamber model.	96
84	L1 GEM+RPC trigger efficiency curves in trigger tower 15 for base geometry. Rows correspond to 3 different p_T thresholds of 16, 50, and $140 \frac{\text{GeV}}{c}$, respectively. Left column shows results for ideal chamber model, right for realistic chamber model.	97
85	L1 GEM+RPC trigger efficiency curves in trigger tower 15 for $2\times$ geometry. Rows correspond to 3 different p_T thresholds of 16, 50, and $140 \frac{\text{GeV}}{c}$, respectively. Left column shows results for ideal chamber model, right for realistic chamber model.	98
86	L1 GEM+RPC trigger efficiency curves in trigger tower 15 for $4\times$ geometry. Rows correspond to 3 different p_T thresholds of 16, 50, and $140 \frac{\text{GeV}}{c}$, respectively. Left column shows results for ideal chamber model, right for realistic chamber model.	99
87	L1 GEM+RPC trigger efficiency curves in trigger tower 15 for $8\times$ geometry. Rows correspond to 3 different p_T thresholds of 16, 50, and $140 \frac{\text{GeV}}{c}$, respectively. Left column shows results for ideal chamber model, right for realistic chamber model.	100
88	L1 GEM+RPC trigger efficiency curves in trigger tower 16 for base geometry. Rows correspond to 3 different p_T thresholds of 16, 50, and $140 \frac{\text{GeV}}{c}$, respectively. Left column shows results for ideal chamber model, right for realistic chamber model.	101
89	L1 GEM+RPC trigger efficiency curves in trigger tower 16 for $2\times$ geometry. Rows correspond to 3 different p_T thresholds of 16, 50, and $140 \frac{\text{GeV}}{c}$, respectively. Left column shows results for ideal chamber model, right for realistic chamber model.	102
90	L1 GEM+RPC trigger efficiency curves in trigger tower 16 for $4\times$ geometry. Rows correspond to 3 different p_T thresholds of 16, 50, and $140 \frac{\text{GeV}}{c}$, respectively. Left column shows results for ideal chamber model, right for realistic chamber model.	103
91	L1 GEM+RPC trigger efficiency curves in trigger tower 16 for $8\times$ geometry. Rows correspond to 3 different p_T thresholds of 16, 50, and $140 \frac{\text{GeV}}{c}$, respectively. Left column shows results for ideal chamber model, right for realistic chamber model.	104

List of Tables

1	Performance requirements in the various η sectors.	11
2	Overview of all GEM detector prototypes that were constructed and studied in this project.	33
3	Performance overview for all tested prototypes.	34
4	Summary table which lists quantities and deliveries	55
5	Summary table	63
6	Power estimate for the main components of a single chamber with 3·10 segmentation.	64
7	Silicon fabrication cost estimated for different elements and phases.	64
8	Silicon fabrication cost of an MPW run and an engineering run in this process.	65
9	Estimated costs of the electronics components for a single chamber	66
10	Estimated costs of the electronics components for a super chamber.	66
11	Cost of the off-detector components	66
12	Estimated costs of the off-detector electronics components for a 30° sector equipped with single GEM chambers.	67
13	Estimated costs of the off-detector electronics components for a 30° sector equipped super chambers.	67
14	Estimated costs of the electronics components for a super chamber.	67
15	Estimated costs of the electronics components for a super chamber.	67
16	Summary of the new and existing modules needed for the CMS-GEM gas system.	69
17	Summary of milestones.	73
18	Budget and resources based on previous experience. We have considered approximately 2.2 MCHF for the electronics; this includes approximately 522 kCHF for the front-end ASIC silicon cost.	76
19	GE1/1 Mechanics	85
20	GE1/1 Electronics	85
21	GE1/1 System overview	85
22	GE2/1 Mechanics	86
23	GE2/1 Electronics	86
24	GE2/1 System overview	86
25	System overview: Endcap disks 1	87
26	System overview: Endcap 2	87
27	System overview: Endcap 3	87
28	System overview: Endcap 4	88
29	System overview: Dimensions	88

1 Endcap muon system

1.1 Introduction

The CMS muon system[1] is designed to provide robust, redundant and fast identification of the muons traversing the system, in addition to trigger capabilities and momentum measurement. One of the main goals during the upgrade phases will be to have a detector capable of fully exploiting the increased LHC performance, and sustaining reliable operation for at least ten years.

Here a big challenge arises, coming from the higher luminosity and more hostile conditions, in particular in terms of expected rates and backgrounds in near future. The high instantaneous luminosity can confuse the CMS Level-1 trigger. To keep up with the 40 MHz rate, this uses partial data from events in each beam crossing and dedicated, custom, hardware. At very high luminosity, with 20-40 interactions superimposed, and with only some of the event information available the trigger performance will degrade. Upgrades to the muon system (and also to the hadron calorimeters) aim to preserve the Level-1 trigger capability by providing it with more and higher quality inputs.

For the initial phase of CMS, three types of gaseous detection technologies (see Fig. 1) have been chosen, according to the different background rates and magnetic field the detectors have to withstand. Where neutron background is relatively small and in the 1-10 Hz/cm² range, Drift Tube Chambers (DTs) are used. In the endcap regions where the background rate is higher and around 100-200 Hz/cm² and the magnetic field is more intense than in the barrel, cathode strip chambers (CSCs) are selected.

DTs and CSCs, both with self-trigger capabilities, can be used to measure the momentum and time of crossing of the muon. In addition, to assure an unambiguous bunch crossing (bx) identification and to build up a robust and redundant system, Resistive Plate Chambers (RPCs) both in the barrel and endcaps are used, providing a fast and accurate time measurement. The muon momentum resolution is extracted by combining information of the muon track from the muon system, modulated by the Global Muon Trigger with an efficiency > 96%, complemented with the more precise tracker measurement (including the vertex constraint). A momentum resolution down to 2 % is obtained for $p_T < 100$ GeV (at all pseudorapidities) and 18 % for the most forward 1 TeV muon measurable by the CMS Muon spectrometer.

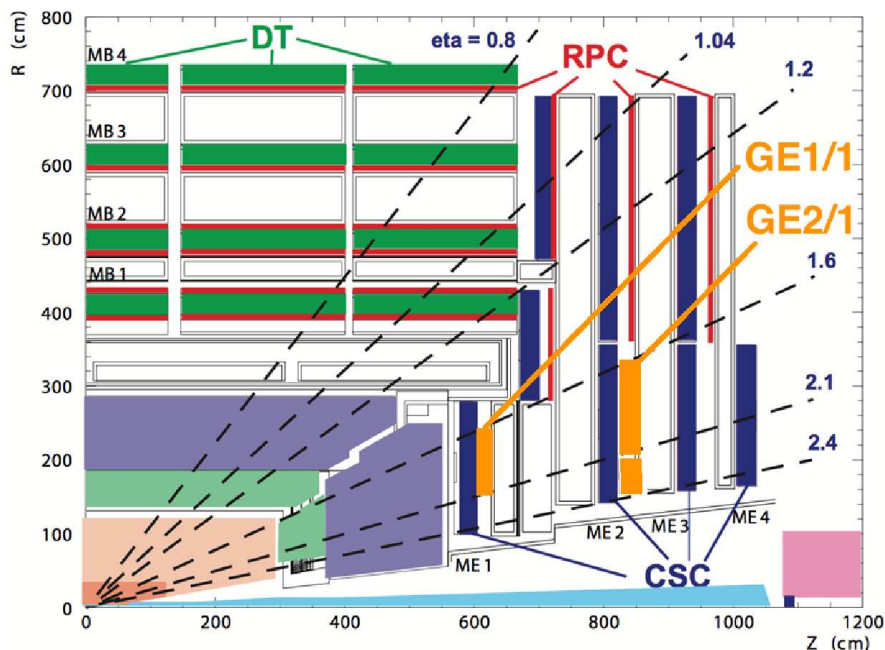


Figure 1: CMS transverse section showing the existing gaseous detector for muon tracking and triggering namely RPCs, DTs and CSCs and the locations of the proposed GEM detectors GE1/1 and GE2/1.

1.2 CSC (Cathode Strip Chambers)

CSCs are multiwire proportional chambers comprising anode wire planes interleaved with cathode strip panels where strips run radially according to CMS coordinates. By interpolating charges induced in the strips from the avalanche of positive ions near a wire, a precise localization accuracy $75\mu\text{m}$ - $150\mu\text{m}$, from low to high- η is

obtained. The angular resolution is $\approx 10\text{mrad}$.

The wire signals give fast and precise time information (5 ns) with coarser spatial resolution $16\mu\text{m}-54\mu\text{m}$. For high- η chambers, anode wires are rotated to compensate the Lorentz force under the 3.8 T magnetic field, avoiding electron charge to be spread along the wires. The nominal gas mixture is Ar/CO₂/CF₄ (45:15:40).

1.3 RPC (Resistive Plate Chambers)

The Resistive Plate Chambers[2] used in CMS are made of 2 gas gaps read out by a unique set of copper strips placed in between the two gaps. Each gas gap is made out of two Bakelite plates filled with a gas mixture of C₂H₂F₄/iC₄H₁₀/SF₆ (95.2:4.5:0.3) with a 50 % relative humidity to keep the Bakelite resistivity stable. Chambers are operated in avalanche mode, ensuring proper operation at rates of up to 100 Hz/cm².

RPCs guarantee a precise bunch crossing assignment thanks to their fast response and good time resolution. 3 rings of 4 stations each are present in the endcaps, as shown in Fig. 1. For the low luminosity phase the innermost ring (RE1/1) and the outermost stations (RE4) had been staged ($|\eta| > 1.6$), while RE4 stations have been up-scoped and are under construction for installation in the Long Shutdown LS1, during 2013-2014.

The high- η rings of all endcap stations have not yet been under consideration. For high momenta muons, it is imperative that the muon system functions well so that it contributes substantially towards momentum resolution. For forward muons, however, CMS redundancy is compromised, due to the missing high- η muon station and to the high background rate in the existing ME1/1 stations, already at the limit of the acceptable.

1.4 Muon system redundancy and extension up to $\eta = 2.4$

In Table 1 the particle rates and expected accumulated charges for different phases of LHC operation and its luminosity upgrades are shown. The RPCs radiation hardness is at the limit, and the large strip pitch (1-2 cm) may affect high-rate system performance, even with an adequate time resolution.

Micro-pattern gaseous detectors (MPGD[3],[4]) can reach rate capabilities up to 10MHz/cm² and provide high spatial (100 μm) and time ($\approx 5\text{ns}$) resolutions, with a $\approx 98\%$ detection efficiency. They can be operated with non-flammable component gas mixtures and finer readout granularity along both η and ϕ allows for both triggering and/or tracking.

1.5 Performance requirements for high- η muon detectors

For the forward Muon RPC low eta region, extensive tests were performed over several years in order to validate the RPC technology and the gas mixture for particle rates of $\approx 10\text{Hz}/\text{cm}^2$. Bakelite RPCs are well suited for operation at moderate rates ($< 1\text{kHz}/\text{cm}^2$). The international RPC community has devoted a tremendous effort on aging studies, and mainly due to the LHC RPC R&D work at GIF[5] (Gamma Irradiation Facility - CERN), we now have much better understanding for the mechanism of RPC operation, aging, rate capability. It has been clearly shown that RPC performance and degradation are determined by complex interactions among the operating conditions and the materials of the RPCs, in which the current, integrated charge, humidity, production of hydrofluoric acid, etc. affect the linseed oil, graphite coating, and the bakelite itself, in complex ways that result in degraded performance, increased dark current, reduced efficiency and increased resistivity[5]. A sophisticated gas system was commissioned in order to recuperate the expensive components of the gas and to filter the pollutants and contaminants produced during chamber operation. The tests carried out showed that the detectors are suitable for operation in the low- η region, while concerns remained about the possibility of achieving stable operation with the radiation conditions expected at $\eta > 1.6$. Thus the presently vacant high eta region of CMS RPC presents an opportunity to instrument it with a detector technology that could sustain the environment and be suitable for operation at the LHC and its future upgrades and the targeted installation period would be the long shutdown LS2, in the years 2017/18. At that point detectors installed should be able to withstand the hostile environment and high luminosity rates at the LHC upgrade, and sustain operation for a minimum of \approx ten years after installation namely until after CMS Phase II ($\approx 2020 - 2030$). The RE high- η region presents hostile conditions, with a particle fluence of several 100Hz/cm² for an LHC luminosity of $10^{34}\text{cm}^{-2}\text{s}^{-1}$, which may go up to several kHz/cm² depending on the upgrade scenarios. In addition the rates of thermal neutrons, low energy protons and γ must be taken into consideration. Hence the most stringent requirements for a detector at high η which can sustain operation in the upgraded LHC are summarized in the Table 1.

Table 1: Performance requirements in the various η sectors.

Region	Rates (Hz/cm ²) LHC (10 ³⁴ cm ⁻² /s)	High Luminosity LHC 2-3 \times LHC	Phase II (10 ³⁵ cm ⁻² /s)
Barrel RPC	30	Few 100	\approx kHz (tbc)
Endcap RPC 1, 2, 3,4 $\eta < 1.6$	30	Few 100	\approx kHz (tbc)
Expected Charge in 10 years	0.05 C/cm ²	0.15 C/cm ²	\approx C/cm ²
Endcap RPC 1, 2, 3,4 $\eta > 1.6$	500Hz \approx kHz	few kHz	few 10s kHz
Total Expected Charge in 10 years	0.05-1 C/cm ²	few C/cm ²	few 10s C/cm ²

Over the past two years, an effort has been focused on looking for options based on Micro-Pattern Gas Detectors (MPGDs). A dedicated R&D program was launched in 2009 to study the feasibility of using micro-pattern gas detectors for the instrumentation of the vacant $|\eta| > 1.6$ region in the present RPC endcap system. Micro-pattern gas detectors can offer an excellent spatial resolution of order 100 μm , a time resolution below 5 ns, a good overall detector efficiency above 98% and a rate capability of order 10⁶ Hz/mm² that is sufficient to handle the expected particle fluxes in the LHC environment. In the case of the existing RPC system, the large volume, the cost of the gas mixture, and the need to constantly remove impurities from the gas circuit to guarantee a stable detector operation, make the use of a rather complex closed-loop gas system including filtering mandatory. For MPGDs, their operation with a non-flammable gas mixture, e.g. Ar/CO₂/CF₄, is therefore also advantageous compared to the present RPC system.

With the enhanced (η, ϕ) readout granularity and rate capability of the MPGDs, one could effectively improve the Level-1 muon trigger efficiency and even offer both triggering and tracking functions at the same time. In this case, we consider to extend the pseudo-rapidity range of the system up to $|\eta| = 2.4$, to match the coverage of the Cathode Strip Chambers in the endcaps.

1.6 Present experience with MPGDs in experiments

An investigation of MPGDs as candidate technology to instrument the vacant zone in the high eta RPC part of the CMS detector, namely $1.6 < |\eta| < 2.4$, is undertaken. The objective is to develop the CMS detector with enhanced and optimized readout granularity $(\eta - \phi)$, and a rate capability improved by two orders of magnitude compared to RPCs, to improve the muon trigger efficiency and combine triggering and tracking functions.

Two types of micropattern detectors have been considered: the MICROMEGAs and the gas electron multiplier (GEM). The MICROMEGAs is a gaseous detector made with a metallic mesh exploiting the exponentially increasing Townsend Coefficient at very high electric fields. The gas electron multiplier on the other hand is a thin metal-coated polymer foil perforated with a high density of holes (50 – 100/mm²); each hole acting as the multiplication region. Single GEMs can operate up to gains of a several thousands and GEMs can be used in tandem. Thus a double or Triple-GEM detector delimiting the gas volume with a drift cathode and customized readout anode can be assembled. The operating point of each single GEM in a Triple-GEM is thereby at a lower gain with safe operating margin from the discharge point; multiple structures provide equal gain at lower voltage. Both technologies have the potential for production of large area detectors (1m \times 2m) with cost effective industrial processes. MICROMEGAs and Triple-GEMs have been installed at the COMPASS experiment in 2002 and were also operated for one week with a 25 ns LHC-like hadron beam with the intensity on the detector of $5 \cdot 10^6$ pions per spill of 5s on a surface of approximately 1cm², similar to the one expected in CMS for an LHC luminosity of 10³³cm⁻²s⁻¹. The COMPASS collaboration reports good performance of the GEM detectors, with no evidence of deterioration. Triple-GEMs have been installed in the first LHCb muon station, while ATLAS is considering the micromegas for its muon upgrade. On a COMPASS Triple-GEM operated at the gain of $2 \cdot 10^4$, a charge of 2C/cm² has been integrated on the readout board. GEM detectors are rather insensitive to ageing under sustained irradiation, at a gain of $\approx 10^4$ with Ar/CO₂ (70:30), corresponding to one year of continuous run at a maximum rate of 10⁵/cm². No sign of ageing has ever been observed which implies that the detectors could be operated without degradation at even higher integrated charges. Operation at lower gain (for example ≈ 8000) can further enhance the robustness of the detector for high particle rates, in view of the high luminosities that may be achieved with the LHC upgrades. For Triple-GEMs, with a gain of $\approx 2 \cdot 10^4$, very good gain stability was measured up to a photon flux of about $5 \cdot 10^7$ Hz/cm², and extensive ageing measurements have been performed in the past. Considerable improvement with respect to the Ar/CO₂ (70/30) gas mixture, which exhibits a poor time resolution of about 10ns rms, is obtained with the new CF₄ and iso – C₄H₁₀ based gas mixtures, which allow to reach time resolutions better than 5ns rms with the optimum choice which is the fast & non-flammable gas mixture Ar/CO₂/CF₄ (45:15:40). As all gaseous detectors, GEMs have a finite probability of exhibiting a breakdown

of the gas rigidity or discharge. Systematic investigations have been carried out; the most significant study is the measurement of the discharge probability of a Triple-GEM detector in a high intensity, low energy beam at PSI, the beam that best simulates the conditions expected at the LHC. It has been demonstrated that the detector does not deteriorate after multiple discharges with large repetition rates, provided that the amplifiers of the GEM electronics are properly protected¹⁾.

In the following feasibility study we have studied small and large size prototypes to demonstrate that the Triple-GEM detector fulfils all requirements for forward muon tracking and triggering at high eta CMS.

1.7 High- η muon detectors proposed for LS2 (2017-2018)

In Fig.2, the nose region of the first endcap disk is visible. In this document, we propose the installation of the stations called GE1/1 and GE2/1 as shown in Fig. 3. For the GE1/1 station the chambers will be installed on the YE1 'nose'. For the GE2/1 station, which sits exactly on the backside of YE1 'nose', there will be two sets of chambers; one long chamber and one shortened chamber due to the neutron shielding in the $2.1 < |\eta| < 2.4$ region. Since there is room for long chambers in z, the 2/1 station offers 4 measurements points from $1.6 < |\eta| < 2.1$ and two measurements points from $2.1 < |\eta| < 2.4$. The first station GE1/1 would have 10 degree chambers while for the second station GE2/1, 20 degree chambers are proposed. In the following section we describe the preliminary study of the impact of upgrading the CMS forward muon system with these detectors, on the performance of the muon system. In Section 3 the case for micropattern detectors is made based on the past and present experience. The intensive experimental and simulation studies with small prototypes are summarized. Full size prototypes were constructed and tested during 2010-2011 and the results from laboratory and beam tests are elaborated. The focus then shifts to the development of new technologies for fabrication and construction of full scale CMS detectors. Results from measurements in the laboratory and at the beam, with and without magnetic field upto 1.6 T are summarised.

From simulation studies we can conclude that the GEM detector stations would significantly improve the L1 muon trigger performance over that of the originally planned RPC-only system in the forward direction $|\eta| > 1.6$.

Large scale production scenarios are discussed with the assembly procedure and work flow description. Studies on integration and installation within the CMS high eta envelope are presented followed by the electronics system and other services including gas and cooling. A tentative schedule is presented for construction of the first two stations along with preliminary budget and resources needed. Finally the structure of the GEMs for CMS collaboration is described towards installation in LS2 (2017/2018).

¹⁾ Whenever the total charge in the avalanche exceeds a value between 10^7 and 10^8 electron-ion pairs (Raethers limit), an enhancement of the electric field in front of and behind the primary avalanche induces the fast growth of a long, filament-like streamer. This discharge is measured by counting the number of alpha particles that produce a current greater than $1\mu\text{A}$, the current from nominal radiation being of the order of few tens of nA.

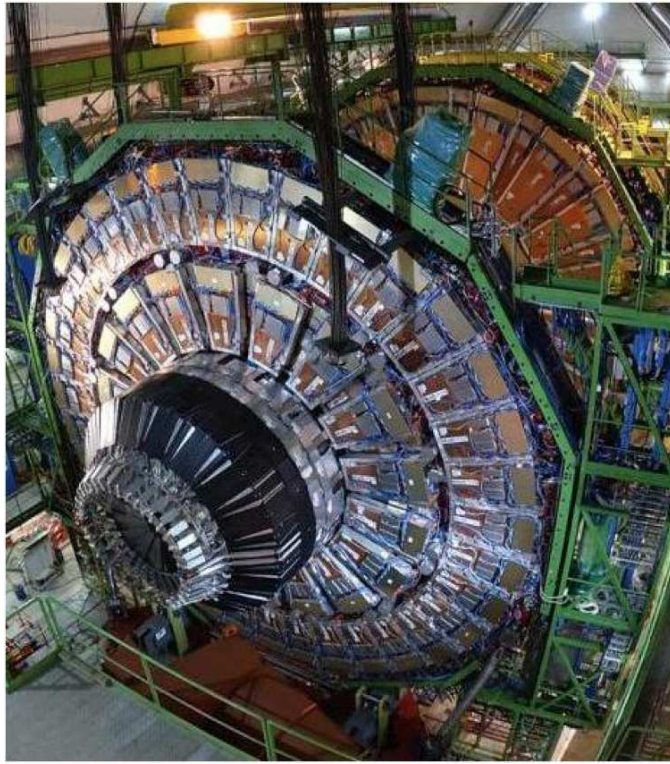


Figure 2: The CMS Endcap YE1 disk showing the “nose”, namely the high- η region.

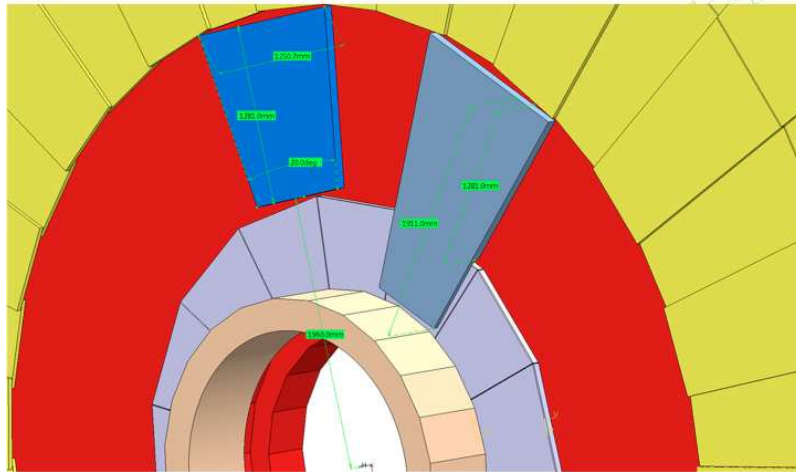
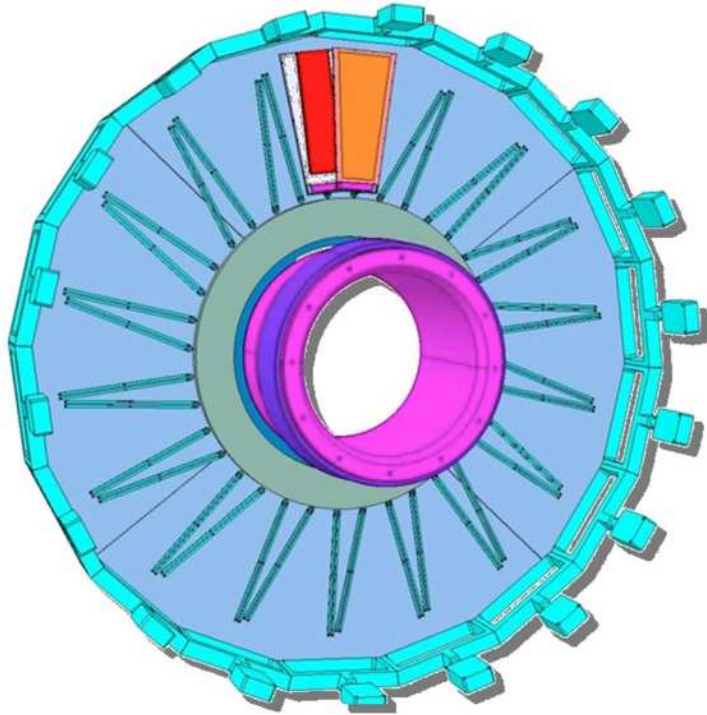


Figure 3: CATIA model of the CMS endcap structure for GE1/1 chambers (top) and GE2/1 Chambers (bottom). For the GE1/1 station the chambers will be installed on the YE1 “nose”. For the GE2/1 station, which sits exactly on the backside of YE1 “nose”, there will be two sets of chambers long and short due to the neutron shielding that sits between $2.1 < |\eta| < 2.4$. Since there is room for long chambers in z, the 2/1 station offers 4 measurements points from eta $1.6 < |\eta| < 2.1$ and two measurements points from $2.1 < |\eta| < 2.4$.

2 Impact of high- η upgrade on muon reconstruction

2.1 Muon system redundancy and extension up to $\eta = 2.4$

Muon detection is a powerful tool for recognizing signatures of interesting processes over the very high background rate expected at the LHC. This is particularly true as the luminosity increases.

By the start of Long Shutdown 2, CMS will have collected hundreds of fb^{-1} integrated luminosity at nominal center of mass energy. Whether CMS has discovered something or not, the program will continue with the determination of the fundamental properties of the discovered particles and with searches for rare processes and high mass new states, requiring even higher luminosity.

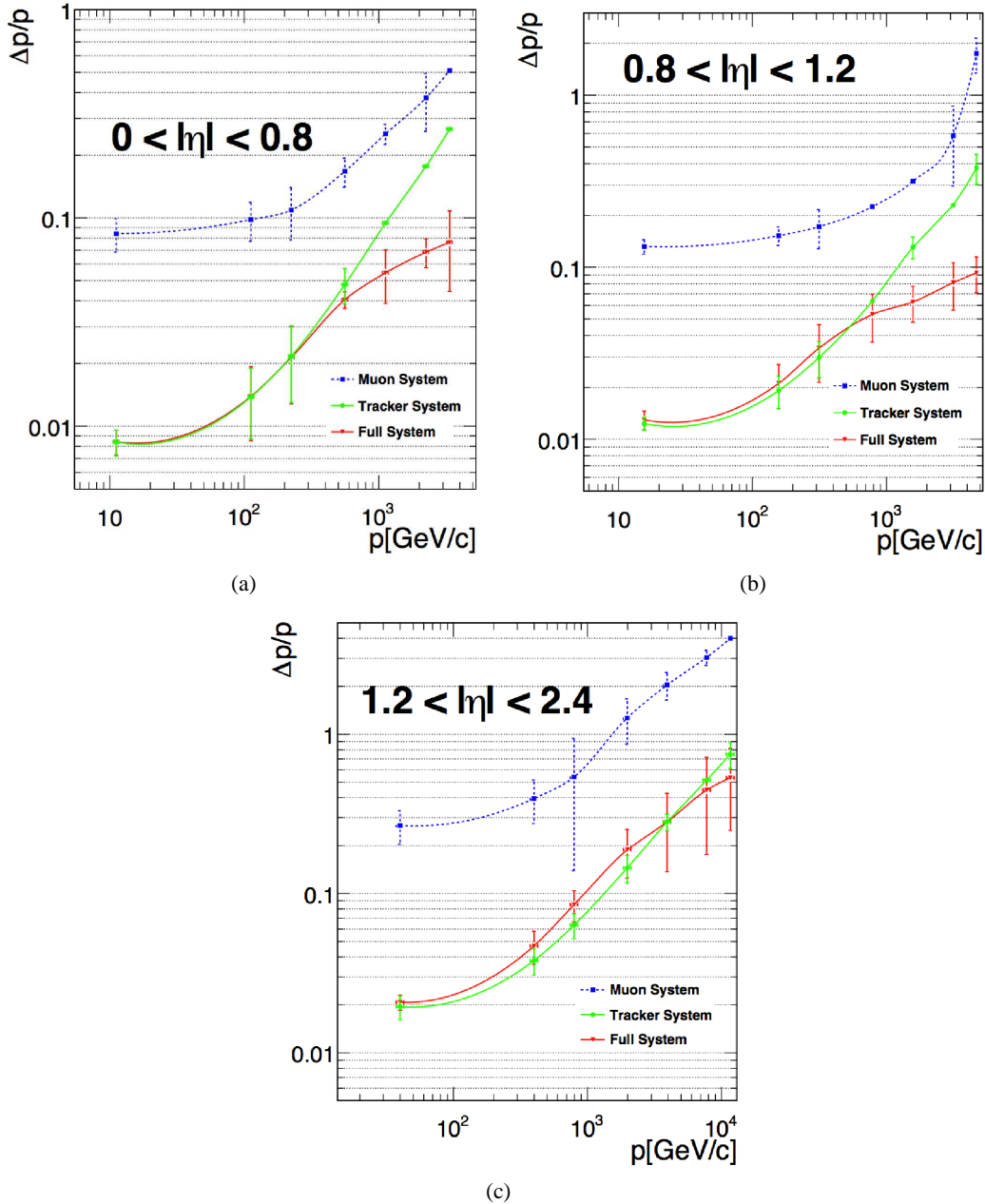


Figure 4: Muon momentum resolution as a function of momentum for barrel (a), overlap (b), and endcap (c) regions using the muon system only (blue), the inner tracking only (green) and both system together (red).

In this framework, the forward muon upgrade will provide additional hit measurements to obtain higher efficiency and higher resolution for muons in certain pseudo-rapidity regions, providing the necessary control on the trigger rates, in addition to significant additional acceptance for muons at the trigger level.

Therefore, the physics case for addition of forward muon chambers is straight forward. The foreseen upgrade for the CSC system will restore the reduced muon acceptance at trigger level in the region $1.2 < |\eta| < 1.6$. The installation of new RPC chambers in the same region (RE4) will provide the finer timing and redundancy for the corresponding CSC system. Upgrade in the $2.1 < |\eta| < 2.4$ will improve the trigger capability in the high luminosity regime, where the present ganging of some channels in these chambers results in an unacceptable number of spurious tracks.

The Muon System provides muon trigger and identification capability. The original CMS designed was tailored to setup a robust system through the redundancy. So far the experiment has achieved the design goals only up to $\eta = 1.6$.

In CMS the high momentum resolution of muons is given by the very precise point resolution of the Tracker system. The Muon system starts giving a sizable contribution in the high- η region, because of the reduced lever arm of muons in the Tracker volume. In Fig. 4 is shown the momentum resolution as a function of the muon momentum for the reconstruction in the inner Tracker system and the Tracker and Muon system[6]; muons with $p_T > 200$ GeV/c improve their resolution thanks to the addition of the Muon system information. For this reason, in this η region is particularly interesting to design a Muon system redundant also on the tracking capability. An additional detector system for the Muon system, with high point resolution, would also improve over the limited p_T resolution obtained in the Muon system only, shown in the same figure, for the benefit of the trigger L2 reconstruction in the High Level Trigger selection.

In order to study the impact of the upgrade Muon system on muon reconstruction performance, Monte Carlo single muon samples with different p_T have been generated. The CMS detector was simulated with GEANT4 within the existent CMS framework, where the proposed upgrade has been described by extending the existing geometry of the RPC system, up to $|\eta| < 2.1$. The muons transverse momenta, with respect to the beam axis, chosen for this simulation study are 0.2, 0.5, 1, 2, 5 TeV/c.

2.2 Multiple scattering

The spatial resolution lower limit, set by the electromagnetic processes that muons experience in traversing the CMS material, has been estimated from simulation and the results are depicted in Fig. 5. The left plot indicates the dominant role of the multiple scattering with respect to the effect of the magnetic field and other electromagnetic processes such as bremsstrahlung; the results refer to the first station but the conclusion is valid for all stations. The right plot shows the displacements as a function of the p_T in the different endcap station. In the first endcap station the rms of the displacement of 1 TeV muon is $100 \mu\text{m}$, while it reaches $500 \mu\text{m}$ for the fourth and last station.

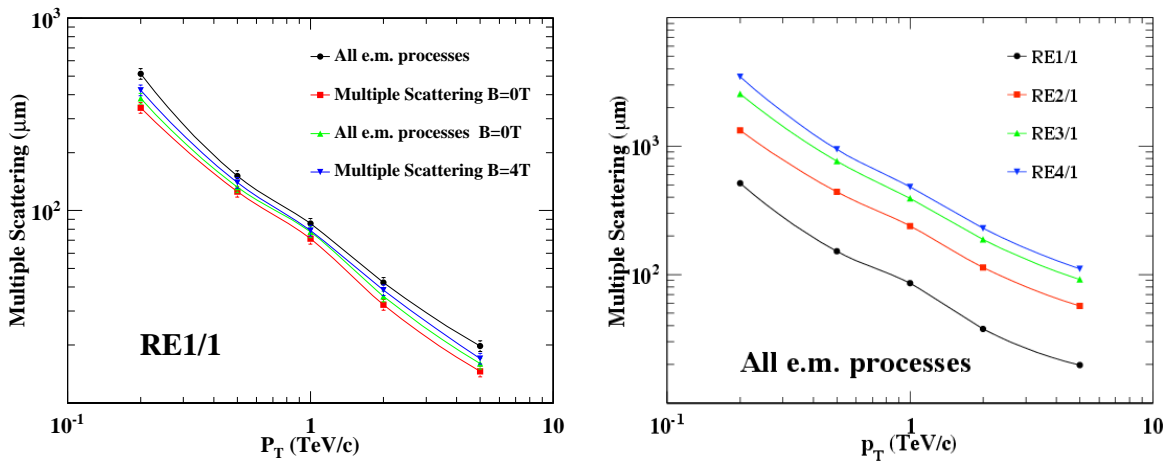


Figure 5: The rms of the distribution of the displacement as a function of the muon p_T of the muon due to electromagnetic processes. On the left the results obtained in the first station are shown for nominal magnetic field (no magnetic field) for all e.m. processes in full circles (upward triangles) and for multiple scattering only in downward triangles (full squares). The right plot describes the values for the different stations.

2.3 Muon track reconstruction

The strip pitch of the new proposed chambers has been set to different several widths, each corresponding to a given GEM spatial resolution. For the sake of simplicity, just resolutions corresponding to number of readout channels multiples of the standard 32 RPC strips reported in the original CMS TDR are used, from 1, corresponding to 1 cm and a nominal point resolution of 3-4 mm, to 128 corresponding to a nominal resolution of 25 μm .

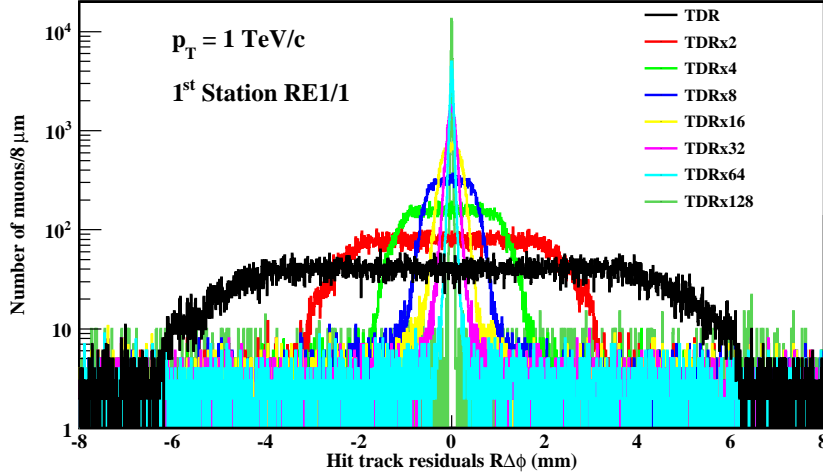


Figure 6: Muon hit residual distribution for increasing number of readout channel. The residuals are computed extrapolating the muon track to the detector surface placed in the first ring of the first endcap disk. The displacement is obtained as difference of the azimuthal angle times the radial distance of the extrapolated point.

In Fig. 6 single muons spatial residuals in Disk-1 Ring-1, from which point resolution is derived, for different strip widths are compared. The strips width dominates the resolution down to widths a factor 8 more narrow than the TDR ones. From a factor 16 upward ($\sigma = 200\mu\text{m}$) the distributions approach a Gaussian shape.

Muon track pattern recognition in CMS have been used to estimate transverse momentum resolution. Hits from the foreseen RPC system are added in the final fit of the muon track. The impact of the GEM detector is derived by substituting the first station or the two first station with higher resolution GEM. The resulting momentum resolutions are shown in Fig. 7. On the top are shown the relative resolution for the global muon algorithm. The right plot describes the resolution as derived from the r.m.s. of the transverse momentum distributions. Large values are due to the tails induced by phenomena like bremsstrahlung. The left plot is obtained from the variance of a Gaussian distribution fitted in the core of the distributions. On the bottom the same plots are shown for a dedicated algorithm tailored for TeV muons that alleviates the effects of the bremsstrahlung. Indeed the resolutions overall improve especially those computed from the r.m.s. as expected. This study shows that the muon system has still margins of improvement in the performance of the muon reconstruction. Further studies are necessary to have a clear estimation of the performances with a more realistic simulation of the GEM detectors and with the exact proposed Geometry.

The major result is that GEMs, being also a tracking devices, allows the muon pattern recognition also in partial, and even total absence, of the CSC allowing a direct measurement of the tracking performances using two independent muon systems. The results of a preliminary are shown in Fig. 8, where the momentum resolution distribution is shown on different Muon system configuration. The full curve represents the transverse momentum resolution for the Global Muon algorithm where, together with the Tracker, the existing CSC system and the foreseen RPC stations are used. The role of the RPC, on this aspect is rather marginal, indeed the similar resolution is obtained by using Tracker and CSC as shown by the dotted histogram. The Tracker and RPC only results are described by the dashed curve and is given by the Tracker resolution. Finally the point-dashed line represents the case where the first station is instrumented with a layer of Triple-GEM with a point resolution as extreme as 50 μm and the pattern recognition is performed using just the Tracker, the GEM layer and the three outer RPC stations.

The obtained results of the muon momentum resolution obtained with high resolution tracking device are very promising. In order to obtain a complete redundancy of the Muon system the GEM should be also capable to provide independent pattern recognition and seeding of the track momentum fit. This can be achieved by instrumenting the inner stations with a double layer of GEM.

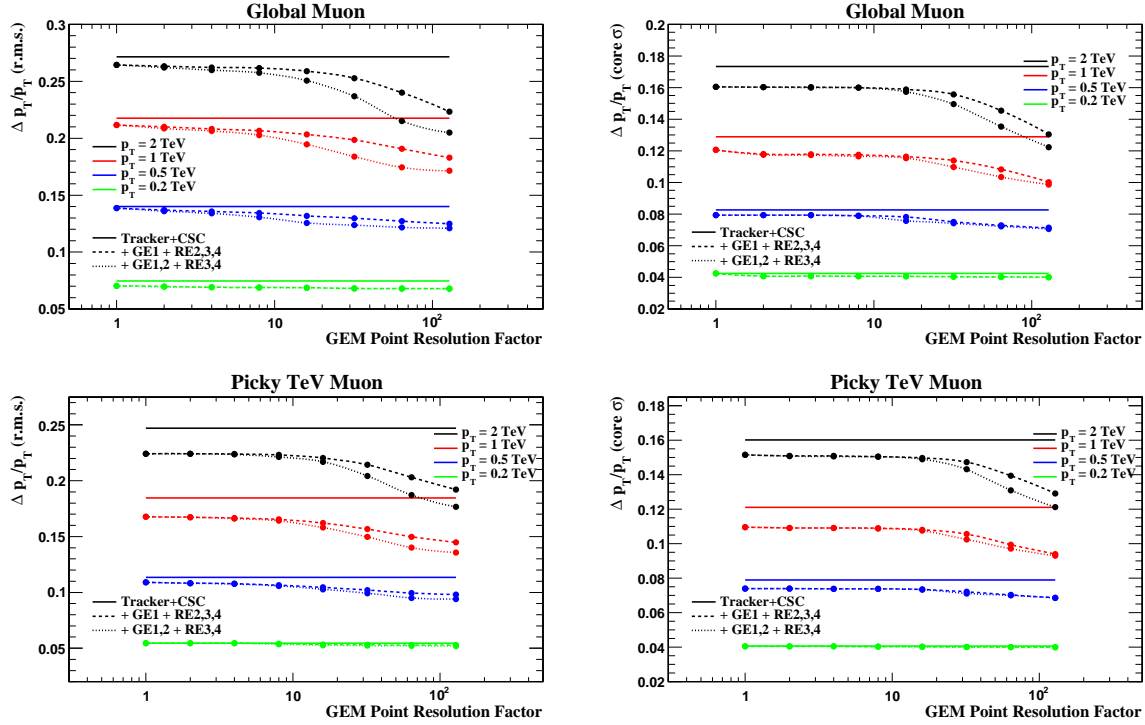


Figure 7: Momentum resolution of 0.2, 0.5, 1 and 2 TeV muons as a function of the GEM resolution factor. GEMs with resolution factor 1 behave like RPCs. For increasing factor the point resolution decreases inversely proportional. On the top muons are reconstructed with the Global Muon algorithm, while on the bottom they are reconstructed with a dedicated algorithm aimed to clean up muon detection layer affected by bremsstrahlung. The r.m.s. of the momentum distributions are used to derive the resolutions shown on the two right plots, while the results described in the two left plots are obtained by using the variance of Gaussians fitted in the core of the distributions. The straight continuous lines are the resolution of the Tracker and CSC Muon systems. The dashed lines are the results obtained by adding on the first station a layer of GEMs and RPC on the other three stations. The dotted lines are the performances measured when GEMs are used in the two inner stations and RPC are used in the two outer stations.

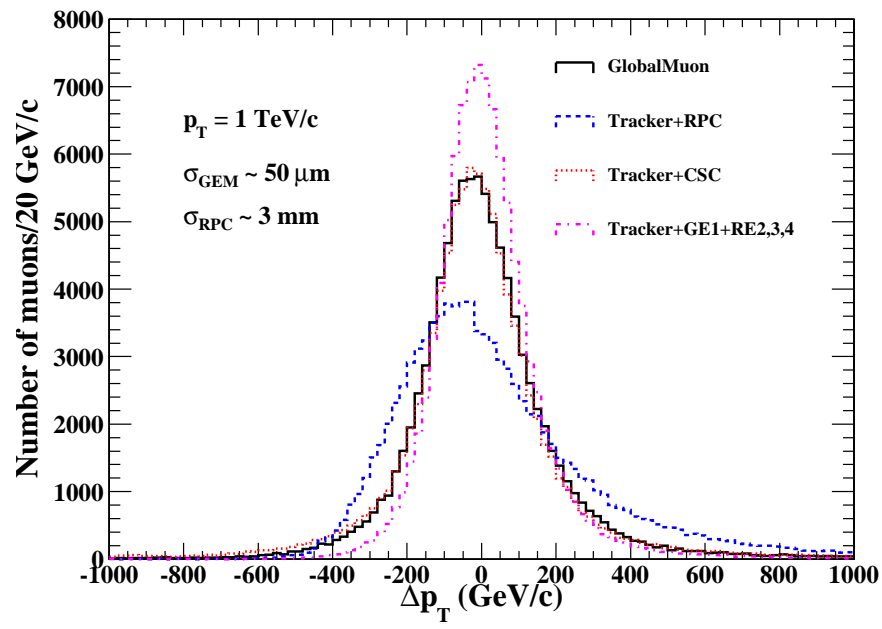


Figure 8: Muon transverse momentum resolution for different Muon system configuration. The full curve represents the standard global muon algorithm used with Tracker, CSC and RPC. The dashed curve is the result of the fit performed using Tracker and RPC. The resolution distribution for Tracker and CSC is given by the dashed curve. Finally the impact of the first GEM station with Tracker, CSC and the 3 outer RPC stations is visible in the point-dashed curve.

3 Studies of small and full-scale GEM prototypes

3.1 Initial prototypes for choosing among MPGD technologies

As the very first step of this project, small prototypes of two different MPGD types were characterized: one Micromegas [7] detector and one Triple-GEM [8] detector. Both prototypes were produced with an active area of $10\text{ cm} \times 10\text{ cm}$ in the CERN EN-ICE surface treatment workshop and were subsequently tested in the RD51 [4] lab of the CERN Detector Technology Group (DT). Using standard Ar/CO₂ gas mixtures, the two detectors were characterized by measuring gain and pulse height spectra with radioactive sources and Cu x-rays from a generator. Their efficiency plateaus were measured and the optimal operational voltages were determined.

In October 2009, the two prototypes were put into a pion/muon test beam at the CERN SPS H4 beam line [9]. In this test, good detector performance was observed for the Triple-GEM while the Micromegas prototype showed a substantial number of discharges and hence poorer data quality. The discharge probabilities of the two detectors were subsequently measured in the RD51 lab. For the Triple-GEM a probability of 10^{-6} was measured for gains up to $2 \cdot 10^4$, while the Micromegas was discharging with a probability of 10^{-4} at a gain of less than 2000. These results were consistent with previous MPGD studies. Based on these findings and given the existing expertise on GEMs within the research group, the Triple-GEM MPGD was selected for detailed further studies.

3.2 Triple-GEM prototypes

GEM foils are made from $50\text{ }\mu\text{m}$ thick kapton sheets with a $5\text{ }\mu\text{m}$ copper cladding on both sides. The initial small $10\text{ cm} \times 10\text{ cm}$ Triple-GEM was constructed using the standard double-mask technique for etching GEM foils. The GEM foils and cathode drift foils were glued onto fiberglass frames and mounted inside a gas-tight box as shown in Figure 9. The detector had 128 readout strips with a pitch of 0.8 mm. Two different gap size configurations were tested to study the effect on the detector performance, i.e. (drift, transfer 1, transfer 2, induction gap size): (3/2/2/2 mm) and (3/1/2/1 mm). For this Triple-GEM prototype a rate capability of over 10 kHz/mm^2 and a time resolution of 4.5 ns (rms) were measured (see Section 3.4.2).

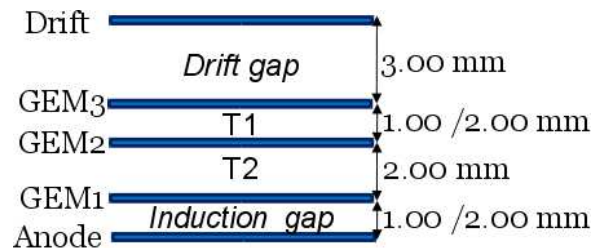


Figure 9: The standard double-mask Triple-GEM prototype. Left: Detector during assembly. Right: Configuration of gaps between electrodes.

The stretching of GEM foils during detector assembly is a somewhat time-consuming procedure. An alternative construction technique was investigated with a small Triple-GEM prototype where honeycomb spacers were inserted into the gaps between the electrodes to main the distances between electrodes and to avoid the need for foil stretching. A significant detection inefficiency was observed where the honeycomb “ribs” are located [10] and consequently this technique has not been pursued further.

In addition to the standard double-mask GEM prototype, a $10\text{ cm} \times 10\text{ cm}$ Triple-GEM prototype was constructed in the same way but using GEM foils produced with the single-mask etching technique [11], which overcomes the problems with the alignment of the masks on either side of the foils during the photolithographic etching of the holes. This prototype had 256 strips in each of two perpendicular directions with a strip pitch of 0.4 mm.

3.3 Single-mask GEM production technology

The production of GEM foils is based on photolithographic techniques commonly used by the printed circuit industry. The copper-clad kapton substrate gets laminated on both sides with solid photoresist of 15 μm thickness that the GEM hole pattern is transferred onto by UV exposure through flexible masks. In order to get good homogeneity of the hole geometry across the foil, it is very important to keep the alignment error between the masks on the two GEM foil sides within 10 μm . However, since both the raw material and the two masks are made from flexible material, the manual alignment procedure becomes extremely cumbersome when the linear dimensions of the GEM exceed 40 cm.

A natural way of overcoming this problem is the use of single-mask photolithography. In this case the GEM pattern is transferred only to one side of the raw material, thus removing any need for alignment. The exposed photoresist is developed and the hole pattern is used as a mask to chemically etch holes in the top copper electrode of the GEM foil. After stripping the photoresist, the holes in the top copper electrode are in turn used as a mask to etch the polyimide.

Single-mask photolithography (Fig.10) has been proven to be a valid manufacturing technique for making GEMs. This technology was used to build a prototype detector for a possible upgrade of the TOTEM T1 detector. More recently, the production process has been refined even more, giving great control over the dimensions of the GEM holes and the size of the hole rims during the production process. Effects of the hole shape are also being explored in simulation studies (see below). Production issues have been studied and single-mask GEMs are compatible with industrial production using roll-to-roll equipment, which is a very important aspect of this new technique. Consequently, a price reduction for GEM foils is expected from large-scale industrial production that is now possible.

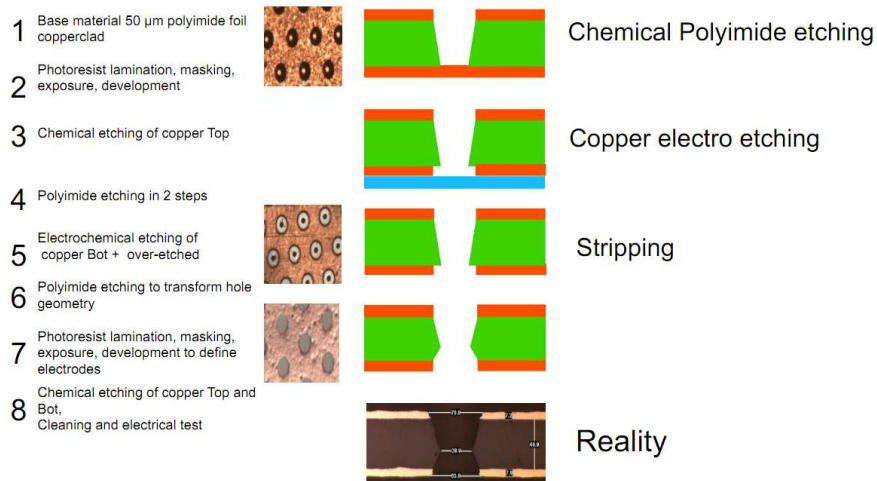


Figure 10: Overview of single-mask etching process for GEM foils.

3.4 Test beam measurements

The Triple-GEM prototypes were tested with a 150 GeV muon/pion beam at the CERN SPS H4 beam line during several RD51 test beam campaigns. The detectors under test were mounted into the RD51 Triple-GEM beam telescope as depicted in Figure 11. The telescope itself consists of three standard Triple-GEM detectors, referred to as tracker GEMs, each with 10 cm \times 10 cm active area and running with an Ar/CO₂ (70:30) gas mixture. They have 256 strips in both horizontal (y-coordinate) and vertical (x-coordinate) directions transverse to the beam, with a pitch of 0.4 mm. The telescope detectors were always operated at a gain larger than 10⁴. This setup served as the reference tracking device for the detectors to be tested.

The standard double-mask Triple-GEM prototypes under test were studied with different gas mixtures, Ar/CO₂ (70:30, 90:10) and Ar/CO₂/CF₄ (45:15:40, 60:20:20) at a gas flow of about 5 l/hour corresponding to roughly 50 detector volume exchanges per hour. The single-mask Triple-GEM was operated with an Ar/CO₂ mixture only.

The readout of all detectors including the tracker GEMs was done with electronics boards based on VFAT2 (Very Forward Atlas and Totem) chips [12] developed for TOTEM [13] by INFN Siena-Pisa. The VFAT2 ASIC was designed at CERN using radiation tolerant technology. It has a 128-channel analog front-end and produces binary

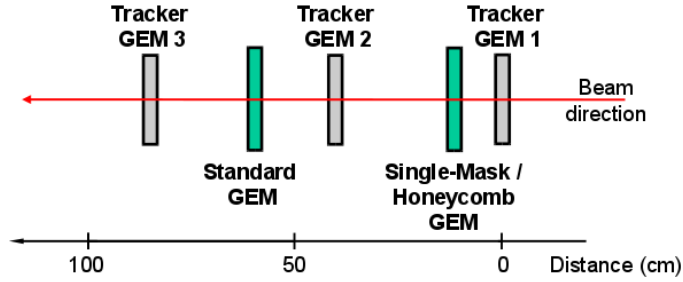


Figure 11: Positions of small Triple-GEM prototypes (green) within the RD51 beam telescope during tests at the CERN SPS H4 beam line. The Triple-GEMs of the telescope are labeled “Tracker GEM”.

output for each of the channels. In addition, it can provide a fast, programmable OR function on the input channels for triggering. The chip offers adjustable thresholds, gain, and signal polarity, plus a programmable integration time of the analog input signals. The signal sampling of the VFAT2 chip is driven by a 40 MHz internal clock.

During the test beam campaign, the readout of all GEM detectors with the VFAT2 electronics was binary. The tracker GEMs were read out in two dimensions with two VFAT2s connected to the 256 vertical strips, but with only one VFAT2 connected to 128 out of the 256 horizontal strips. The standard double-mask prototype had a one-dimensional readout with one VFAT2 connected to the 128 vertical strips, while the single-mask Triple-GEM had two-dimensional readout with two VFAT2s connected to the 256 vertical strips and one VFAT2 connected to 128 out of the 256 horizontal strips. Data were acquired from the VFAT2 chips with TURBO front-end electronics.

3.4.1 Data analysis and results

The results presented below for the different small Triple-GEM prototypes were obtained with data taken during the 2010 and 2011 RD51 test beam campaigns at the SPS.

Typical beam profiles for the muon and pion beam as reconstructed with the tracker GEMs of the RD51 beam telescope are shown in Figure 12. For the track reconstruction, events were selected in which the telescope GEMs had only a single cluster of fired strips. Straight tracks were fitted to these tracker GEM clusters and extrapolated to the detectors under study. The alignment of the detectors was done relative to the first tracker GEM, using the position of the clusters in each detector.

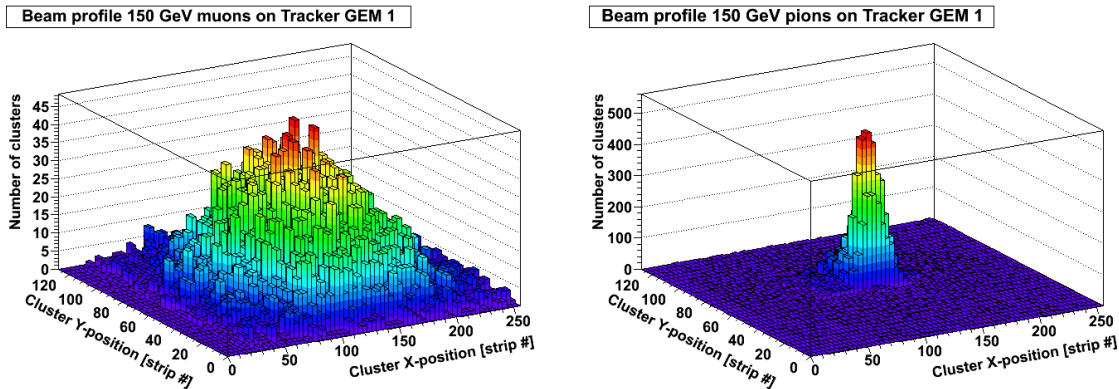


Figure 12: Beam profiles for muons and pions obtained with the tracker GEMs in the beam telescope.

3.4.2 Standard double-mask Triple-GEM

The typical value measured for the position resolution for the standard double-mask Triple-GEM is about $270 \mu\text{m}$ as demonstrated in Figure 13. This value includes the uncertainty on the position of the extrapolated track at the detector, and agrees with the value of $231 \mu\text{m} (= 0.8/\sqrt{12} \text{ mm})$ expected from the strip pitch with a binary readout. Neither detector gap size configuration, used gas mixture, or operating gain were found to have a strong influence on this measured resolution as it is mainly driven by the strip pitch.

The measured efficiency for the standard Triple-GEM is displayed in Figure 14. The efficiency was determined for different gas mixtures and gap size configurations as a function of the detector gain. Although for the standard

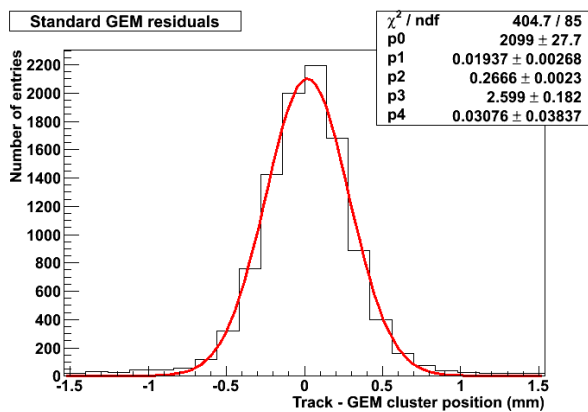


Figure 13: Residual distribution for the standard Triple-GEM, fitted with a Gaussian of the form $p_0 \cdot \exp(-0.5 \cdot ((x - p_1)/p_2)^2)$, plus a first-order polynomial of the form $p_3 + p_4 \cdot x$ to account for noise hits.

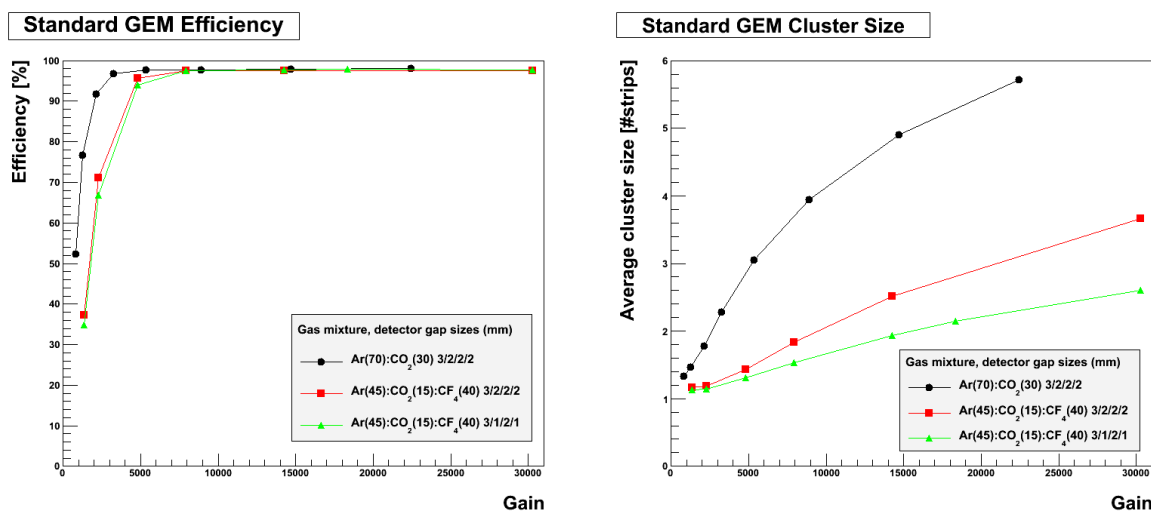


Figure 14: Detector efficiency (left) and strip cluster size (right) for the standard Triple-GEM with different gas mixtures and gap size configurations.

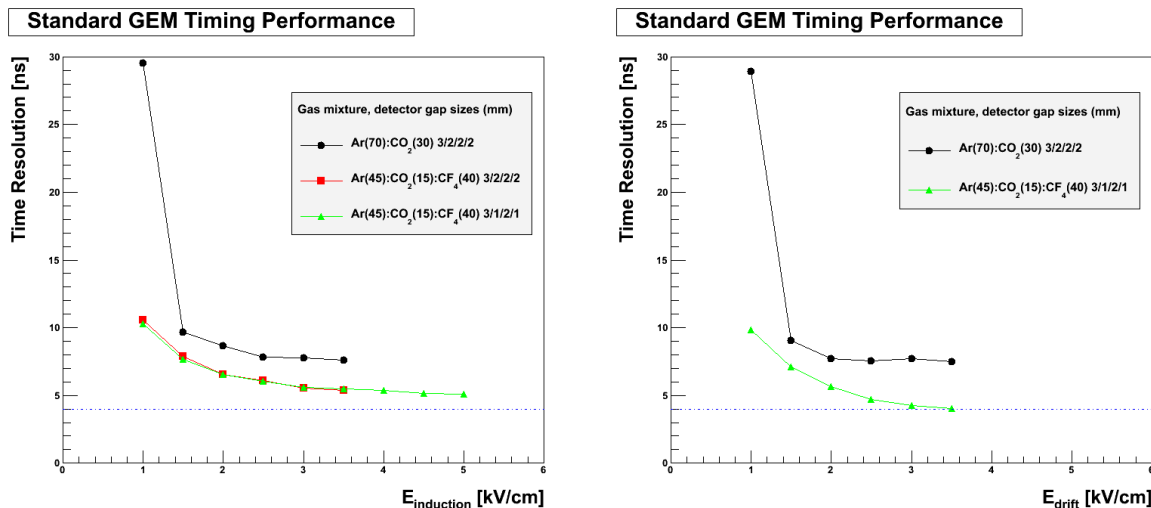


Figure 15: Detector timing resolution as function of the induction field (left) and drift field (right) for the standard Triple-GEM with different gas mixtures and gap size configurations.

Ar/CO₂ (70:30) gas mixture a slightly better performance is observed for low gain values, in each of the cases the efficiency reached the same plateau at about 98 % for a gain above 8000. Note also the stability of the detector

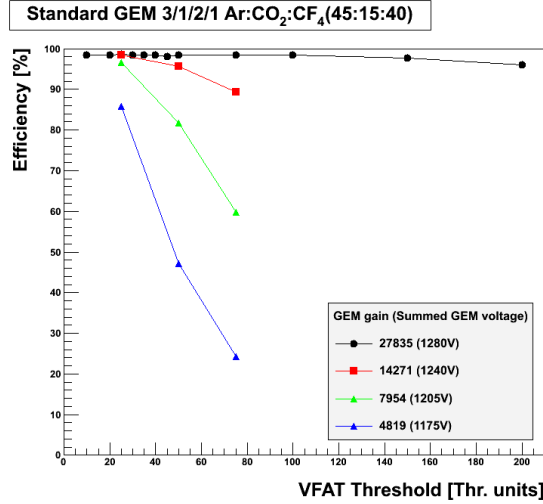


Figure 16: VFAT2 threshold scan for the standard Triple-GEM with the 3/1/2/1 mm gap size configuration and Ar/CO₂/CF₄ (45:15:40) gas mixture.

performance up to high gains of about $3 \cdot 10^4$.

The effect of the different gas mixtures and the gap size configurations for the standard Triple-GEM on the measured average cluster size, expressed in number of detector strips, is shown in Figure 14. Clearly, the use of the Ar/CO₂/CF₄ (45:15:40) gas mixture gives a much better performance for a digitally read out detector than the standard Ar/CO₂ (70:30) mixture because there are fewer strips per cluster. Also, the configuration with the smaller transfer gap 1 and induction gap size gives slightly better results.

The timing performance of the standard Triple-GEM was studied using a custom-made high voltage divider that allowed individual modification of the electric fields in the different detector gaps. For this study, plastic scintillators positioned in front and behind the beam telescope were used to generate a trigger to signal the passage of a beam particle through the detector. The spread in arrival time of the GEM signal from the VFAT2 board with respect to this external trigger was measured with a TDC module. In these measurements one has to take into account the 40 MHz clock cycle of the VFAT2 chip, which introduced a 25 ns jitter in the arrival time of the detector signals. Note that in case of the LHC, this jitter can be avoided with a proper synchronization of the VFAT2 cycle with the LHC clock. The obtained time resolution after a deconvolution of the 25 ns VFAT2 jitter is displayed in Figure 15. The electric field across either the induction gap or the drift gap was varied while keeping the other fields constant at (drift, transfer 1, transfer 2, induction gap) 2/3/3/3 kV/cm. The different gap size configurations had no visible effect on the timing performance. However, the timing performance is clearly better with the Ar/CO₂/CF₄ (45:15:40) gas mixture. With this mixture, a timing resolution of 4 ns could be obtained.

Based on the observed noise in the detector without beam, a minimum VFAT2 threshold of 25 units was used for all measurements. To check the effect of the VFAT2 threshold on the apparent detector performance, a VFAT2 threshold scan was performed for the standard Triple-GEM operating at different gain values as displayed in Figure 16. With the VFAT2 threshold set at 25 units, no impact of the threshold on the efficiency was observed when the detector was operated at a gain larger than 10^4 .

3.4.3 Single-mask Triple-GEM

Several of the measurements as described above were also performed on the single-mask Triple-GEM to compare its performance to the standard double-mask Triple-GEM. Figure 17 shows the measured efficiency and average strip cluster size for the single-mask Triple-GEM. The single-mask GEM reaches a comparable performance level as the corresponding double-mask GEM (see Figures 14-16) albeit the efficiency plateau is attained only at a gain level well above 10^4 .

3.4.4 Performance summary for small prototypes

For the standard double-mask Triple-GEM, the best detector performance was observed using Ar/CO₂/CF₄ (45:15:40) gas mixture instead of Ar/CO₂ (70:30) and with a 3/1/2/1 mm gap size configuration. Detector efficiencies up to $\sim 98\%$ and time resolutions down to 4 ns were obtained. The detectors could be operated stably up

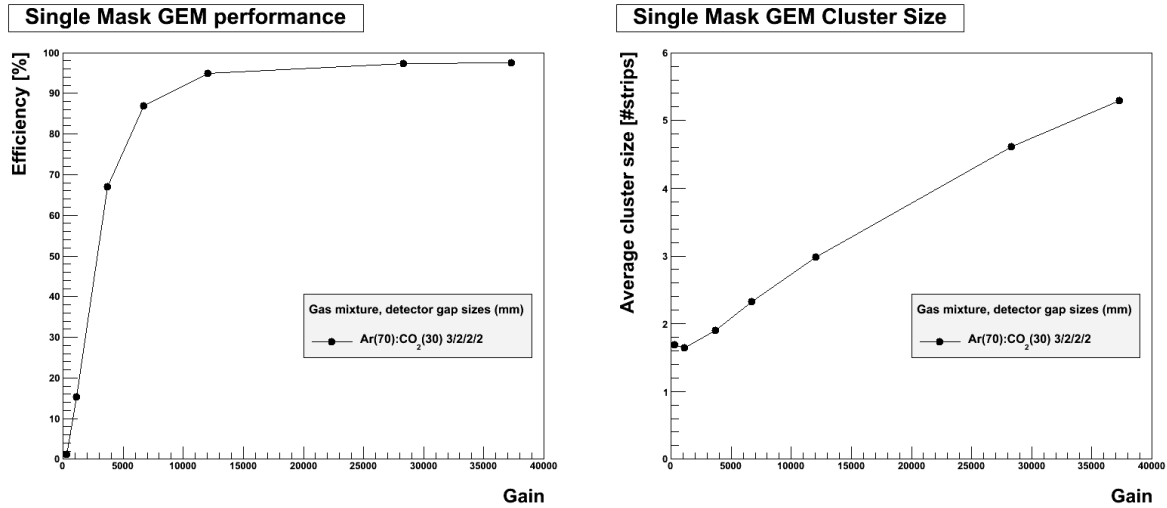


Figure 17: Detector efficiency (left) and strip cluster size (right) for the single-mask Triple-GEM.

to gains on the order of $3 \cdot 10^4$. The Triple-GEM produced with the single-mask technique performed similarly to the standard double-mask Triple-GEM.

3.5 Full-size Triple-GEM prototype

3.5.1 Prototype description

In addition to the small prototypes described in Section 3.2, two full-size prototypes of Triple-GEM chambers for a CMS GE1/1 station were produced and studied. These prototypes have a trapezoidal shape with an active area of $990 \text{ mm} \times (220 - 455) \text{ mm}$ as shown in Fig. 18 and are labeled “GE1/1-I” (April 2010) and “GE1/1-II” (March 2011).

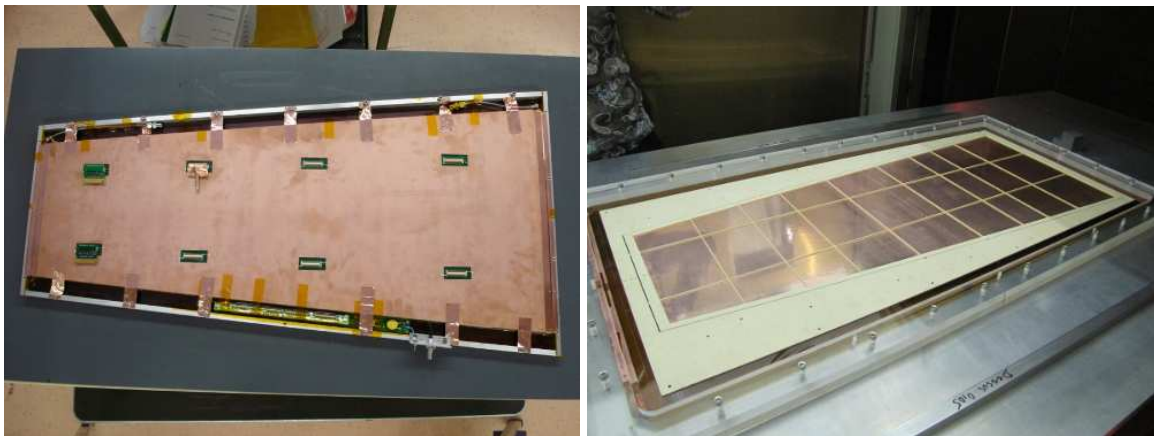
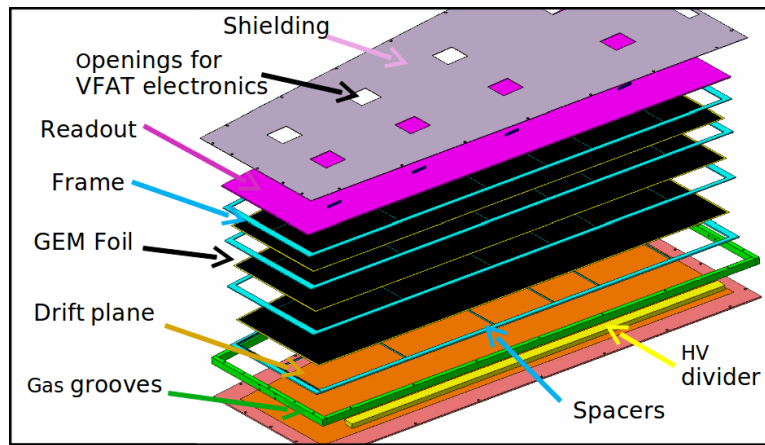


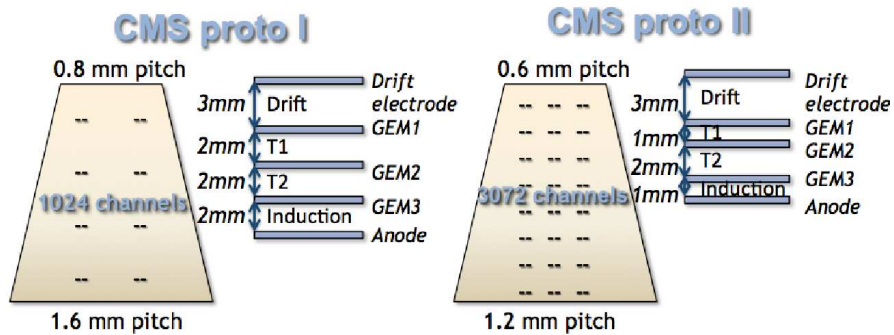
Figure 18: The first prototype of a full-size Triple-GEM detector for CMS. Left: Completed detector. Right: Glueing of spacer frames during detector assembly.

Their geometry followed the design for the RPCs that were to be installed originally in the ME1 endcap disks in the highest η region, i.e. RE1/1. In fact, the GEM detectors were embedded in an aluminum cover box similar to what was designed for the RPCs in that region. These chambers each would cover a 10° azimuthal sector of the muon endcap disks. Fig. 19(a) shows an exploded view of GE1/1-I, while Fig. 19(b) displays the general layout and different gap size configurations of the two prototypes.

The GEM foils for both large-area prototypes were produced at CERN using the single-mask photolithographic process described above. To limit the discharge probability and strength, the foils are divided into 35 sectors of about 100 cm^2 each. The drift electrodes, made of a thicker $300 \mu\text{m}$ kapton foil with a solid $5 \mu\text{m}$ thick copper cladding, were glued directly onto the 3 mm thick bottom aluminum baseplate of the detector cover box. The



(a)



(b)

Figure 19: (a) Exploded view of the first full-size Triple-GEM prototypes for CMS. (b) Electrode layout and gap size configurations of the two full-size prototypes GE1/1-I (left) and GE1/1-II (right).

readout planes provide a one-dimensional readout using radial strips running in long direction of the chamber, with a pitch varying from 0.8 mm (short side) to 1.6 mm (long side) for GE1/1-I and from 0.6 mm to 1.2 mm for GE1/1-II. If the chambers were installed in CMS, the radial strips would point to the LHC beam line. The first prototype was divided into four η -partitions with 256 strips per partition, while the second prototype had eight partitions with 384 strips each. Due to the improvements in GEM timing performance obtained with the small prototypes, the gap size configuration for the second large prototype was changed to 3/1/2/1 mm (drift, transf.1, transf.2, induction) from the 3/2/2/2 mm configuration for the first prototype. Different steps of the assembly procedure of the large prototypes are depicted in Fig. 20. Fig. 21 shows the gain curve for GE1/1-I measured with an x-ray gun in the RD51 lab.

3.5.2 Test beam setups

The full-scale prototypes were tested with 150 GeV muon/pion beams at the CERN SPS H4, H6, and H8 beam lines during several RD51 test beam campaigns in 2010 and 2011. The RD51 standard double-mask Triple-GEM beam telescope (Fig. 23) as described in Section 3.4 was used as a reference tracking device also in these tests. The GE1/1-II was installed near the RD51 telescope on a vertically movable table for scanning different points to account for the varying pitch of the full-scale detector along its long axis.

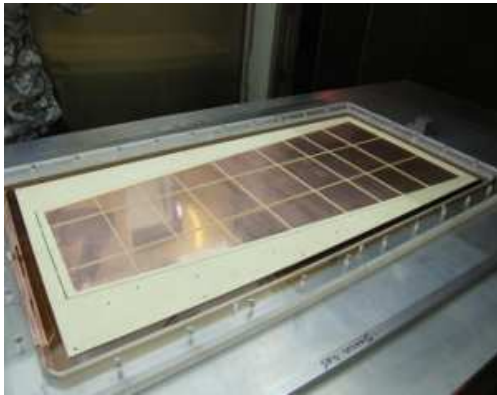
Fig. 24 shows a typical profile of the muon beam as reconstructed with the GEM telescope. After alignment, the reconstruction algorithm fits telescope hits in both dimensions providing a track space resolution of around $50 \mu\text{m}$.



(a)



(b)



(c)



(d)

Figure 20: Assembly procedure of the full-size CMS prototypes: (a) foil stretching in the oven; (b) gluing the spacer frames; (c) curing the glue; (d) mounting the readout plane.

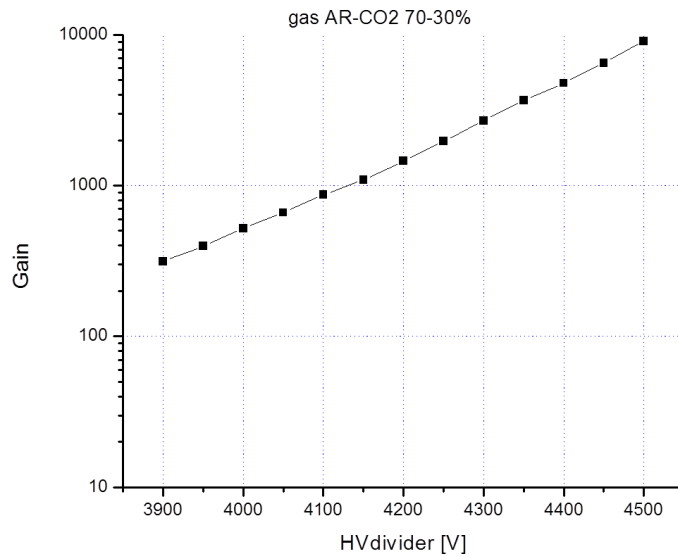
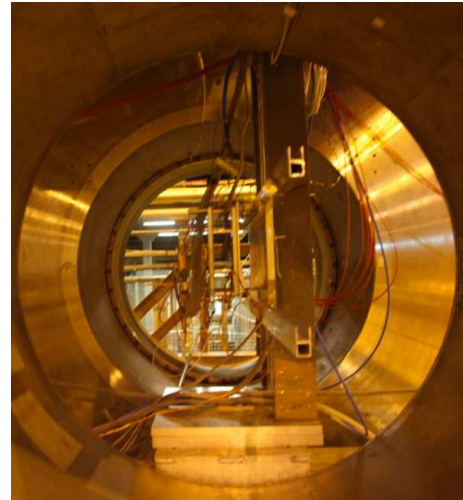


Figure 21: Gain curve for the GE1/1-I measured with x-rays in the RD51 lab.

In one beam test, the CMS M1 superconductive magnet was operated to test the GE1/1-II in a strong magnetic field. The M1 magnet is a solenoid that can achieve a field of 3T with a current around 4000 A. Inside the CMS detector, the GEM detectors would be installed in a location where the magnetic field can reach up to 1.5 T with an angle between the magnetic field and the electric field inside the GEM detector less than 8° . In this test, the RD51 Triple-GEM telescope as well as the PMTs for the trigger scintillators had to be kept 5 m away from the magnet so that they were not adversely affected by the magnetic field.



(a)



(b)

Figure 22: (a) The GE1/1-I detector installed in the SPS H4 beam line. (b) The GE1/1-II detector installed inside the CMS M1 magnet at the SPS H2 beam line.

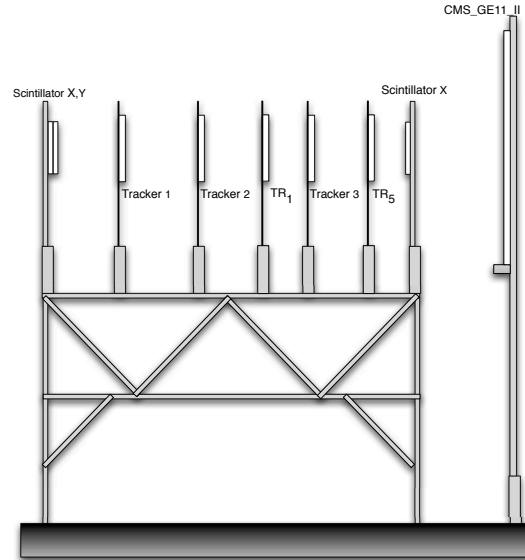


Figure 23: The RD51 telescope used during all test beams at the RD51 H4, H6, and H8 beam area.

3.5.3 Prototype performances in beam test

Fig. 25 shows a few results obtained with the GE1/1-I prototype in the October 2010 campaign.

With the beam pointing at the η -sector of the GE1/1-I detector with the smallest average strip pitch, i.e. 1.05 mm, a spatial resolution of $355 \mu\text{m}$ was measured with an Ar/CO₂ (70:30) gas mixture. This is close to the expected value of $1050 \mu\text{m}/\sqrt{12} = 305 \mu\text{m}$ for a binary readout. The detector efficiency was measured to be above 98% for this prototype. The uniformity of the detector response across the GEM active area was found to be very good.

In the 2011 measurements, the noise could be substantially reduced compared with the 2010 measurements when operating the detector with VFAT2 binary electronics. Based on the very low observed noise in the detector without beam, the VFAT2 threshold was set to 12 units²⁾ and the VFAT2 internal comparator current was set to $40 \mu\text{A}$. With these settings the noise was practically absent, when operating the detector with gains up to 10^4 .

Fig.26 shows average strip cluster sizes of 1.6-1.9 strips (depending on the η position) and a residual of $291 \mu\text{m}$ between extrapolated tracker tracks and hits measured in the GE1/1-II. This is about 20% better than what was

²⁾ One VFAT2 threshold unit corresponds to a charge of $\approx 0.08 \text{ fC}$ at the input channel comparator stage.

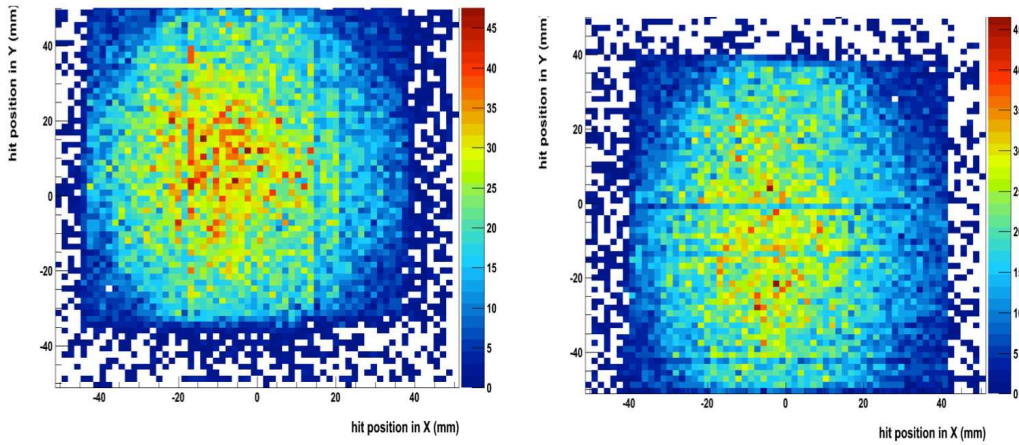


Figure 24: Typical muon beam profile obtained with tracker GEM detectors.

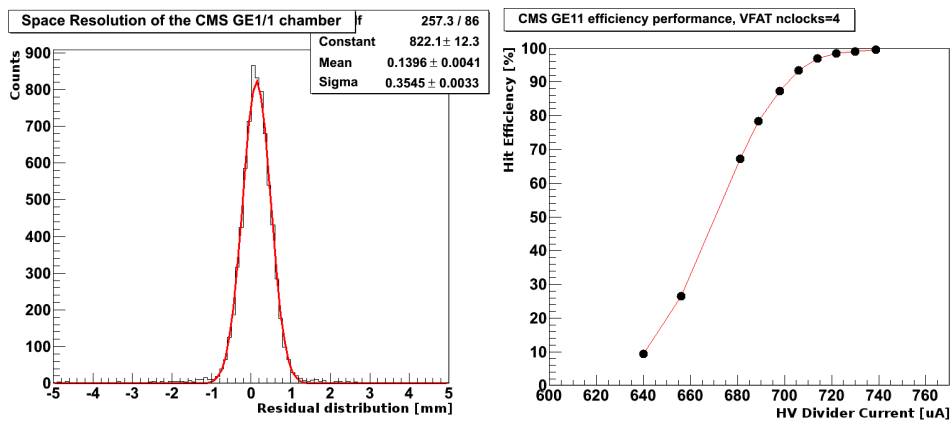


Figure 25: Results obtained with GE1/1-I during the Oct. 2010 test beam campaign: (a) residual distribution; (b) detector hit efficiency as function of the current in the HV divider, which is proportional to the electric fields in the GEM.

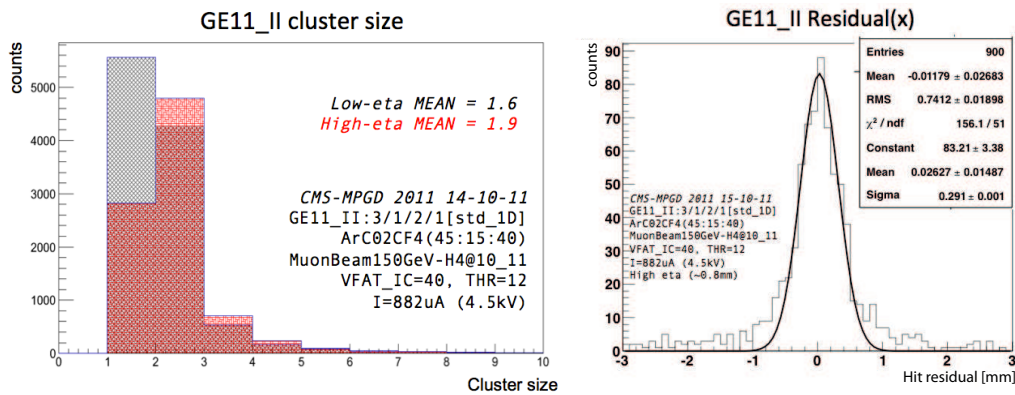


Figure 26: GE1/1-II performance: cluster size (left) and space resolution (right) at high and low η measured with VFAT2 binary electronics.

found with the GE1/1-I prototype. This is not unexpected as GE1/1-II has a 25% smaller strip pitch than the GE1/1-I.

A remarkable result is the fact that the GE1/1-II prototype reaches full efficiency with a gain of ≈ 7000 with Ar/CO₂/CF₄ (45:15:40) as shown in Fig. 27. This is in agreement with previous results on small prototypes and indicates that the full-size detector is performing excellently; operation at even higher gain is certainly possible, which would add a safety margin in terms of efficiency.

Fig. 28 shows results for the GE1/1-II prototype that were obtained during the August 2011 test beam campaign

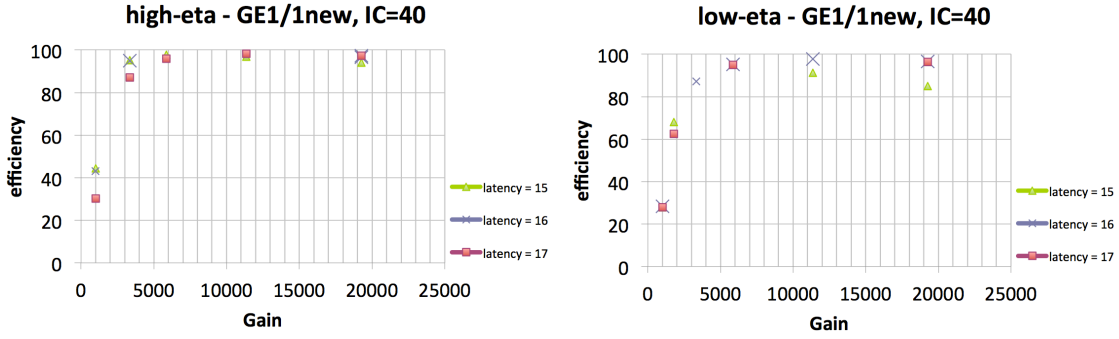


Figure 27: GE1/1-II efficiency performance at high and low η ends. Efficiency reaches 96.5% at gain 7000.

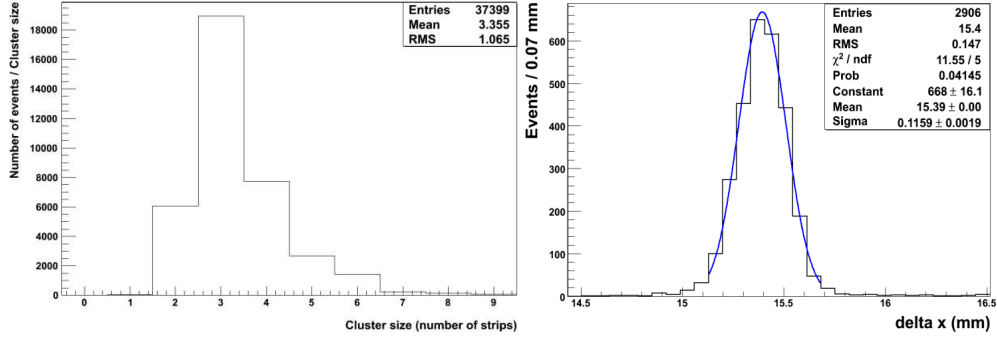


Figure 28: Results for GE1/1-II using pulse height measurements with APV25/SRS during the Aug. 2011 test beam campaign: (a) strip cluster size distribution; (b) difference Δx between hit positions measured with GE1/1-II and with a reference GEM in the tracker.

when the prototype was read out with electronics that recorded pulse height information. Specifically, the detector was read out with APV25[14] chips in combination with the Scalable Readout System (SRS) [15] that has been developed by the RD51 Collaboration. Two small 10cm \times 10cm GEM detectors TR_5 and TR_1 (see Fig. 23) were used to provide a reference measurement for the tracks. With the GE1/1-II prototype detector flowing an Ar/CO₂/CF₄ (45:15:40) gas mixture, data were taken with the H4 pion beam pointing at the detector region with the smallest strip pitch, i.e. 573 μ m.

An average cluster size of about 3 strips was found in this measurement and for the space resolution an upper limit of 103 μ m can be derived as shown below using the additional information on the charge sharing among adjacent strips that is available with a pulse height measurement. This result is significantly better than the resolution expected from a purely binary readout, i.e. strip pitch/ $\sqrt{12}$ = 573/ $\sqrt{12}$ = 165 μ m.

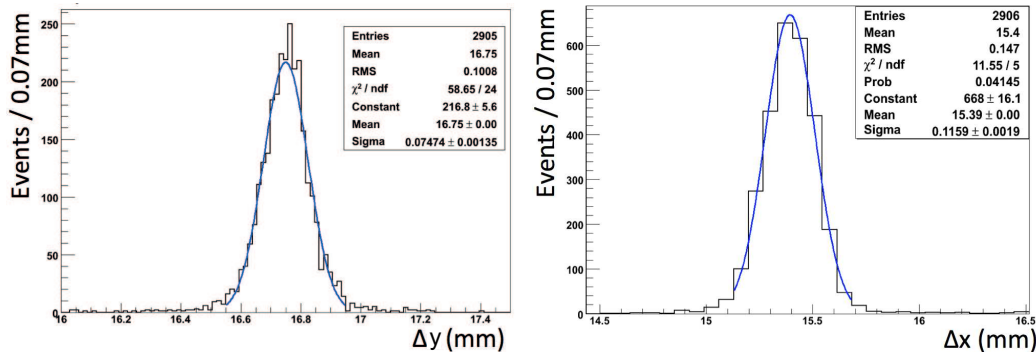


Figure 29: Left: Δy distribution for TR_5 and TR_1 . Right: Δx distribution for TR_5 and GE1/1-II using central tracks in a pion beam.

To minimize the impact of beam divergences in this spatial resolution measurement, tracks were selected to be from a 2×2 mm² spot in the center of a pion beam which is much narrower than the muon beam. Assuming that both TR_5 and TR_1 , which are constructed in the same way, have the same spatial resolutions ($\sigma_{y5} = \sigma_{y1}$) and that the beam divergence in y is negligible in the center, Fig.29 shows that we have for the width $\sigma_{\Delta y}$ of the Δy

distribution measured with these two tracker detectors:

$$\sigma_{\Delta y}^2 = \sigma_{y5}^2 + \sigma_{y1}^2 = 2 \sigma_y^2 \quad (1)$$

$$\sigma_y = \frac{\sigma_{\Delta y}}{\sqrt{2}} = 53 \mu m \quad (2)$$

Hit positions in x and y are computed from the mean (or “center-of-gravity”) of the corresponding strip cluster using the analog pulse height information for each strip. It is a reasonable assumption that $\sigma_{x5} \approx 53 \mu m$ if $\sigma_{y5} = 53 \mu m$ since in TR₅ strips in x and y have the same pitch. Consequently, the following upper bound on the spatial resolution of the GE1/1-II prototype can be established in the chamber section with smallest strip pitch at the high- η end when analog pulse height information is used:

$$\sigma_{x_{GE11}} \leq \sqrt{\sigma_{\Delta x}^2 - \sigma_{x5}^2} = 103 \mu m \quad (3)$$

Equ. (3) gives an upper bound value, as any remaining beam divergences in x still contribute to the width of the Δx distribution in Fig. 29.

Fig. 30 shows the measured shift in the average strip cluster position due to the presence of a magnetic field for the GE1/1-II prototype operated inside the M1 magnet. Measurements were performed in June and July 2011 using the SPS H2 150 GeV muon beam, with the detector flowing an Ar/CO₂/CF₄ (45:15:40) gas mixture. The angle between the GEM electric field and the external magnetic field could be varied by rotating the detector inside the M1 magnet. The data are in good agreement with a Garfield/Magboltz [16] simulation performed for a 90° angle between the magnetic field and the GEM electric field. The measurement at 1.5 T was performed for an angle of 30°, which accounts for the observed small deviation between data and simulation for that particular point.

More details on test beam results obtained with the two large-area prototypes can be found in [17].

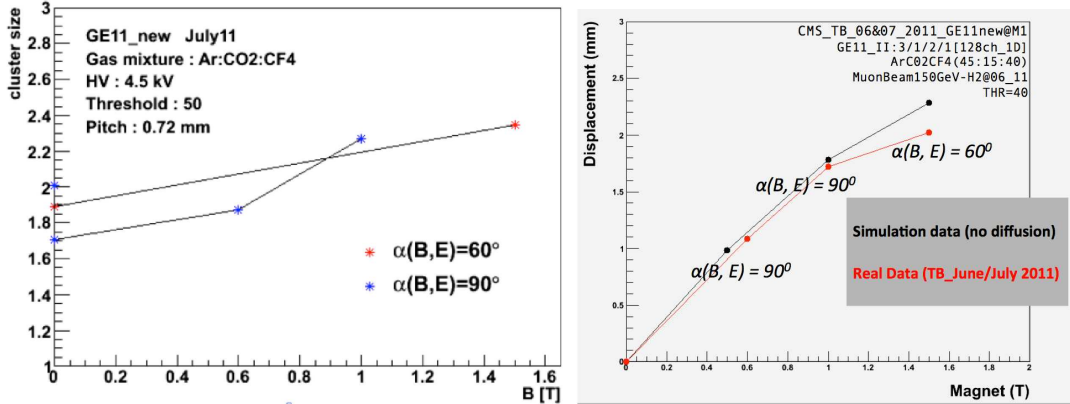


Figure 30: Left: GE1/1-II cluster sizes inside a strong magnetic field. Right: Comparison of measured and simulated strip cluster position displacement in GE1/1-II due to an external magnetic field.

3.5.4 Conclusion from measurements with full-size prototypes

Beam tests of both full-size prototypes produced very positive and promising results. The performance of the large-area prototypes with single-mask GEMs was quite similar to that of the small double-mask “Timing GEM” prototype. A significant advance was achieved with the construction and assembly of the second full-scale detector GE1/1-II even though it was technically challenging to construct a large-area GEM with transfer and induction gap sizes as small as 1 mm. Good detector performances regarding detection efficiency and spatial resolution were demonstrated and the second detector behaved as expected when operated in a magnetic field.

3.6 Present status and improved detector assembly technique

With a GEM detector geometry similar to the RPCs in the CMS endcap disks, the smallest active GEM detector area required by CMS is of the order of 100 cm × 50 cm. Depending on how many endcap disks would be

instrumented with GEMs, the number of detectors needed for CMS could be several 100's. For such quantities, the time and certainly the cost of the detector production becomes an issue.

One of the most time-consuming and labor-intensive part of Triple-GEM detector production is the GEM foil stretching and the gluing of the spacer frames. In an attempt to avoid these steps and speed up the production process, a novel assembly procedure was tested in 2011, here referred to as the “*self-stretching*” technique. The procedure is demonstrated in Fig. 31 showing a few photographs taken during the assembly of the first 10 cm × 10 cm “CMS Proto III” Triple-GEM prototype at CERN using this new technique.

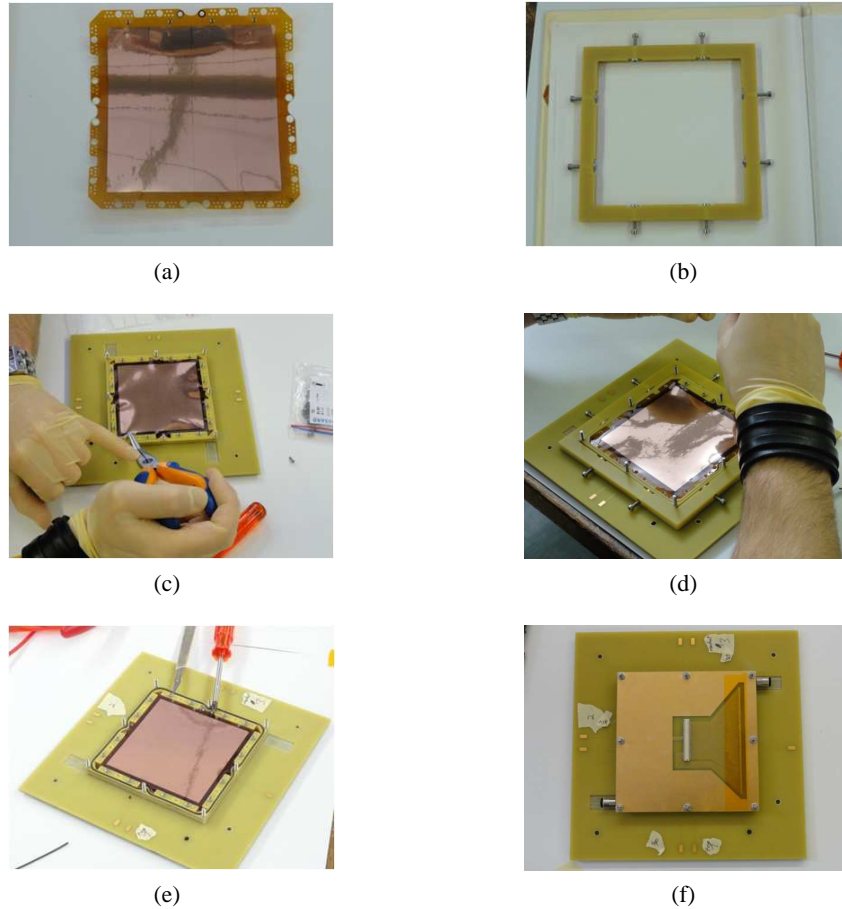


Figure 31: The *self-stretching* Triple-GEM assembly technique: (a) GEM foil before assembly; (b) external frame for foil stretching; (c) mounting the GEM foils; (d) stretching the foils; (e) stretched GEM; (f) completed detector including readout board.

The GEM foils are produced with a pattern of holes near the edge of each of the four sides of the foil. Using a special external frame that is placed around the assembly, the detector frames are pre-tensioned in such a way that they slightly bow inwards. The foils are then placed on a detector structure which has a set of alignment pins matching the hole pattern in the foil edges. After removal of the external frame, the GEM frame resumes its natural shape and the attached foils are stretched and finally fixed with screws to the detector structure and thus held in place. In the end, once the foils have been completely stretched and fixed, the readout board can be mounted, closing the detector.

Clearly, compared to the standard assembly procedure, the *self-stretching* technique offers many advantages. Neither gluing nor soldering is required during the assembly procedure and, at least in the case of a small prototype, the detector can be produced without the need to place any spacers in the active area, i.e. in the gaps between the foils. The technique is very fast; for example, the small prototype shown in Fig.31 was assembled in only one hour. As an additional benefit, this allows for the detector to be re-opened if needed in order to make modifications or repairs, or to replace a GEM foil.

The small “CMS Proto III” prototype produced in this way was tested using an x-ray gun with a Cu target in the RD51 lab. With an Ar/CO₂ (70:30) gas mixture, the detector exhibited stable operation for a measured gain up to

Table 2: Overview of all GEM detector prototypes that were constructed and studied in this project.

Name of GEM Prototype	Mask Type	Prod. Tech.	Active Area (cm ²)	r/o & Pitch (dim./mm)	Gap Sizes (D,T1,T2,I) (all in mm)	Num. of strips	Prod. Site
Timing	double	standard	10 × 10	1D 0.8	3/2/2/2 3/1/2/1	128	CERN
Single-Mask	single	standard	10 × 10	2D 0.4	3/2/2/2	512	CERN
Honeycomb	double	standard	10 × 10	2D 0.4	3/2/2/2	512	CERN
GE1/1-I	single	standard	99 × (22 – 45)	1D 0.8-1.6	3/2/2/2	1024	CERN
GE1/1-II	single	standard	99 × (22 – 45)	1D 0.6-1.2	3/1/2/1	3184	CERN
GE1/1-III	single	self-stretch	99 × (22 – 45)	1D 0.6-1.2	3/1/2/1	3840	CERN
CMS Proto III	single	self-stretch	10 × 10	1D 0.4	3/1/2/1	256	CERN
CMS Proto IV	single	self-stretch	30 × 30	1D 0.6-1.8	3/1/2/1	256	CERN
Korean I	double	standard	8 × 8	1D 0.6	3/1/2/1	256	New Flex

at least $3 \cdot 10^4$. The detector response was also observed to be very uniform across the GEM surface. Given these promising results, a larger prototype with dimensions 30 cm × 30 cm was produced with the new technique. Its gain curve and gain uniformity are shown in Fig.32. Initial tests of its performance are ongoing.

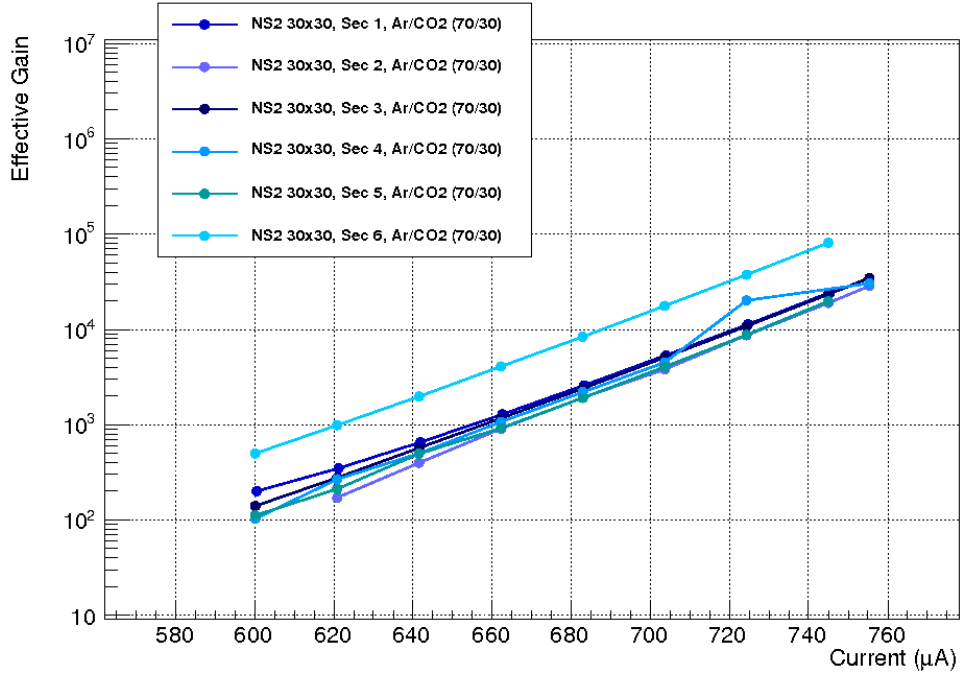


Figure 32: Gain curve of the 30 cm × 30 cm self-stretched GEM prototype detector.

As a summary of the hardware R&D described in this chapter, Table 2 lists all GEM detector prototypes constructed and tested so far. Table 3 gives an overview of the performance measurements for these prototypes with and without a magnetic field, i.e. efficiency and space and time resolutions with different gas mixture.

Table 3: Performance overview for all tested prototypes.

Name of GEM Prototype	Max. Gain	Gas Mixture	Electr.	Effic. (%)	Space res. (mm)	Time res. (ns)	Magnetic field (T)
Timing	60776	Ar/CO ₂ (70:30)	VFAT2	98.3	0.24	9.8	B=0
	17943	Ar/CO ₂ /CF ₄ (45:15:40)	VFAT2	98.8	0.24	4.5	B=0
Single-Mask		Ar/CO ₂ (70:30)	VFAT2	97.9			B=0
		Ar/CO ₂ /CF ₄ (45:15:40)	VFAT2	98.6			B=0
Honeycomb		Ar/CO ₂ (70:30)	VFAT2				B=0
		Ar/CO ₂ /CF ₄ (45:15:40)	VFAT2	70.5			B=0
GE1/1-I	15889	Ar/CO ₂ (70:30)	VFAT2	98.8			B=0
		Ar/CO ₂ /CF ₄ (45:15:40)	VFAT2	99.0	0.32		B=0
GE1/1-II	15889	Ar/CO ₂ (70:30)	VFAT2	98.9			B=0
		Ar/CO ₂ /CF ₄ (45:15:40)	APV		<0.10		B=0
	18938	Ar/CO ₂ /CF ₄ (45:15:40)	VFAT2	97.8	0.29		B=1.5
CMS Proto III		Ar/CO ₂ (70:30)	VFAT2				B=0
		Ar/CO ₂ /CF ₄ (45:15:40)	VFAT2				B=0
CMS Proto IV		Ar/CO ₂ (70:30)	VFAT2				B=0
		Ar/CO ₂ /CF ₄ (45:15:40)	VFAT2				B=0
Korean I	4653	Ar/CO ₂ (70:30)	VFAT2				B=0
		Ar/CO ₂ /CF ₄ (45:15:40)	VFAT2				B=0

4 Simulation studies

4.1 The GEM detector

The GEM detector consists of a thin metal-clad polymer foil chemically perforated by a high density of holes. The polyimide used has a dielectric constant of 3.5 and the metal used is copper. The GEM has a bi-conical hole, with outer and inner radii as $70\ \mu\text{m}$ and $50\ \mu\text{m}$ respectively and the pitch is $140\ \mu\text{m}$.

A very high electric field develops in the GEM hole which can go as high as $\sim 60\ \text{kV/cm}$, when a potential difference is applied to the two metal layers as can be seen in Fig. 33. We use a drift field region of 3 mm, and spaces of 1 mm and 2 mm in the transfer regions and a 1 mm space in the induction field region. At CMS, the gas under consideration is a mixture of $\text{Ar}/\text{CO}_2/\text{CF}_4$ in a 45 : 15 : 40 combination, similar to the gas that was used in LHCb [18].

The detector is modeled using the ANSYS software, which is a general purpose finite element modeling package for numerically solving a wide variety of mechanical problems. It can be used for solving the electric field in a complicated structure like the GEM. The elements are defined using the solid modeling method. In order to calculate the electric field, we use the free meshing method in ANSYS. ANSYS improves on the meshing used in the previous simulation by using curved elements, and is more accurate.

One element of the GEM consists of a hole in the center with four quarter holes at the edges as can be seen in the Fig. 34. The element is then extended to make a GEM detector of any size by using the periodicity feature in Garfield++[16]. In Fig. 34, one can see the single GEM modeled in ANSYS and the Triple-GEM arrangement made of single GEMs, the anode and cathode plane.

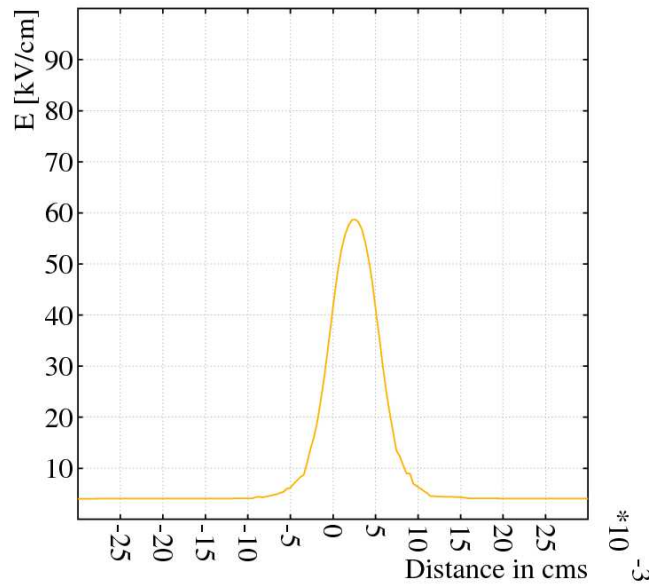


Figure 33: The electric field as seen in Garfield at the center of the GEM

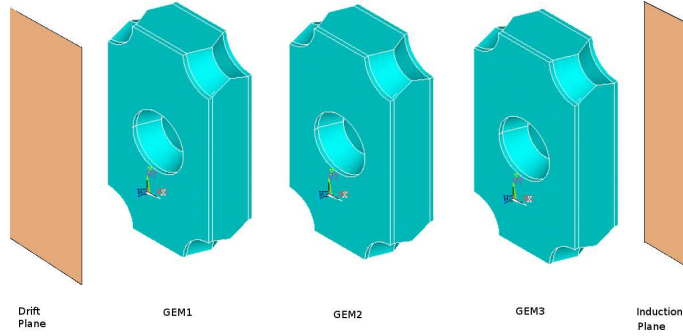


Figure 34: Exploded view of a Triple-GEM arrangement (Distances are not to scale)

4.2 Study of the transport parameters

In this section, we present studies of the transport parameters for two gas mixtures, ($\text{Ar}/\text{CO}_2/\text{CF}_4$) and (Ar/CO_2) in the ratios 45 : 15 : 40 and 70 : 30 respectively. Some discussions on transport properties in gaseous detectors can be found here[20]. Recently GEM detectors have been operated with $\text{Ar}/\text{CO}_2/\text{CF}_4$ successfully in a high rate environment in the LHCb experiment[18], and with Ar/CO_2 in a 70 : 30 ratio in the TOTEM experiment[13]. We are investigating the usage of $\text{Ar}/\text{CO}_2/\text{CF}_4$ as this gas combines a high drift velocity along with a small Lorentz angle (almost comparable to Ar/CO_2), which will be useful for triggering and other physics studies in the forward region. Also, this gas was found to give a better time resolution of ~ 5 ns as compared to Ar/CO_2 which gave a time resolution of ~ 10 ns [18]. We do a feasibility study of these gas mixtures for the CMS scenario. Since CMS has a magnetic field of 4 T in particular, we would like to study the effect of the magnetic field and the effect of the angle between the E-field and B-field.

When electrons and ions in a gas are subjected to an electric field, they move on an average along the electric field, but individual electrons deviate from the average due to scattering on the atoms and molecules of the gas. Scattering leads to variations in velocity, called longitudinal diffusion, and to lateral displacements, called transverse diffusion. The scattering process in each direction can to a good approximation be considered Gaussian on a microscopic scale. Electric field affects the transverse and longitudinal diffusion differently and so the two coefficients are plotted separately in the figures. In cold gases like carbon-dioxide for example, the diffusion is small, while drift velocity is low and unsaturated for values of electric fields which are usually used in gas detectors. Warm gases like argon on the other hand, have a higher diffusion, but when they are mixed with polyatomic/organic gases having vibrational and rotational modes, diffusion is reduced in most cases, while the drift velocity is increased.

Fig. 35 shows the diffusion coefficients for two gas mixtures as a function of the electric field. As can be seen from the plot, the diffusion in the mixture $\text{Ar}/\text{CO}_2/\text{CF}_4$ is lower, as expected, because of a higher polyatomic gas component; both CF_4 and CO_2 having vibrational modes which contribute to lowering the diffusion. CF_4 is advantageous to use in a high-rate environment because of its high drift velocity but it suffers from electron attachment. Therefore CO_2 is used to “cool” the electrons and reduce the electron attachment which occurs in CF_4 .

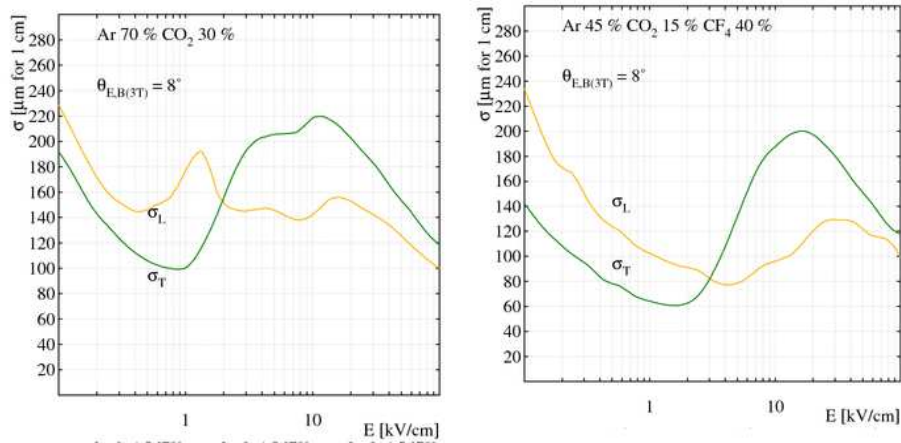


Figure 35: Diffusion coefficient for two different gas mixtures under study in presence of magnetic field and with angle $\theta(E, B) = 8^\circ$

In Fig. 36, the diffusion coefficients can be seen for magnetic fields of 0 T and 3 T. The effect of the magnetic field is to reduce the transverse diffusion coefficient w.r.t to its direction, while the longitudinal coefficient is unchanged. This effect is seen in the two figures.

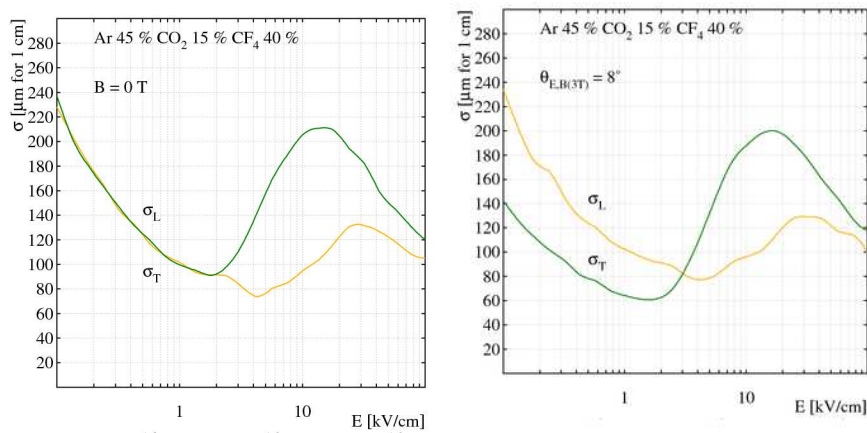


Figure 36: Diffusion coefficients for magnetic fields = 0T and 3T with $\theta(E, B) = 90^\circ$.

In the presence of both an electric field, and a magnetic field, the electrons are deflected due to the magnetic field and drift along a direction at an angle to the electric field, called the Lorentz angle. It is the angle between the electric field and drifting electron. Too large a Lorentz angle leads to worsening of the spatial resolution, although a small Lorentz angle may give better spatial resolution due to charge sharing in the readout strips. Knowledge of this angle is important in order to correct for this effect and improve spatial resolution. The Lorentz angle can be seen in Fig. 37, for the gas mixture Ar/CO₂/CF₄ for two $\theta_{(E,B)}$ angles in order to show the expected range of Lorentz angles we can expect in this gaseous mixture.

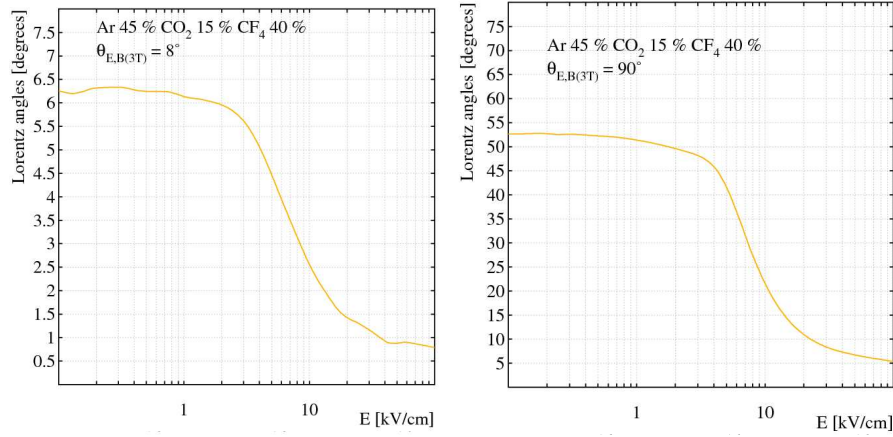


Figure 37: Lorentz angles for the gas mixture Ar/CO₂/CF₄ for the angles $\theta(E, B) = 8^\circ$ (left) and $\theta(E, B) = 90^\circ$ (right) for a magnetic field of 3 T.

The diffusion effect leads to variations in drift velocity. In Fig. 38, one can see that the simulation results for different gas mixtures compared with experimental LHCb test beam results[18]. It can be seen that the mixture Ar/CO₂/CF₄ is a faster gas on account of addition of the CF₄ gas.

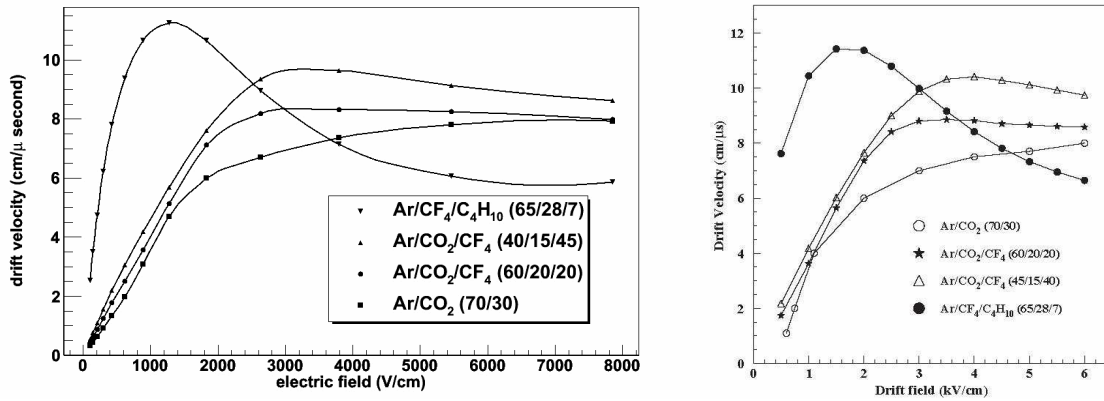


Figure 38: The drift velocities for various gas mixtures from simulation and the experimental values from LHCb studies. The simulation shows a good agreement with the experimental results

4.3 Gain studies

When an electron enters the GEM hole, under the influence of the high electric field it gains enough kinetic energy between two successive collisions to further ionize the argon and more and more free charges are produced rapidly. The primary electron therefore produces an “avalanche” under the influence of the high electric field. This increase in the number of electrons is also called gain. In this section we study the gain and losses in a single GEM for Ar/CO₂/CF₄. We then compare it with Ar/CO₂. We then study the gain for a Triple-GEM and compare it with test beam data.

Even after 10 \approx years since the invention of the GEM detector, gas gain is still not very well understood. However, in a very recent approach[16], microscopic tracking has been used, which tracks electrons from one collision with a gas molecule to the other using Monte Carlo methods. The electron-gas interaction takes into account the processes of elastic scattering, attachment, excitation and ionization. Electrons with an energy above the excitation threshold can lift an electron of an argon atom to a higher energy state. The excited states undergo radiative decay but excited noble gas atoms are more aggressive and can alternatively de-excite by transferring their excess energy to a quencher molecule which may even get ionized if the energy transfer exceeds its ionization potential. We study the effect of this process, called Penning transfer [21],[22],[?], in the Ar/CO₂ gas. A previous paper[19] has done a detailed gain study which includes the effect of Penning transfer in Ar/CO₂ gas. It was shown that the Penning transfer can play a big role. The issue under study here was whether it plays a similar role in Ar/CO₂/CF₄ gas,

where we have a higher percentage of CF_4 than CO_2 . A more detailed study is underway for the effect of CF_4 gas in GEMs and other detectors.

4.4 Avalanche simulation

The studies done here use “single-electron” avalanches as also described in the paper[19]. We generate a stack of single electrons randomly at a distance of $250 \mu\text{m}$ in the z-direction, from the GEM. The plane lies in the x-y direction. The electron is given an initial energy of 0.1 eV and a random initial direction of motion. Then one of the processes listed above is selected at random, weighed by their relative probability considering the electron energy at the time of the collision. An additional electron is added to the stack in case of Penning transfer or ionization; the electron is removed from the stack in case it is attached or attempts to leave the drift medium. The process is repeated until the stack is exhausted.

The total gain, G_{tot} which is the total number of electrons produced in the avalanche, differs from the measured or effective gain G_{eff} because the latter is derived solely from the current in the anode plane. Avalanche electrons which terminate on the GEM electrodes or insulator do not contribute to the anode current and hence G_{eff} is always smaller than G_{tot} . The “single-electron” avalanche simulation has been repeated at least 1000 times for varying GEM voltages and Penning parameters. All simulations were performed at standard temperature and pressure, i.e. $T_0 = 293.15 \text{ K}$, $P_0 = 1 \text{ atm} = 760 \text{ Torr}$.

Some of the primary electrons are lost due to attachment to the gas molecules (attachment loss) or to the metal (geometric loss). The losses due to attachment and due to geometric losses can be seen in Fig. 39. The attachment loss as expected is independent of the GEM potential difference, while the geometric losses decrease with increasing GEM potential (or higher electric field), as electrons are accelerated and sucked into the GEM hole faster with increasing electric fields. This leads to lower geometric losses. The attachment loss is $\sim 12\%$ in this gas mixture.

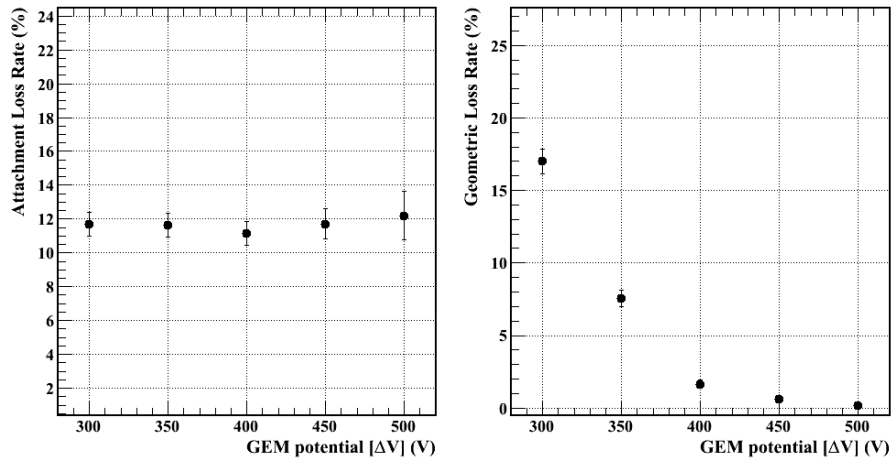


Figure 39: Loss rate for primary electrons for $r_p = 0.6$. The losses occur due to attachment to the quencher gas molecules (left) and due to the electrons hitting the surface of copper metal or polyimide walls (right)

The electrons which make it into the GEM hole give rise to the avalanche. All of these secondary electrons do not contribute to the signal as some are lost on hitting the walls of the polyimide or hitting the copper metal and some are lost due to attachment to the gas molecules. The losses due to attachment and due to geometric losses can be seen in Fig. 40. The geometric loss increases with increasing GEM potential because the electrons exiting the hole are attracted back by the lower copper metal which is positive with respect to the upper copper metal plate. The secondary attachment loss reduces to $\sim 8\%$ as the electrons gain energy inside the GEM hole due to the high electric field inside the hole.

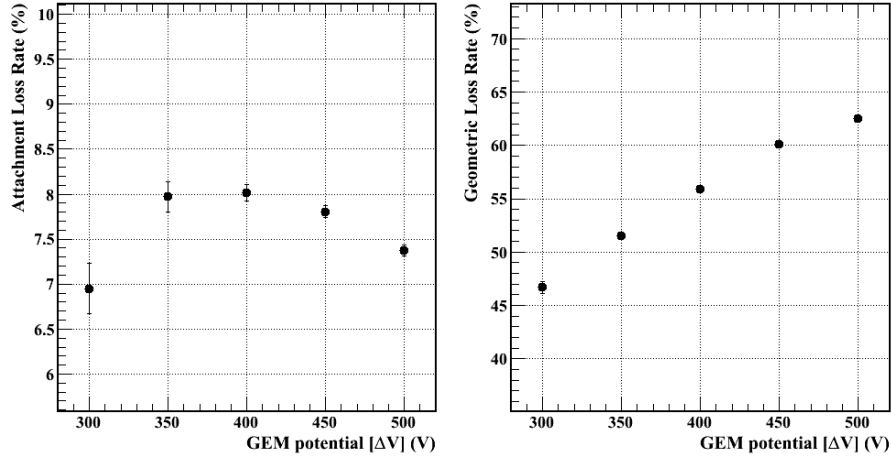


Figure 40: Loss rate for secondary electrons. The losses occur due to attachment to the quencher gas molecules (left) and due to the electrons hitting the surface of copper metal or polyimide (right)

The overall loss of the primary and the secondary electrons can be seen in the Fig. 41.

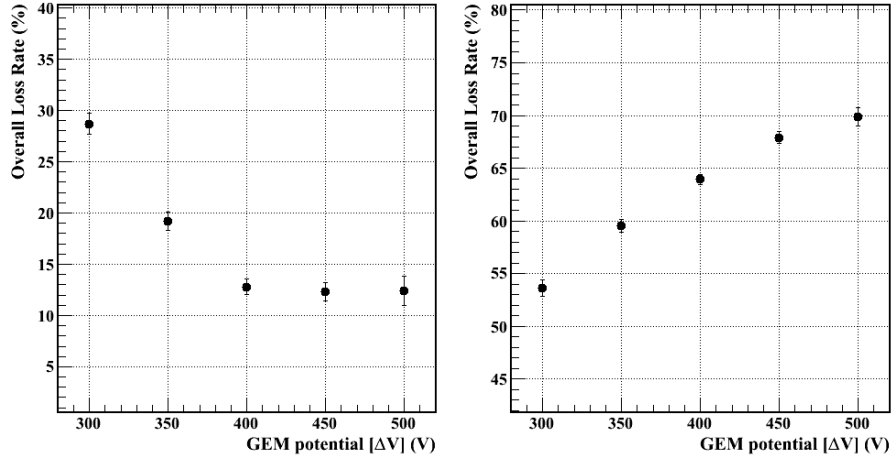


Figure 41: Overall Loss rate for primary (left) and secondary (right) electrons for penning parameter $r_p = 0.6$

If l_p and l_s are the primary and secondary electron losses, then we can define the collection efficiency (which is the efficiency of the electrons to make it into the hole), as $\epsilon_{coll} = 1 - l_p$, and the extraction efficiency (which is the efficiency of secondary electrons to make it out of the GEM hole), as $\epsilon_{extr} = 1 - l_s$.

The effective gain (G_{eff}) is then defined as :

$$G_{eff} = \epsilon_{coll} \times \epsilon_{extr} \times G_{tot}$$

The effective gain and total gain can be seen in Fig. 42. It is shown for different values of the Penning parameter.

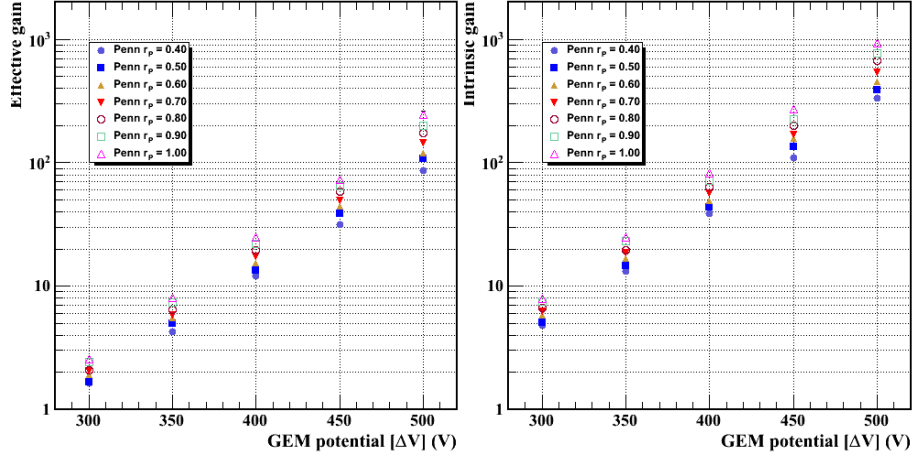


Figure 42: Effective gain (G_{eff}) and the total gain (G_{tot}) for different penning parameters.

A comparison of the effective gain with Ar/CO₂ can be seen in Fig. 43 for one penning parameter $r_P = 0.6$. As can be seen, the effective gain reduces considerably in the case of Ar/CO₂ by a factor of 1/2. However, we are using Ar/CO₂/CF₄ because CF₄ being a fast gas gives fast response and an improved time resolution. The time resolution obtained in the case of Ar/CO₂/CF₄ and Ar/CO₂ can be seen in Fig. 45. The average time in case of Ar/CO₂/CF₄ is 23 ns with a resolution of 0.5 ns while for Ar/CO₂, it is 33 ns with a resolution of 1.2 ns. However, the figures in 45 do not show a realistic time resolution because we have not done a primary particle ionization simulation and it just shows the effect of using CF₄ gas.

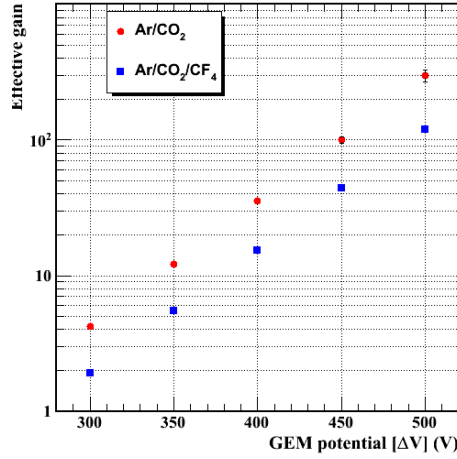


Figure 43: Effective gain comparison for Ar/CO₂/CF₄ and Ar/CO₂ for penning parameter of 0.6

In order to study the Triple-GEM, we simulate three single GEMs and the overall gain G_{tgem} , is defined as :

$$G_{tgem} = G_1 * G_2 * G_3$$

, where G_1 , G_2 and G_3 are the single GEM gains. The Triple-GEM results compared with the gain obtained in GE1/1 prototype II of CMS is seen in the Fig. 44 for the different penning parameters. As can be seen, for a penning parameter of $r_P = 0.6$, a good agreement is obtained for the different overall potentials of the Triple-GEM configuration as compared to data.

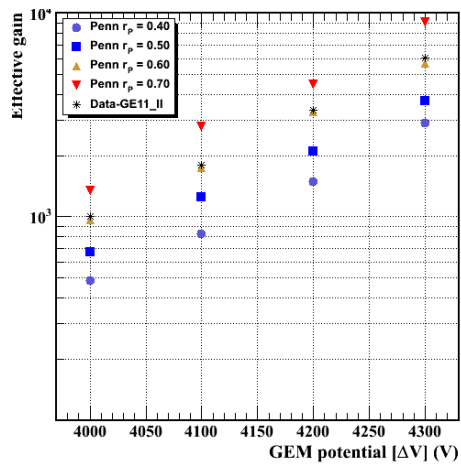


Figure 44: Triple-GEM effective gain compared with data

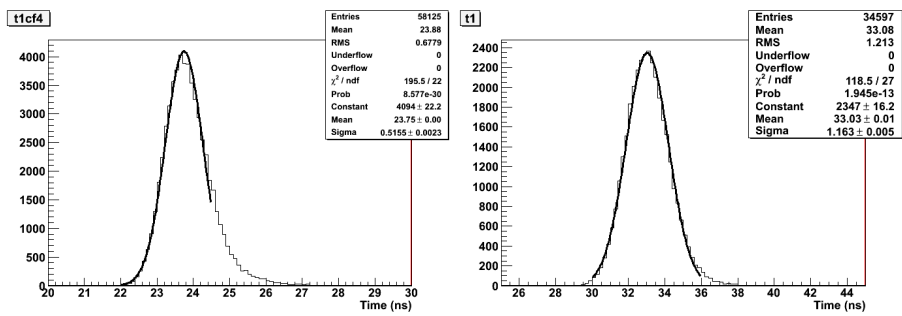


Figure 45: Time resolution for single electrons in the case of Ar/CO₂/CF₄ (left) and Ar/CO₂ (right)

5 Muon triggering with GEM detectors in the high- η region

One of the main objectives of the proposed GEM detector system is to provide an additional muon trigger source redundant with the CSC trigger to ensure robust triggering on forward muons at the high luminosity LHC and beyond. In this section, we give a brief overview of the existing RPC trigger system followed by initial results from an GEM trigger emulation study, which is derived from the existing CMS RPC trigger emulation.

5.1 Trigger emulation

The Resistive Plate Chamber (RPC) trigger is one of the Level-1 (L1) muon subtriggers used in the CMS experiment. The goal of the L1 RPC trigger is to identify high p_T muons produced near the interaction point, determine the bunch crossing they originate from, estimate their transverse momenta, and provide information on how good this momentum determination by calculating a “muon candidate quality” figure-of-merit. Muon candidates found by the RPC trigger are sent to the Global Muon Trigger (GMT), which matches candidates sent by RPC, CSC, and DT triggers.

The RPC trigger identifies muons by comparing RPC hits with predefined sets of patterns using Pattern Comparator (PAC) chips. The number of planes in which a measured pattern matches predefined patterns determines the muon candidate quality; matches in higher number of planes mean higher quality. Since a single muon may be found by different (neighboring) PAC chips, a procedure called “ghostbusting” is applied to remove extra (“ghost”) muon candidates leaving the one with the best momentum measurement; i.e. only the muon candidates with the highest quality are kept.

Since multiple muons may be produced in the interaction point and since the RPC trigger is supposed to send no more than eight muon candidates (four for the barrel region and four for the endcap regions), an additional procedure called “sorting” is needed for selecting the best muons. This selection is based on muon candidate quality and assigned momenta. Sorting and ghostbusting procedures are done simultaneously by a sorting/ghostbusting tree at different levels in RPC Trigger Board Sorters, Trigger Crates Sorters, two Half Sorters, and a Final Sorter. Further information on RPC Trigger logic and its implementation in hardware can be found in [23].

GEM chambers are characterized by very fine readout granularity. For this first simulation, we make the assumption that the trigger is to be derived by the same or a very similar trigger hardware system based on PAC chips as the current RPC trigger. Since the PAC chips have limited pattern capacity, the RPC trigger would then have to receive signals from GEM chambers that are logical OR’s of several neighboring GEM strips. We are not necessarily proposing to make this a requirement. Alternatively, CMS could consider designing a new L1 GEM trigger system fully tailored to GEM capabilities. However, we use the existing RPC trigger geometry and logic and the RPC trigger emulation as our starting point for the GEM trigger studies.

In addition to the basic analysis presented below, two or more layers of GEM-like chambers in one muon station may provide an independent precise measurement of a local track bending angle. Benefitting from full GEM chamber resolution locally available to a GEM-based trigger, such a measurement may be used at the end of the trigger logic to further constrain the momentum of reconstructed track candidates. This kind of improvement applies mainly to station GE1/1, but it can be also used in other parts of the muon system where the muon trigger has difficulties. A substantial gain in momentum resolution at the trigger level may be obtained by replacing the RPCs in RE1/2 and RE1/3 with GEMs. In addition, an extra layer of GEM-like chambers in the pseudorapidity range $1 < |\eta| < 1.6$ placed just in front of or behind the CMS coil may substantially improve CMS muon triggering capabilities. However, these more advanced potential extensions of GEM usage in the trigger are not included in the initial studies described below.

In order to fully benefit from the bending power of the magnetic field between the two innermost stations (GE1/1 and GE2/1), the muon quality definition was optimized. Muon candidates built from patterns matching in all four muon stations are preferred, with the quality value set to 2. If the pattern matches in the first two layers GE1/1 and GE2/1 and in either one of the two outermost layers (3/1 or 4/1), the muon candidate receives a lower value of quality (1). In all other cases, when the pattern matches in three planes, the muon candidate receives the lowest value of quality (0). If the pattern matches in fewer than three planes, no muon candidate is found.

Patterns used in this study were generated using the standard procedure, i.e. the same as used for pattern generation for data taking, independently for all tested geometry variations. In order to avoid negative effects due to reconstruction of low p_T with low quality with high assigned transverse momentum, a “wide” pattern was inserted to all pattern sets (for all tested geometry variations). As a result, all muons that left hits in all four planes and that do not have any pattern matching in all four planes, will be assigned the lowest transverse momentum possible.

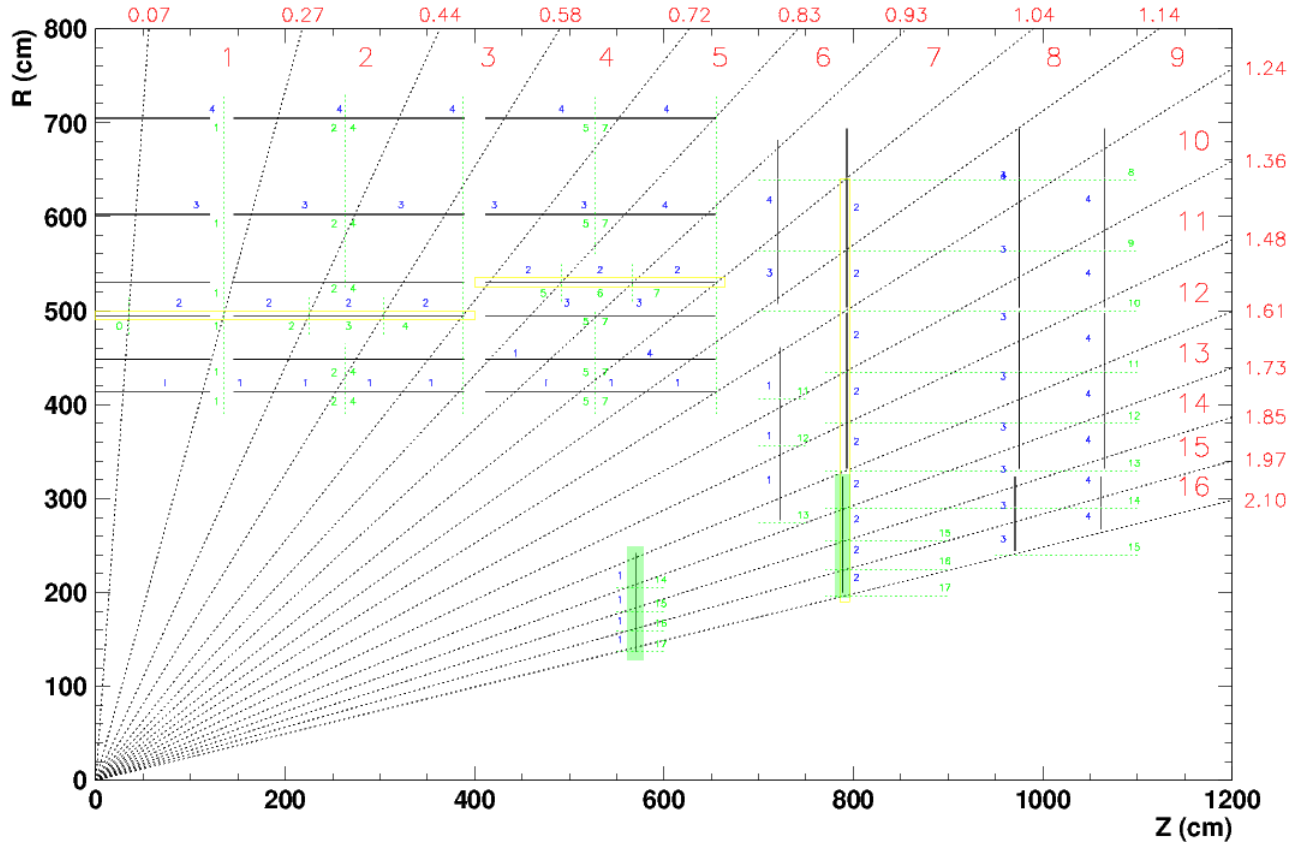


Figure 46: Longitudinal view of the current RPC trigger towers in one quadrant of the CMS detector. Chambers in areas marked with green (RE1/1, RE2/1) were modified to have increased number of strips to simulate the use of GE1/1 and GE2/1 GEM stations in those locations.

Extensive information on pattern generation can be found in [26].

5.2 GEM geometry

The RPC trigger emulation in the standard CMS experiment software framework (CMSSW, [25]) was used without major changes. During trigger emulation, the RPC trigger logic was enabled only in trigger towers 13-16, which is the region where the RPC geometry was changed to a GEM-like geometry. A modified version of the baseline TDR CMS detector geometry [27] was used, with four fully instrumented chamber planes present in the endcap regions with $|\eta|$ coverage up to 2.1. The potential range extension up to $|\eta| = 2.4$ as discussed above has not yet been implemented in the emulation as this extended range was not part of the original design geometry for the RPCs.

Fig. 46 shows the RPC trigger tower segmentation in a longitudinal view of one quadrant of the CMS detector as given in the original Muon TDR. The geometry description of chambers RE1/1 and RE2/1 marked by green rectangles was modified by increasing the number of strips in these layers to emulate the higher granularity of GE1/1 and GE2/1 GEM chambers. For this study, the number of strips in the RPC chambers in the third and fourth endcap layer (RE 3/x and 4/x) was not changed since the bending power of the magnetic field is small in this region when compared to the region where RE1/1 and RE2/1 are located.

In total 4 different strip readout geometries were tested:

- **base** - baseline RPC design geometry as outlined in the Muon TDR ([27])
- **2×** - geometry with two times higher number of strips in RE1/1 and RE2/1
- **4×** - geometry with four times higher number of strips in RE1/1 and RE2/1
- **8×** - geometry with eight times higher number of strips in RE1/1 and RE2/1

5.3 Simulated chamber properties

The trigger studies were done in two stages. In the first stage, the impact of changes in geometry was tested while assuming perfect chamber operation, both for GEM and RPC chambers, i.e. no noise, no clusters (charged particle always fires exactly one strip), and 100% chamber efficiency, i.e. the “ideal” chamber model. In the second stage, chamber effects were included in a “realistic” chamber model. Here the simulated chamber efficiency was taken as 95%, an average cluster size of two was used for RPC chambers while for the GEM chambers the clustering remained disabled. The latter choice was motivated by the assumption that the RPC trigger will not use the full GEM chamber granularity. In this model, the simulation of noise still remained disabled for both types of chambers since it is hard to estimate expected noise in the GEM chambers at this point.

5.4 Results

Fig. 47 and 48 show the dependence of GEM+RPC L1 trigger output rates on the p_T threshold for all simulated geometries. The shape of the single-muon input rate as function of p_T is generated based on the shape in Ref. [24] and normalised to $10^{34} \text{cm}^{-2} \text{s}^{-1}$ luminosity. Results sum trigger rates for trigger towers -16 to -13 and 13 to 16. The overall rate is dominated by muon candidates with lowest quality 0. This effect is visible for all geometries; it is higher for the realistic chamber model when compared to the ideal one. This is not surprising since due to the definition of “quality” the muon candidates with quality 0 use only one muon trigger station for momentum measurement and do not benefit from increased spatial resolution. Consequently, only contributions from muon candidates with qualities 1 and 2 will be considered further in our discussion.

The most important result observed in these plots is that the rate for muon candidates with higher qualities 1 and 2 flattens out above $p_T = 26 \text{ GeV}/c$ for the RPC-only “base” geometry. By contrast, in the $2\times$, $4\times$, and $8\times$ scenarios that make use of GEM chambers, the rate continues to decrease with increasing p_T threshold. This indicates that a L1 trigger upgraded with information from GEM chambers allows continued use of the p_T trigger threshold as a powerful tool to control muon trigger rates.

We also find that the higher the strip readout granularity, the lower the muon trigger rates for a given p_T threshold. Fig. 49 shows the total L1 GEM+RPC trigger output rate as a function of different geometries for different p_T thresholds and for both chamber simulation models. The contribution from muon candidates with low quality 0 is not included here. The biggest relative improvement occurs when going from the base geometry to the $2\times$ geometry. A further increase in the number of strips lowers the rate further, but the relative improvement is smaller due to a non-linear dependence. The number of trigger patterns grows with the number of strips used. Since the existing PAC chips have limited capacity, a full upgrade of the PAC system, in the future, could match the GEM installation schedule in such a way that it exploits the capabilities of the combined system.

Fig. 50-53 show the simulated trigger turn-on curves for trigger tower 13³⁾, i.e. the L1 trigger efficiencies for all geometry variations and for three different p_T thresholds (16, 50, and $140 \frac{\text{GeV}}{c}$) as a function of the true muon transverse momentum. The efficiency curves get worse in general for higher tower numbers due to the decreasing bending power of the magnetic field. The turn-on curves become much sharper as the GEM strip granularity increases. The higher the p_T threshold, the more dramatic the effect. For instance, with a $140 \frac{\text{GeV}}{c}$ threshold, the current “base” RPC trigger accepts typically over 80% of all muons with a momentum of just $60 \frac{\text{GeV}}{c}$ or higher, i.e. the RPC trigger rejection with this high threshold is actually very ineffective. This is because the current RPC pattern trigger has difficulties distinguishing the momenta of very straight tracks from each other due to its coarse granularity. For the $8\times$ GEM+RPC geometry, this 80% point with a $140 \frac{\text{GeV}}{c}$ threshold moves up to 120-140 $\frac{\text{GeV}}{c}$ making the L1 trigger rejection much more effective.

From these first simulation studies we conclude that the GEM detector stations would significantly improve the L1 muon trigger performance over that of the originally planned RPC-only system in the forward direction $|\eta| > 1.6$.

³⁾ Results for trigger towers 14-16 can be found in appendix D

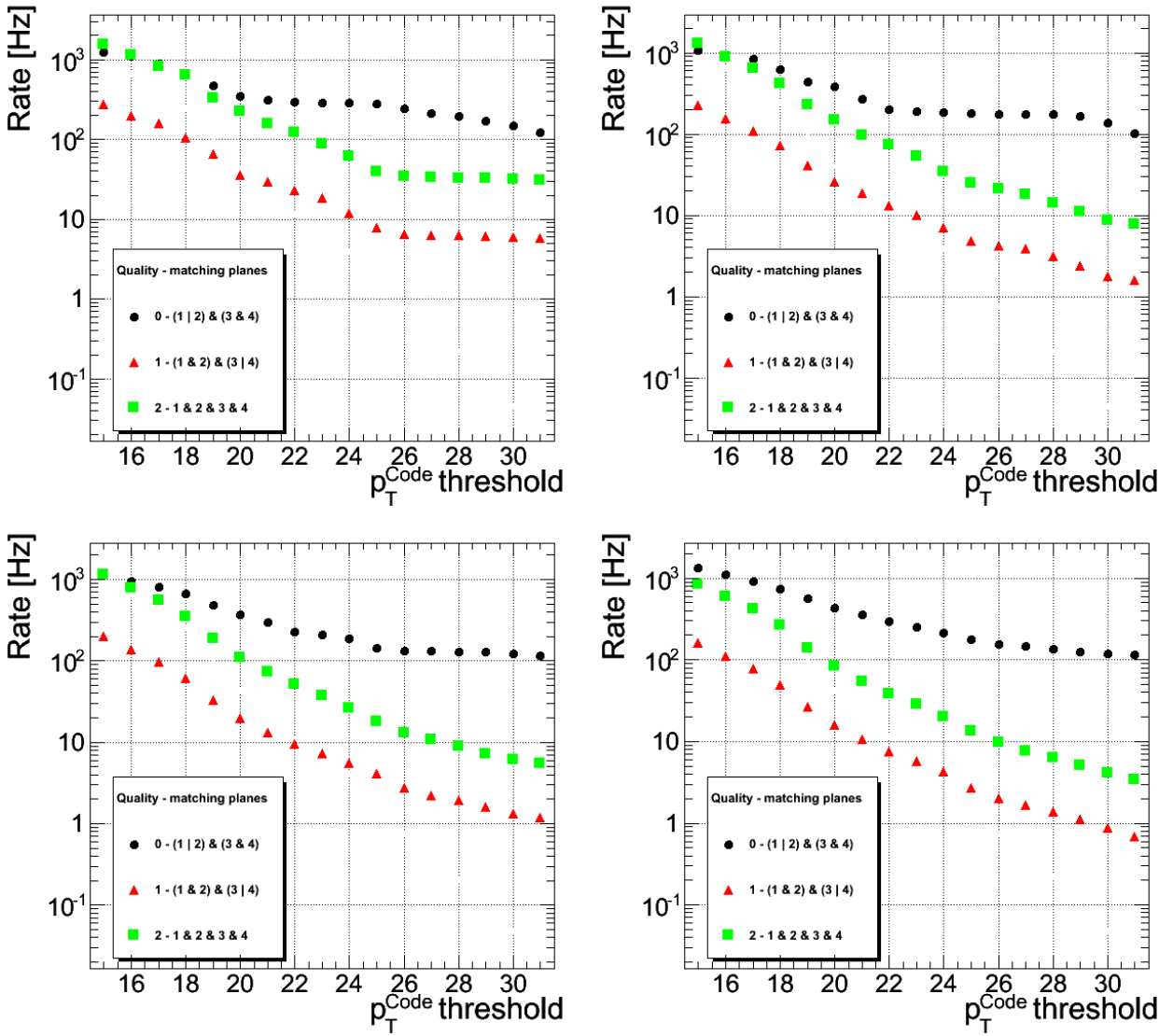


Figure 47: Simulated L1 GEM+RPC trigger output rates summed over trigger towers -16 to -13 and 13 to 16 vs. p_T cut for ideal chamber model (top left: base, top right: $2\times$, bottom left: $4\times$, bottom right: $8\times$ strip granularity).

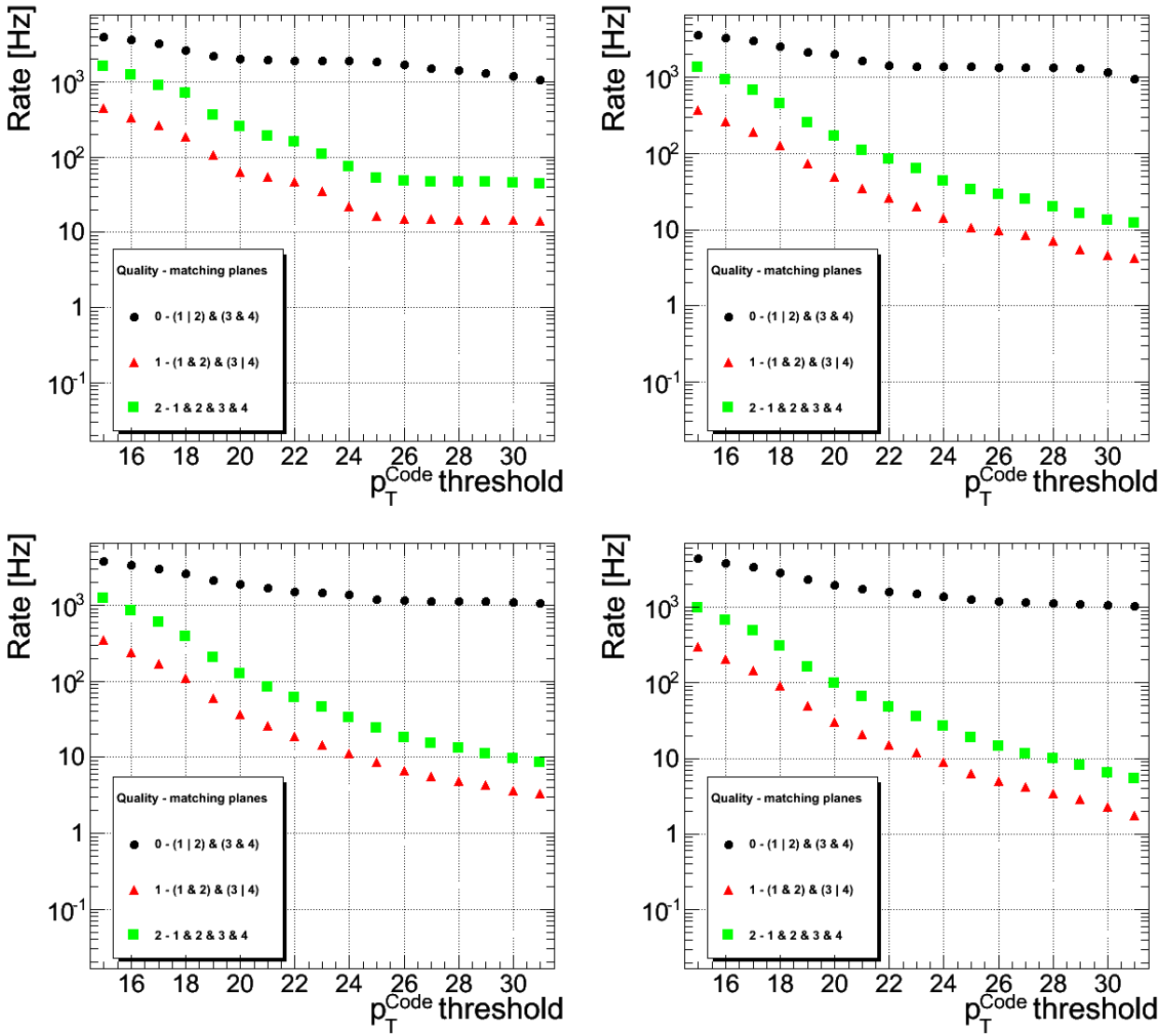


Figure 48: Simulated L1 GEM+RPC trigger output rates summed over trigger towers -16 to -13 and 13 to 16 vs. p_T cut for realistic chamber model (top left: base, top right: $2\times$, bottom left: $4\times$, bottom right: $8\times$ strip granularity).

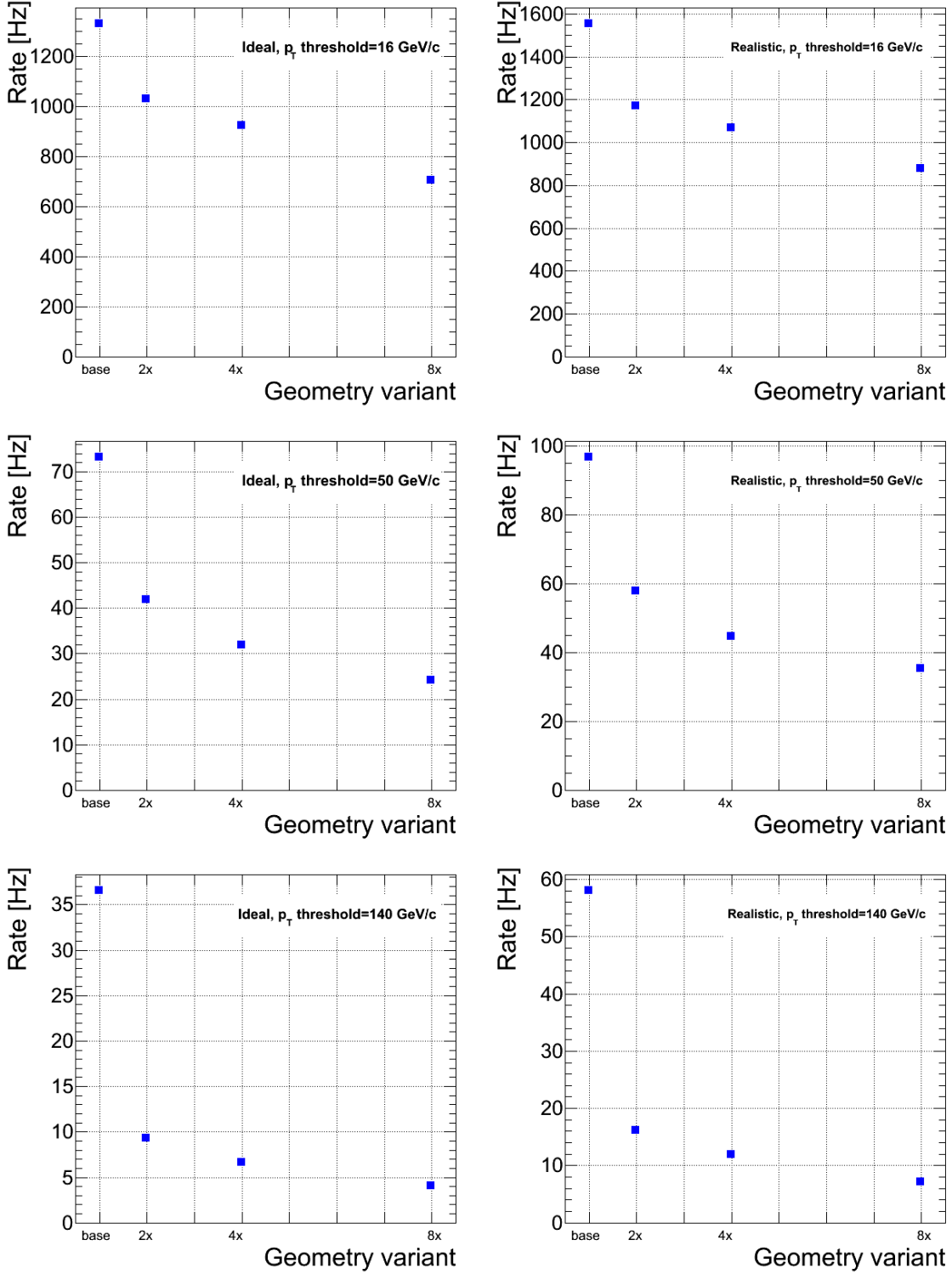


Figure 49: Simulated total L1 GEM+RPC trigger output rates as function of different geometries for ideal (left) and realistic (right) chamber models. Rows correspond to three different p_T thresholds of 16, 50, and 140 $\frac{\text{GeV}}{c}$. Only the contribution from muon candidates of quality 1 or 2 is shown.

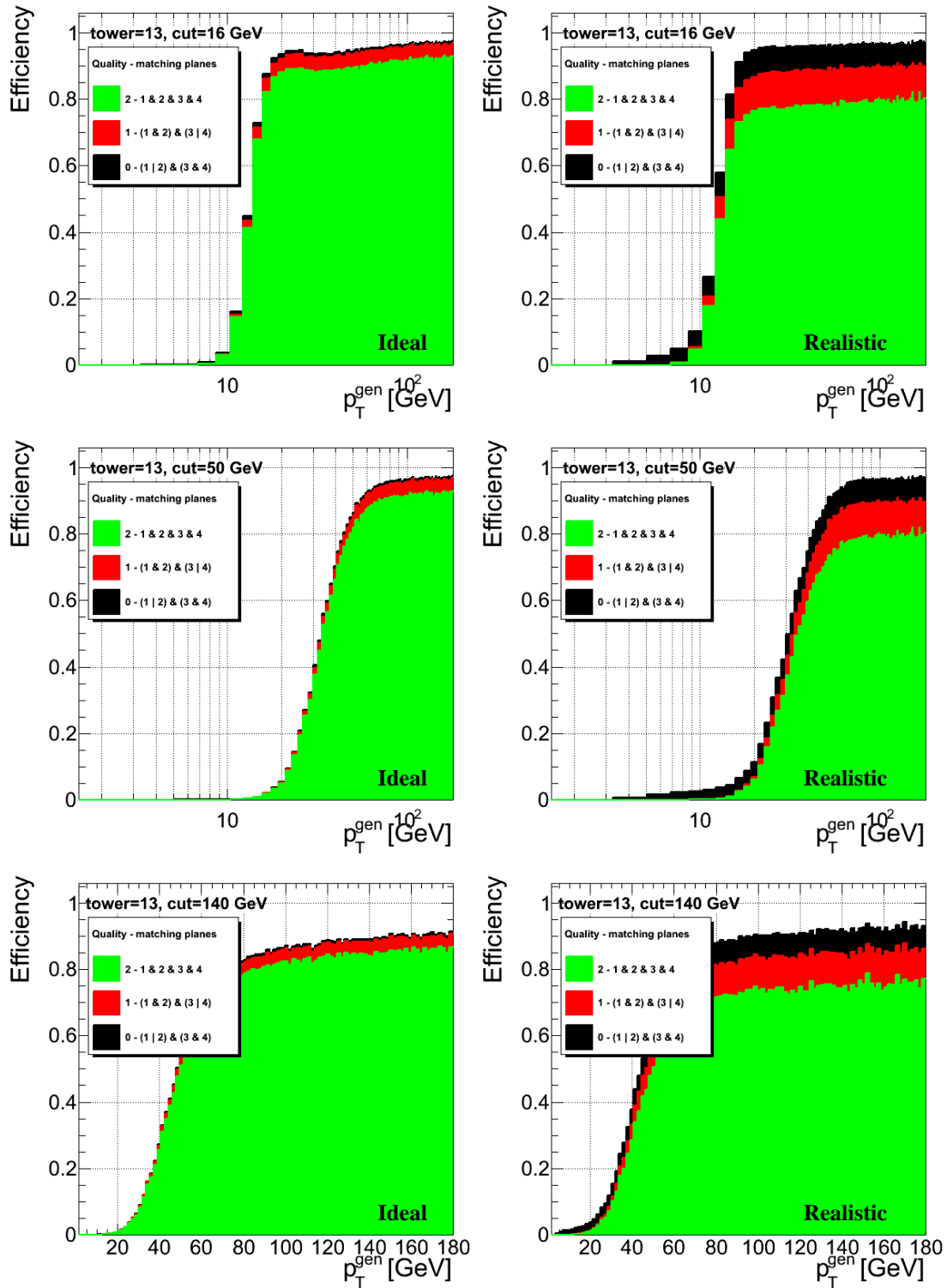


Figure 50: L1 GEM+RPC trigger efficiency curves in trigger tower 13 for base geometry. Rows correspond to 3 different p_T thresholds of 16, 50, and 140 $\frac{\text{GeV}}{c}$, respectively. Left column shows results for ideal chamber model, right for realistic chamber model.

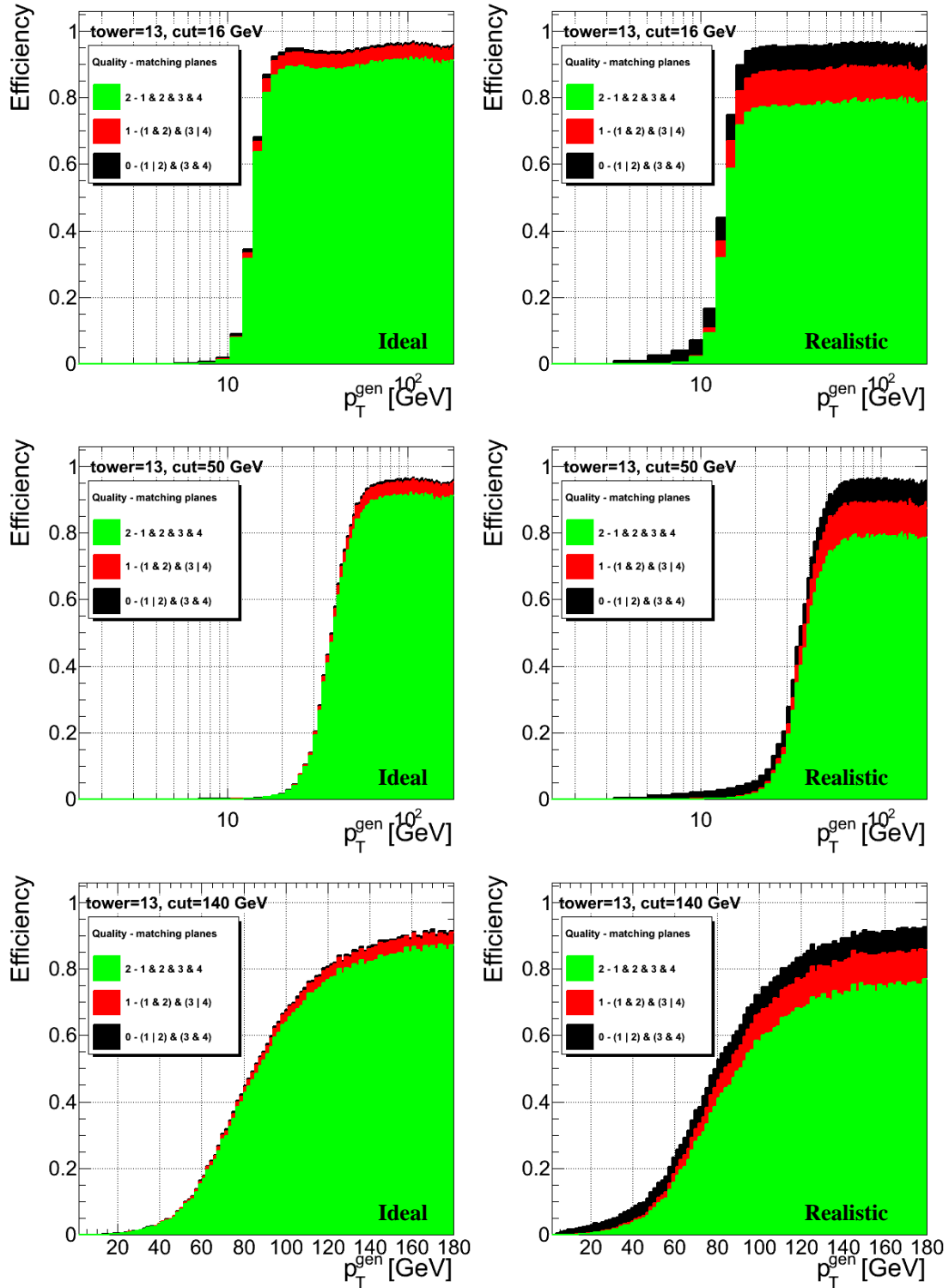


Figure 51: L1 GEM+RPC trigger efficiency curves in trigger tower 13 for $2\times$ geometry. Rows correspond to 3 different p_T thresholds of 16, 50, and 140 $\frac{\text{GeV}}{c}$, respectively. Left column shows results for ideal chamber model, right for realistic chamber model.

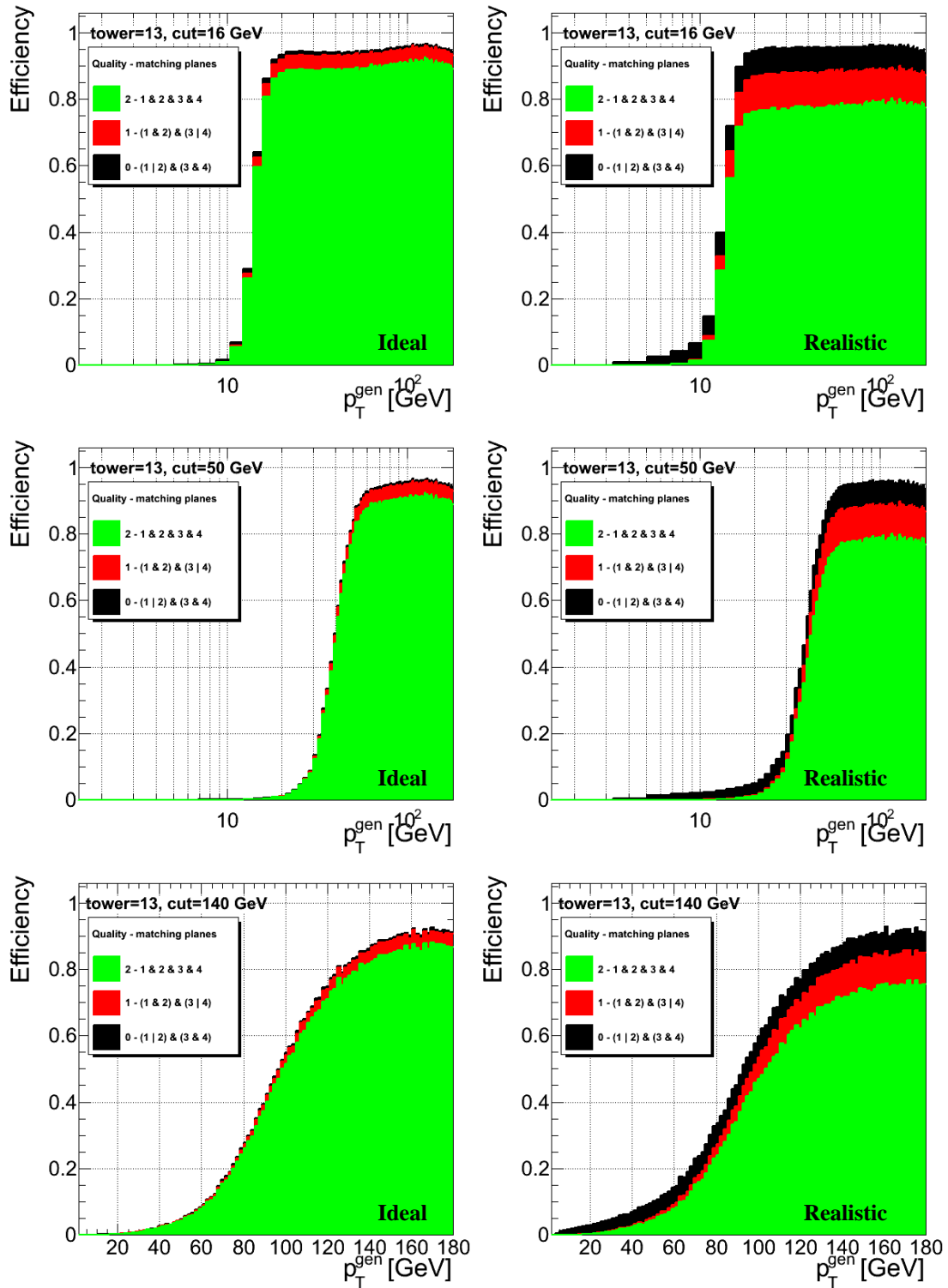


Figure 52: L1 GEM+RPC trigger efficiency curves in trigger tower 13 for $4\times$ geometry. Rows correspond to 3 different p_T thresholds of 16, 50, and 140 $\frac{\text{GeV}}{c}$, respectively. Left column shows results for ideal chamber model, right for realistic chamber model.

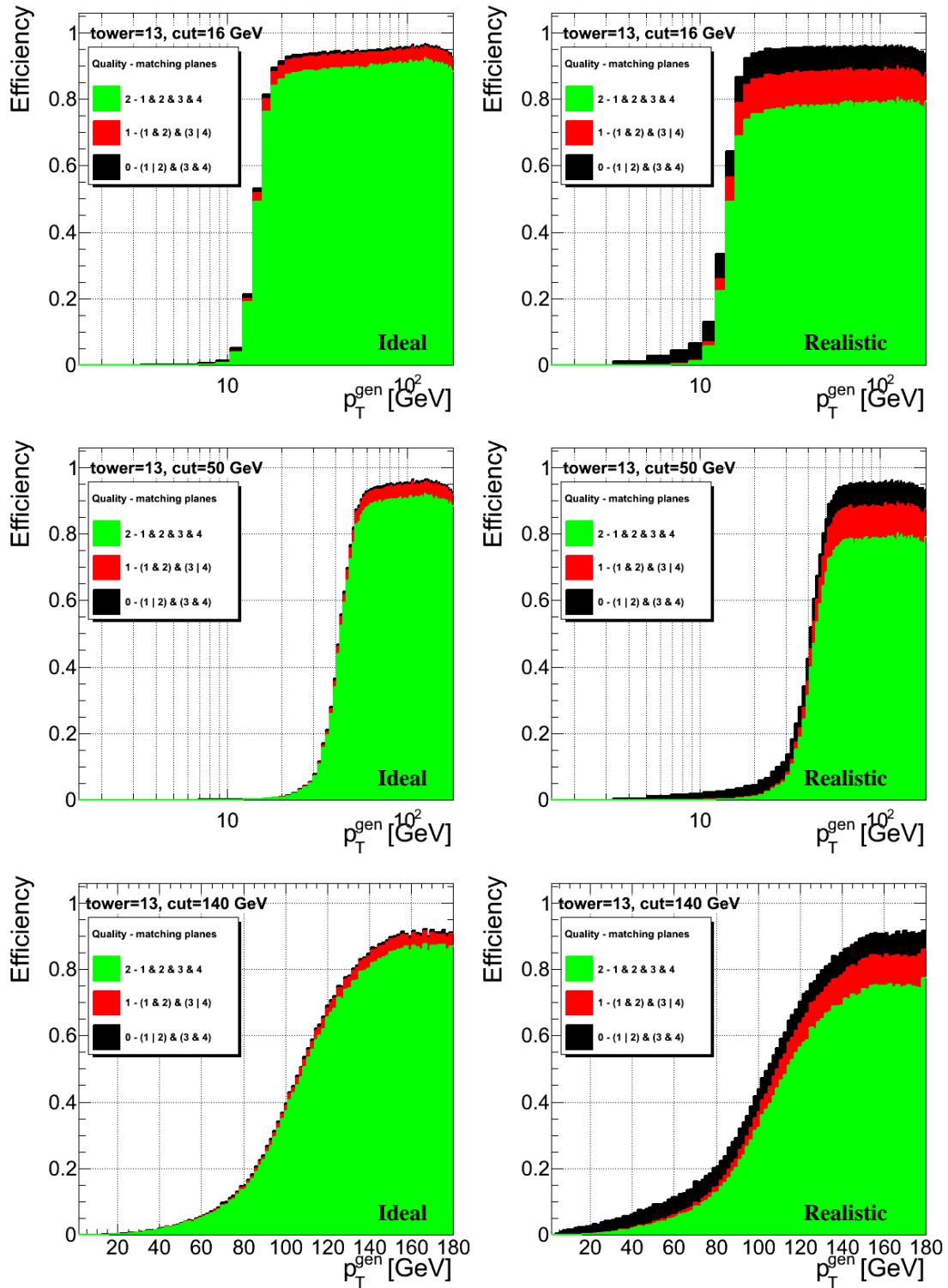


Figure 53: L1 GEM+RPC trigger efficiency curves in trigger tower 13 for $8 \times$ geometry. Rows correspond to 3 different p_T thresholds of 16, 50, and 140 $\frac{\text{GeV}}{c}$, respectively. Left column shows results for ideal chamber model, right for realistic chamber model.

5.5 Assembly laboratory (TIF - Tracker Integration Facility, building 186)

TIF (Fig. 54) is a laboratory located at CERN Meyrin site in building 186. It has one of the largest clean rooms (class 10000) and is planned to be used for assembly the Triple-GEMs for stations GE1/1 and GE2/1.



Figure 54: Building 186 view.

In Fig. 55 is shown the tentative plan of the assembly laboratory which is part of the big clean room. For GEi/1 project we have 90m² from the total laboratory area. It has special entrance access needed for the clean room conditions and also a big transport portal suitable for big transportation needs for materials and chambers deliveries.

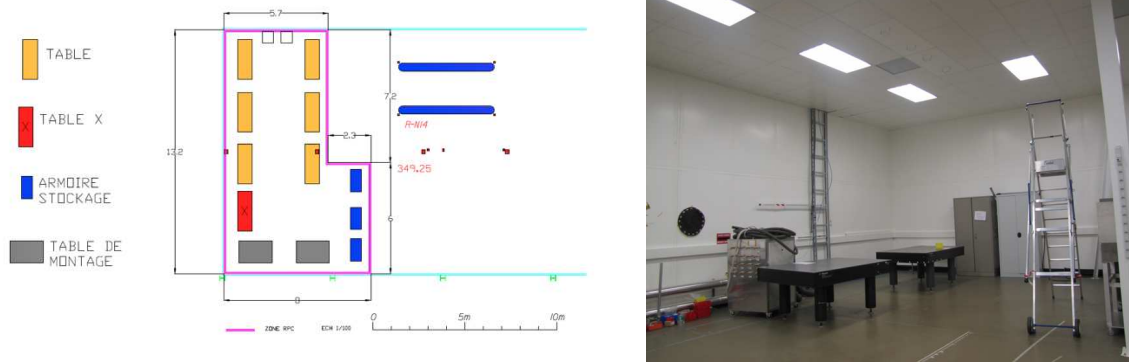


Figure 55: TIF clean room view.

We intend to host two main activities: production and testing. We have several tables and cupboards needed those purposes, for instance we have two optical tables large enough to fit the full size detector as shown in Fig. 55.

For future production and QC procedures in building 186 there are ten gas lines to be installed (Fig. 56) which will provide: Ar, CO₂, CF₄, N, Ar/CO₂ premixed and five additional spare lines. All the gas cylinders will be placed outside the building where there is the delivery gas point. To connect the external gas point to the lab ten stainless steel gas pipes of 10mm and an exhaust line of 22mm are foreseen. Inside the lab there will be the main gas distribution panel from which the gas supply will be provided to six small panels across the lab.

GEM foils will be handled in the TIF clean room to avoid any contact with dirty environment. The detector assembly will be performed following a new solution which is simple and cost-effective, imperative for a large-scale production. The *self-stretching* technique is described in Section 3.

The TIF assembly facility will host the GEM assembly and the quality control of each assembled detector.

Once detectors are assembled gain uniformity measurements will be performed to validate the chamber response using a cosmic stand facility, before the chambers will be transported to CMS for installation.

Similar facilities exist in some participating institutes and once approved, detailed plan and sharing of work for large scale production will be drawn out.

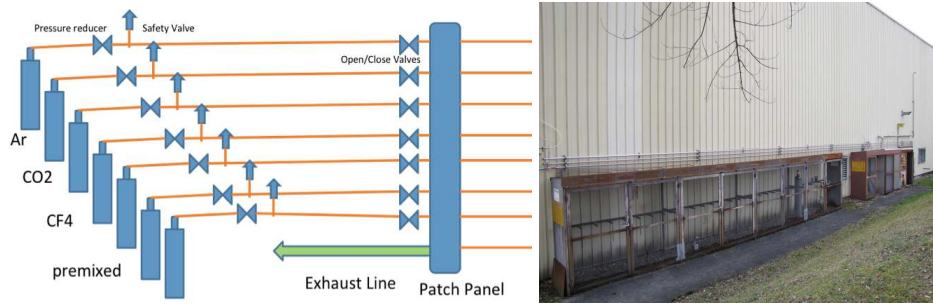


Figure 56: TIF gas system.

5.6 Production of GEM foils and assembly of GE1/1 detector

The CERN TE-MPE-EM fine pitch printed circuit board (PCB) workshop provides know-how and production facilities for the development of MPGDs. It is presently located in the building 102 and consists of an area of about 1000m² equipped with machines for rigid and flex PCB production. The infrastructure is well sized for prototyping and limited series productions. Large area gas detectors with GEM and Micromegas technologies became a real perspective for detectors upgrades as technology improvements allowed increasing in size and implementing more compact structures, with enhanced geometrical accuracy and cost reduction. This trend called for an improvement of the equipment infrastructure in the PCB workshop, in order to be able of processing larger PCB sizes. Together with the support of RD51, the workshop established a machine upgrade project. The project started in 2010 with the agreement of the CERN management to finance 785kCHF for the supply of ten key machines for large PCB size processing up to 1m in width. All machines orders have been completed in 2011 and the last batch of three machines will be received and installed in January 2012. As from next year the workshop will be capable to process GEM foils of sizes up to 2m×0.6m, where the limitation of 0.6m is imposed by the availability of the raw material. At the end of 2013 the whole TE-MPE-EM section will be moved to a new building facility (building 107), hosting together the design office, the fine pitch PCB workshop and the assembly workshop. The new working area will be located at the place of the building 174 and will also extend onto part of the present parking place. The new area will consist of 1400m², allowing a better installation for the working stations, providing better separation of equipment types into different dedicated rooms and improving the handling of larger PCB sizes.

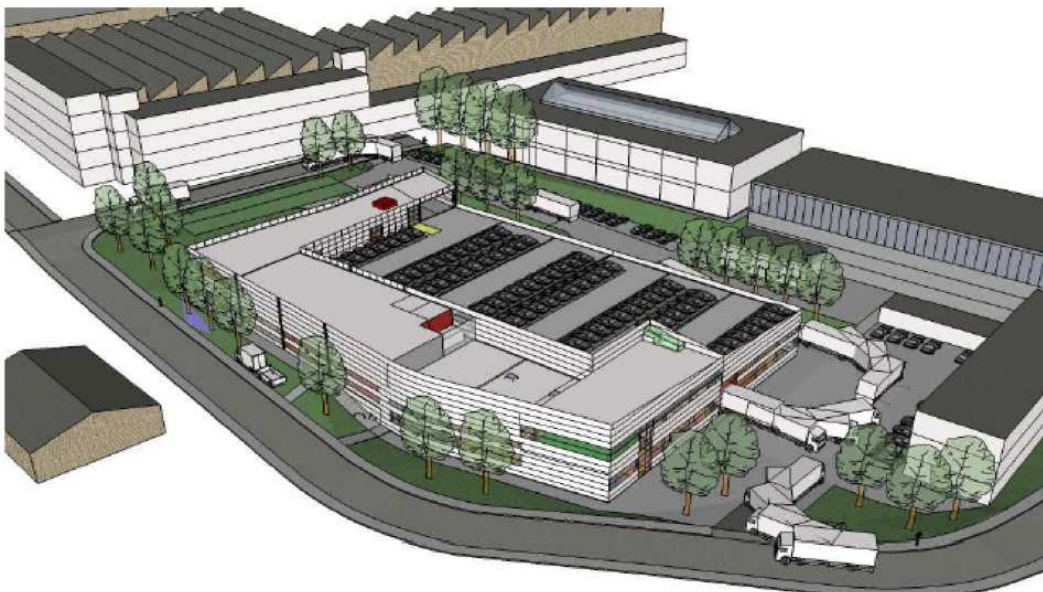


Figure 57: New building 107.

In the new building, in particular, it is planned to improve the service of detector development and qualification by providing two additional areas, one for the MPGD assembly (34m²) and equipped with test stations and another one with tool machines (35m²) for the manufacture of mechanical parts. The project for the development of GEM dedicated test station will start in January 2012 with the support of an AIDA fellow joining the MPGD team for two years. Limitation to the detector production volume in the workshop is mainly given by knowledgeable manpower.

Two actions have been taken in 2011. The first one consisted in securing team competence by opening two strategic LD positions in the MPGD domain (one technician for design and one technician for construction). The second one is to initiate a program of MPGD industrialization, within the framework of the RD51 WG6 (production) working group. A technology transfer program for GEM foil manufacturing has been established with NewFlex, a flex PCB Production Company located in South Korea. They were able to produce the first GEM foils of 6cm×6cm, which have been assembled in a detector and successfully qualified at CERN. NewFlex has recently performed a new production of 20 samples of 10cm×10cm GEM foils, which will be tested at CERN in January 2012 to qualify the production stability. If successful, the program foresees the manufacturing of larger size GEMs of 30cm×30cm and later in 2012 of a real CMS size. Regarding the CMS needs for GEM detector in the high- η region, the TEMPE-EM workshop plans to make available its know-how and facilities for the development and supply of the GEM detectors. The CMS planned quantities and deliveries are listed in the Table 4.

Table 4: Summary table which lists quantities and deliveries

Station	Num of modules	Module area	Total number of modules w/ spares	Total foil area (Triple-GEMs)	Manufacturing plan
1	$18 \times 2 \times 2 = 72$	$\approx 0.55\text{m}^2$ (1037x526)	80	132m^2	Yrs 2013+2014
2	$36 \times 2 \times 2 = 144$	$\approx 1.6\text{m}^2$ (1301x1251)	160	768m^2	Yrs 2015+1016

Station 1 could be produced at the CERN workshop at the production rate of about 12 GEM foils/month and 4 modules/month. The minimal needed manpower will consist of 2 field support units (FSU) people to be 100% devoted to the CMS Moun upgrade project, one for the GEM foil manufacturing and one for the detector assembly and test. One dedicated test stand has to be built. Additionally CMS shall make available a clean room of about 40m² for the assembly and test of the detectors. As the workshop is planned to move to the new building 107, it may be possible that additional clean room facility could be shared for this production batch during 2014. Station 2 needs the contribution of industry for the mass production of GEM foils. It should be planned a minimal production rate of 24 GEM foils/month and 8 modules/month. The workshop could take care for the detector assembly. Two FSUs have to be 100% devoted to the assembly and test procedures. The test stations need to be duplicated to sustain the production rate and to provide backup in case of repair of modules and in the event of test stand breakdown.

In addition, industrial contact has been established and technology transfer of fabrication of GEM foils to a firm “New Flex” in Korea has been completed. Twenty GEM foils produced in Korea have been delivered to CERN and are in the process of validation test in a detector. At the foil level, the quality controll was passed and full-scale foils are in the pipeline. Once the project is approved CMS baseline detector will be built by “New Flex”, Korea, setting up redundancy in the production.

Details about the installation sequences, integration within CMS and its services can be found in the Appendix B.

6 Electronics system

6.1 Introduction

This chapter discusses the electronics system currently foreseen for the control and readout of GEM detectors within CMS. At the most basic level the system can be divided into two main regions; the “on-detector” region and “off-detector” region, the latter being located in the counting room. All electronics located in the on-detector region have to be resistant to the radiation. This typically requires custom made electronics components whilst electronics located in the counting room can typically be designed using relatively inexpensive and available “off the shelf” components. Communication between the on-detector region and off-detector region will be done via optical fibres which also need to be resistant to radiation. Fig. 58 shows a block diagram of the main elements of the system.

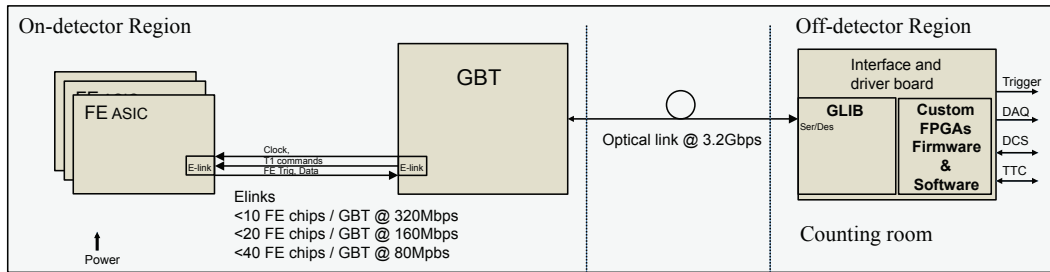


Figure 58: Block diagram showing the main components of an electronic control and readout system suitable for GEMs within CMS.

Many LHC High Luminosity systems variations are on this theme and hence common needs exist between sub-detector systems. Areas that are typically similar between LHC upgrades are power regulation and fibre optic transmission/reception. Generic developments, such as the GBT [28], Versatile Link [29], and DC/DC [30] projects are aimed to satisfy the “on-detector” common needs and the “GLIB” [31] project addresses common off-detector needs. The CMS GEMs electronic system intends to make full use of these generic projects as far as possible to minimize duplication of effort and ensure that design resources within the project are focused on the project specific designs needed. In addition the GEM detectors are evolving and the exact detector implementation within CMS is not yet fully defined. This means that any electronics system under design has to be flexible to changes in this respect over the coming years. The overall GEM electronics system is hence designed with the following philosophy:

1. **Take full advantage of current generic developments.**
2. **Flexibility in terms of system configuration and segmentation.**

In the follow sections the main components of both the on-detector and off-detector electronics will be discussed. The segmentation of the GEM system has many implications. These implications will be explained and show a possible segmentation option suitable for the CMS region GE1/1. In addition the road map for the evolution of the electronics systems from now until the final system will be shown.

6.2 On-detector electronics

In this section we will begin by looking at the GEM detector from an electrical perspective before going on to examine the requirements and design specifications for the front-end ASIC.

6.2.1 The GEM chamber (from an electrical perspective)

A number of large Triple-GEM prototypes have been built and tested by the collaboration. One such example is shown in Fig. 59. This prototype has been split into 4 η regions, each one divided into 256 strips. The chamber is designed to cover and arc with increasing area per eta region as we radiate out from eta region 1 to region 4.

The GEM electrical model is of vital importance to the readout electronics. Fig. 60 shows the schematic diagram of the detector showing the biasing of the 3 GEM foils and the parasitic capacitances between them. The readout strips are shown at bottom of the induction gap below GEM 3, these are directly bonded to the input channels of

Interstrip capacity

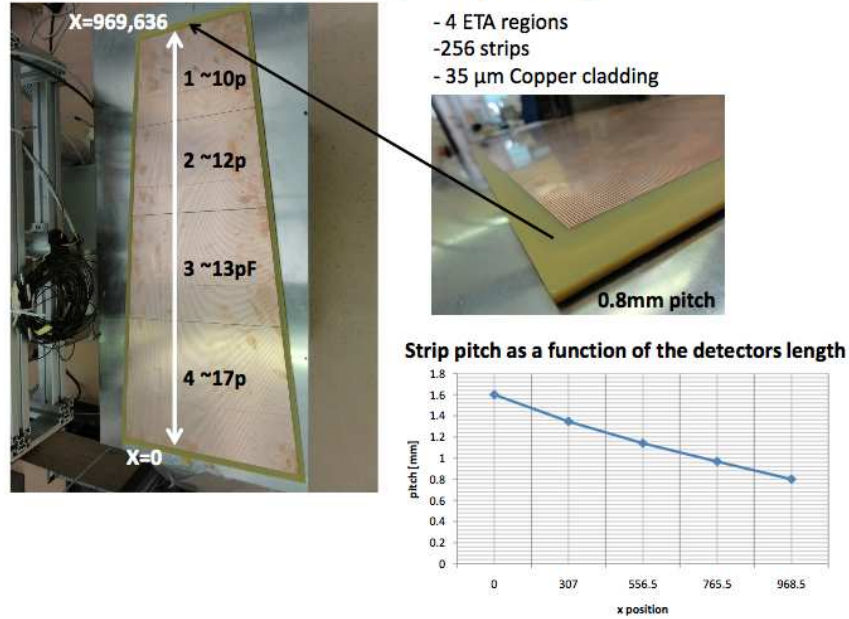


Figure 59: Strip dimensions for GEM prototype GE1/1.

Capacity measurements of GE1/1

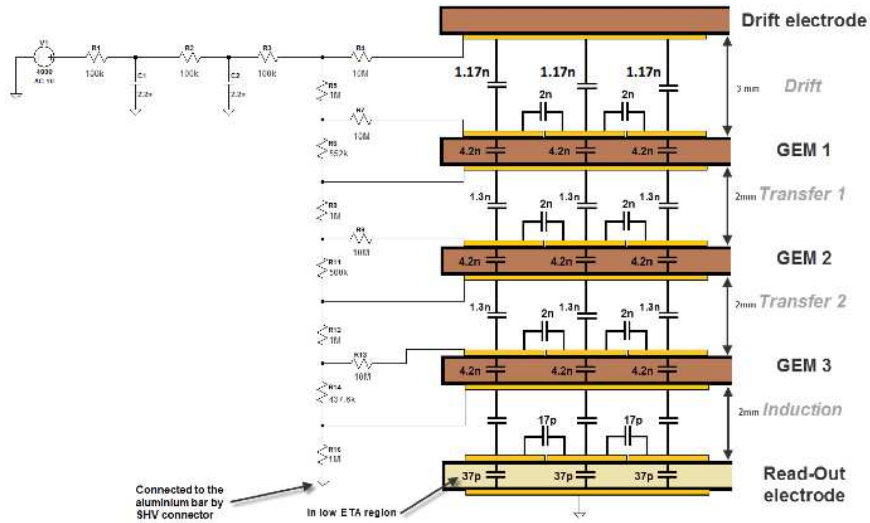


Figure 60: The electrical characteristics of GEM prototype GE1/1.

the readout ASIC. The front-end ASIC used to readout this chamber was the VFAT2 chip (capable of reading 128 channels per chip) requiring 8 chips to readout all channels. The interstrip capacitance was measured at 37pF and the strip to ground plane at 11.7pF giving a total capacitive load of approximately 59pF for each channel.

6.2.2 The front-end ASIC development - VFAT2 to VFAT3 and GdSP

The functional requirements on the system (and indeed the front-end ASIC) are to provide both triggering and tracking information. These are similar basic requirements to that needed for the TOTEM [32] experiment currently using the VFAT2 [33] chip to readout both silicon and gas detectors. The VFAT2 chip is hence the front-end readout chip of choice for initial prototype systems using the large GEM detectors. The need to operate at very high particle

rates and the need for compatibility with the GBT mean that a new ASIC will be required for the future. In the following we provide an overview of the VFAT2 chip before leading on to the design requirements for a new front-end chip (VFAT3/GdSP).

VFAT2 The VFAT2 chip (Fig. 61) is a trigger and tracking front-end ASIC, initially designed for the readout of silicon and gas sensors of the TOTEM experiment. It has two main functions; the first (Trigger) is to provide programmable “fast OR” information based on the region of the sensor hit. This can be used for the creation of a trigger. The second function (Tracking) is for providing precise spatial hit information for a given triggered event. The possibility of these two functions plus internal input protection for use with GEMs make VFAT2 the ideal (existing) candidate for the readout of the current GEM prototypes.

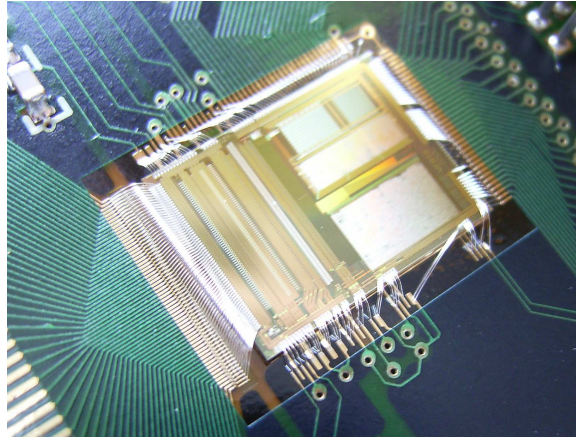


Figure 61: VFAT2, A 128 channel front-end ASIC with trigger and tracking capabilities. This ASIC is currently used for the prototype systems.

Fig. 62 shows the block diagram for VFAT2.

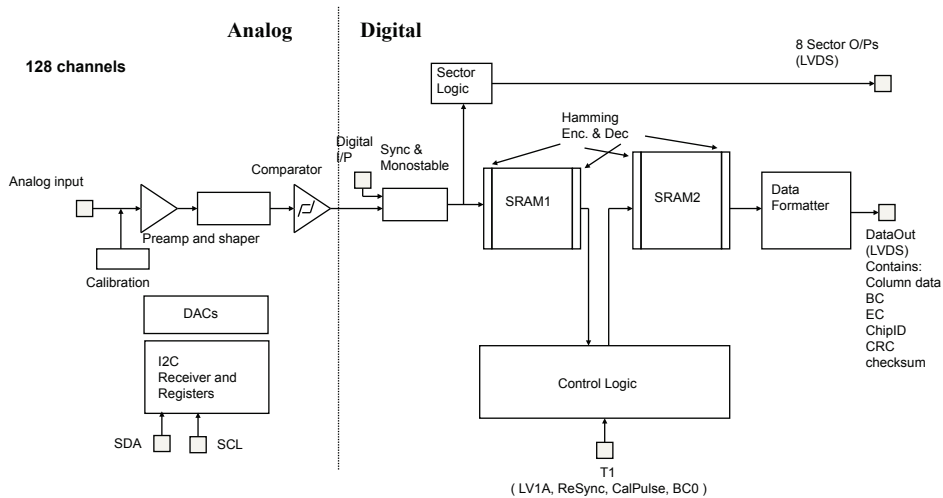


Figure 62: The VFAT2 architecture, shown for 1 channel.

It has 128 analog input channels each of which are equipped with a very low noise pre-amplifier and shaping stage plus comparator. A calibration unit allows delivery of controlled test pulses to any channel for calibration purposes. Signal discrimination on a programmable threshold provides binary “hit” information which passes through a synchronisation unit and then stored within SRAMs until a trigger is received. The storage capacity enables trigger latencies of up to $6.4 \mu\text{s}$ and the simultaneous storage of data for up to 128 triggered events. Dead time free operation with up to 100kHz Poisson distributed trigger rates is ensured. Time and event tags are added to the triggered data which are then formatted and read from the chip in the form of digitized data packets at 40 Mbps. The programmability is achieved through an I²C interface whilst the fast ports are LVDS.

VFAT3 The VFAT architecture is the baseline front-end ASIC architecture for the CMS GEM system. However, the requirements for the system, whilst very similar to those of TOTEM, differ in some very important ways that make the design and optimization of a new front-end ASIC a necessity. The main differences are listed below:

1. Operation at high particle rate using large GEM detectors
2. Precise and clean trigger information at very high rate ($\approx 2.3\text{MHz}/\text{chip}$)
3. Large detector capacitance 20 - 60pF
4. Relatively long signal charge collection $\approx 80\text{ns}$
5. Interface required : slvds elinks to GBT (as opposed to I²C and LVDS)
6. Integrated calibration, bias and monitoring functions,

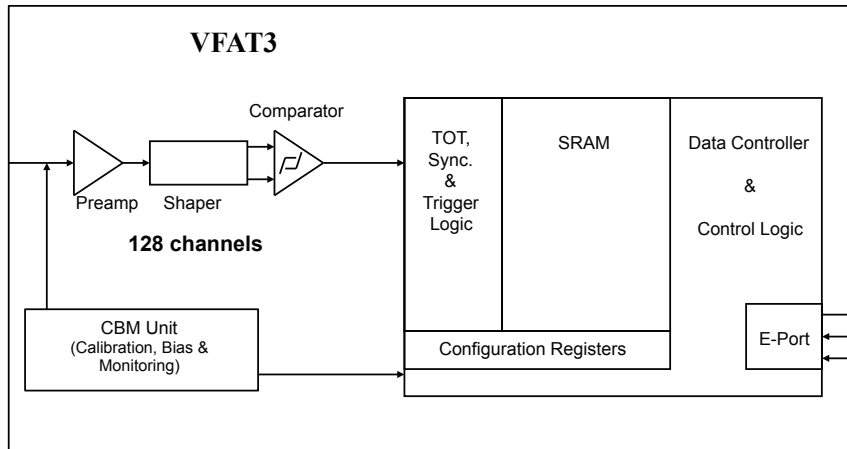


Figure 63: VFAT3 architecture.

The block diagram for VFAT3 is shown in Fig. 63. Similarly to VFAT2 it will have 128 channels of preamplifier, shaper and comparator. The shaping time and gain will be programmable in order to optimize the signal charge collection from the GEM detector whilst maintaining excellent timing resolution ($\approx 4.5\text{ns rms}$ for VFAT2). A longer shaping time will result in improved signal to noise ratio when used with GEM detectors due to reduced ballistic deficit. This in turn will reduce sensitivity to baseline pedestal jumps which can otherwise contribute to the noise. However increased shaping times come at the cost of degrading time-resolution due to increased time-walk. To avoid this degradation of time resolution we are studying the implementation of digital “Time Over Threshold” (TOT) techniques to compensate for time walk and restore the original time resolution. The binary “hit” data and associated time tag are then buffered in SRAM memory before being readout in data packets at 320Mbps via the e-port. Slow control functions also communicate via the e-link to the outside world. The CMB unit provides internal circuitry for the slow control functions of calibration, biasing and monitoring. This avoids the need for an additional slow control ASIC.

GdSP The GdSP architecture is very similar to that previously described for VFAT3 with the same resulting data packet content. However instead of using a comparator plus TOT, the GdSP incorporates an ADC to digitise samples from the preamplifier and shaper. Until recently it would have been unthinkable to have an ADC per channel due to the ADC power demands. However, very rapid advance of ADC design techniques in recent years now make it possible to design ADCs with an order of magnitude less power than 2-3 years ago. It is hence now possible to have an ADC per channel on a 128 channel chip with ADC power consumption $< 4\text{mW} / \text{channel}$. Once samples have been digitized by the ADC, digital signal processing and filtering can be employed to reduce common mode effects and background artifacts. This in turn enables very clean signal discrimination for the creation of a trigger.

The block diagram for the GdSP chip is shown in Fig. 64. Note that VFAT3 and GdSP share most of the important building blocks, differing only with respect to comparator + TOT versus ADC+DSP.

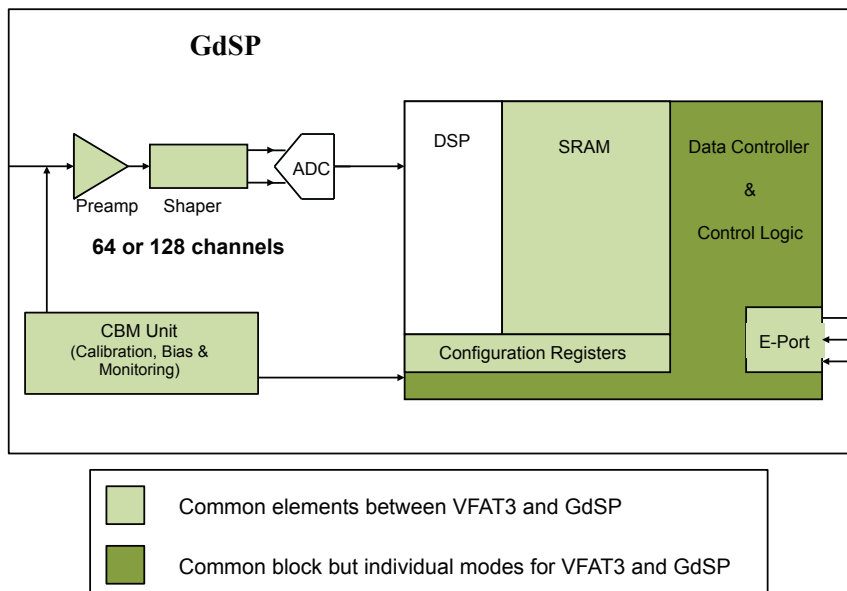


Figure 64: Gdsp architecture.

6.3 Off-detector electronics

The off-detector Electronics provides the interfaces from the detector (and front-end electronics) to the CMS DAQ, TTC and Trigger systems. The design foreseen for the “GEM off-detector Electronics” is based on FPGAs and Multi-GBit/s links that adhere to the micro-TCA (μ TCA) standard[39]. This is a recent standard that has been introduced for the Telecom industry and aims at high data throughput (2 Tbit/s) and high availability (with very low probability of interruption at $\approx 10^{-5}$). It is compact, hot swappable and has a high speed serial backplane. This standard helps ensure compatibility with other CMS sub-detector developments as is used by the GLIB common project and other CMS subdetector upgrade developments such as the calorimeter trigger upgrades [8].

The off-detector Electronics will be designed with a high level of flexibility. This is assisted by design based on Advanced Mezzanine Cards (AMC) used together with the μ TCA standard. Compatibility is also extremely important in that it must be able to integrate GEM data to the current RPC PAC trigger system as well as being able to perform local trigger functions as required. Flexibility and compatibility is therefore key to the design of the system.

The existing RPC PAC trigger system is one of the three muon trigger subsystems of the CMS experiment. Its detailed description can be found in [1], [34] and [35]. It is, in itself, expandable however the integration of the GEM system with the RPC PAC trigger requires an additional interface due to GEMs higher granularity and higher optical link bandwidth.

To date we have considered 3 possibilities that need to be considered in the trigger integration of data from the high- η GEM detectors. The three options include interfacing to the current RPC PAC trigger boards, integrating the trigger boards into the μ TCA crate and allowing for a possible future update of the entire RPC trigger system. These 3 possibilities are explained below, they assume that GEM detectors are used in the high- η part of the first and second endcap muons stations (GE1/1 and GE2/1), while in the third and fourth endcap muon stations have RPC chambers.

Option A: interfacing GEMs to the existing RPC PAC Trigger Boards In this option, shown in Fig. 66, the trigger algorithm is performed by Trigger Boards (TB), in exactly the same way as the current RPC PAC TB. Vacant slots in the current RPC Trigger Crates (TC) could be used for this purpose. The data from the GEM detectors are transmitted (via previously described GBT optical links) from the Underground eXperimental Cavern (UXC) to the GLIB boards and dedicated μ TCA crate located in the Underground Service Cavern (USC). In that crate the trigger bits corresponding to the GEM strip signals would be ORed (both in η and ϕ) to the granularity required by the PAC algorithm. The data would then be converted to the format used in the RPC link system (zero-suppression multiplexer) and transmitted via 1.6 Gbps optical links. The optical signal would have a similar format to the signal produced by the Gigabit Optical Link (GOL)[36] serializer, currently used on the Link Boards of the current RPC trigger system, so that the fibers can be connected to the current TBs. The preprocessing and conversion of the

GEM data would be performed on a custom mezzanine placed on the GLIB board.

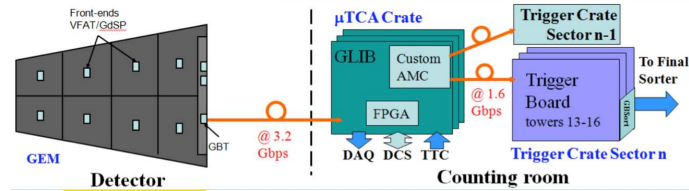


Figure 65: Off-detector Electronics option using the current RPC PAC trigger.

The number of optical links would depend on the GEM segmentation. However, it is important to note that the standard TB has got 18 inputs for the optical links and covers an arc of 30°. Eight of these optical link inputs are used to receive data from the RPC chambers in the RE3/1, RE3/2, R4/1 and RE4/2 regions[37]. The structure of these optical links is an integral part of the RPC system; the GEM interface would need to adhere to this structure to ensure compatibility. Thus 10 optical link inputs are available in each TB for receiving data from GEMs in GE1/1 and GE2/1.

The custom AMC board would encode the data to be compatible with the existing RPC PAC trigger. This uses effectively 21 bit/BX in one optical link. The data coding algorithm, used in the PAC trigger system[38], divides channels into partitions and transmits channels hit within partitions plus a time stamp with the following code bit allocation:

1. 8 bits of the partition data,
2. 9 bits of partition number,
3. 3 bits of partition delay,
4. 1 bit end-of-data

One further requirement for compatibility with the current RPC system is that the maximum latency of the GEM data at the input of the TB cannot exceed the current latency of the RPC data. The maximum latency would therefore be 42 BX, this includes: muons time of flight, detector and front-end electronics signal processing, optical transmission from the UXC to the USC, processing in the GLIB and transmission from GLIBs to the TBs.

Option B: Design of integrated GEM Trigger Boards (GemTB) in the μ TCA crate In this option, shown in Fig. 65, the trigger algorithm is performed on a new GEM Trigger Board (GemTB) placed in the μ TCA crate together with the GLIB boards. The GEM data from the GLIBs are transmitted to the GemTBs through the crate backplane. The advantage of this system is that full granularity data can be transmitted providing the trigger algorithm can profit from it. It is likely that multiple μ TCA crates would be needed to cover the full phi-range of one detector side. Therefore the possibility of data exchange between adjacent crates would be provided in order to assure the logical overlapping of sectors. Additionally, the GemTBs would receive data from the RPC chambers RE3/1, RE3/2, R4/1. and RE4/2 via the current RPC optical links. The muon candidates found by each GemTB would be collected by a GBSort board in which local ghost-busting and sorting of trigger candidates is performed. Muon candidates would then be transmitted to the Trigger Crate (TC) and introduced into the TC GBSort chip for additional ghost-busting and sorting. Interface Boards placed in the slots originally foreseen for the high- η TBs could be used for this purpose.

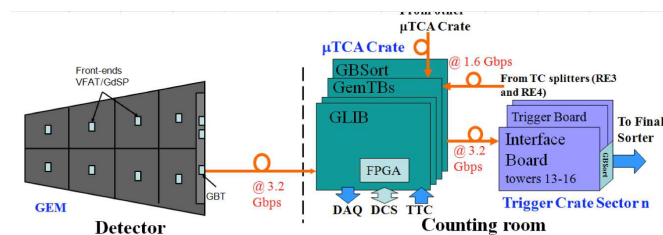


Figure 66: Off-detector Electronics option using new AMC GEM Trigger Boards (GemTB).

The detector region covered by one GemTB in principle does not have to correspond to the PAC logical sector, but can be smaller. The choice would be driven mainly by the granularity of the data used in the GemTB trigger

algorithm, the GemTBs input data bandwidth and the number and size of FPGAs used for executing the trigger algorithm. If the GEM chambers are doubled (to form superchambers) in the first and second station, then the trigger algorithm can use a delta phi between the hits in the doubled layers of the same station to improve the muon momentum measurement. For that, the full granularity of the GEMs would be needed. This cannot be performed by the current RPC TBs, as in option A, because it would not be possible to transmit full granularity GEM data to the current TBs. Therefore option B (or C) would be the preferred choice in the case of superchambers.

The maximum latency of the high- η muon candidates at the input of the Trigger Crate GBSort chip cannot exceed ≈ 70 BX.

Option C: Updating the entire RPC PAC Trigger System Recently, discussions within the CMS Collaboration have started about possibly updating the entire trigger electronics around the year 2020. While a discussion on the new PAC Trigger system is premature and out of the scope of this document, the GEM off-detector Electronics system must also provide for the possibility of a new RPC link system also built using the GBT-GLIB concept with the trigger algorithm performed in new electronics hosted in a μ TCA crate. This system would hence be very similar to the one for the high- η GEMs in the option B, except that the muons candidates from the entire system would be ghost busted and sorted in a new Final Sorter μ TCA crate.

6.4 System considerations

6.4.1 General system view

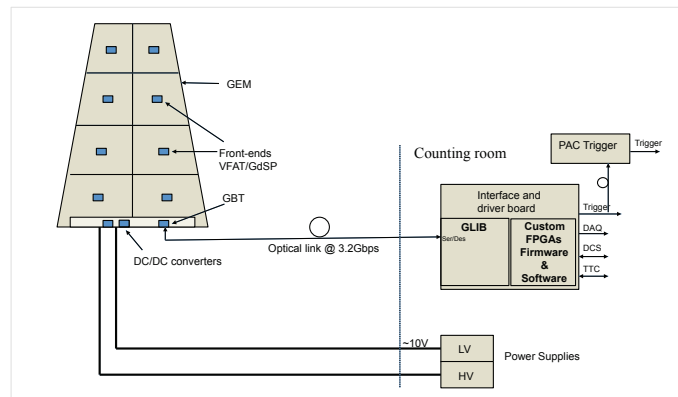


Figure 67: Block diagram for the electronics system (control and readout) as foreseen for the CMS forward high- η region.

Fig. 67 shows the block diagram for the system. A brief summary of the system is as follows:

1. One GEM chamber is segmented into different eta regions and columns creating GEM segments.
2. Each GEM segment is subdivided into 128 strips or channels.
3. One front-end ASIC (VFAT3/GdSP) is used per GEM segment to readout the charge deposited in each GEM channel.
4. Power is delivered to the GEM chamber by electrical cables. Local DC/DC regulators condition the voltage to the levels required by the on-detector electronics.
5. E-links (electrical SLVDS pairs) connect the front-end ASICs to the GBT chipset.
6. The GBT chipset multiplexes to and from the front-end ASIC and receives/transmits data between the inner and outer detector regions via optical fibres.
7. The off-detector electronics within the counting room has an interface and driver unit providing the interface to the CMS trigger, DAQ, DCS and TTC systems as well as allowing integration to the existing PAC trigger.

This basic system is highly flexible to different GEM geometries and segmentation configurations. For the GE1/1 region of CMS, each GEM chamber will cover an arc of approximately 10 degrees, therefore there will be 36 chambers in a ring. In the case of a double layer using super chambers there will be 72 GEM chambers per ring.

6.4.2 Segmentation

The GEM chamber is sub divided into columns and eta partitions as shown in Fig. 68.

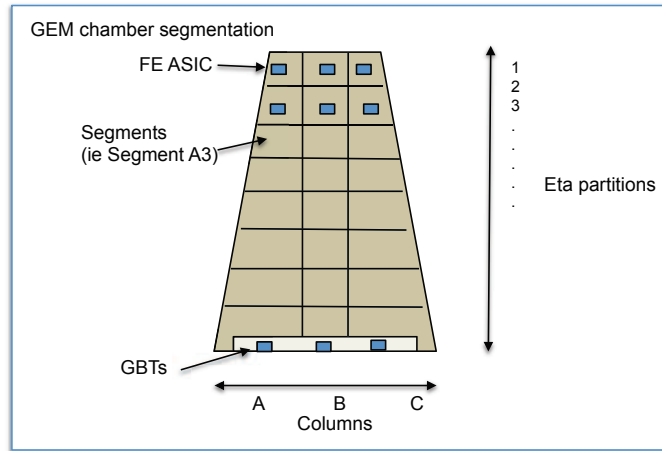


Figure 68: The GEM segmentation into columns and eta partitions.

The segmentation of the GEM chamber has many implications, the main ones are noise, rate capability, power and cost. One can summarise the general effects as in Table 5

Table 5: Summary table

	Increasing Eta Partitions	Increasing columns
Area cover by one chip	↘	↘
Strip area and capacitance	↘	↘
Noise	↘	↘
Strip pitch	-	↘
Rate capability	↗	? ↘
Power	↗	↗
Cooling needs	↗	↗
Cost	↗	↗

The optimal balance between all of these factors is a delicate study which is not yet completed. For GE1/1 we have so far considered columns-eta partitions of 3-4, 3-8 and 3-16 creating 12, 24 and 48 sectors respectively. A fourth possibility of 3-10 is also under consideration as this provides the optimum usage of bandwidth of the GBT. This is because (at the maximum GBT E-Link frequency of 320Mbps) the GBT can communicate with up to 10 front-end chips. Hence a 3-10 configuration requires one GBT and one optical fibre per column with 10 front-end ASICs per column. Initial studies of rate capability show that operation with a 3-10 configuration with a hit rate of $< 10\text{kHz}/\text{cm}^2$ is possible.

6.4.3 Electronics power consumption for a 3-10 chamber.

The chamber is designed as an individual element in order to allow for flexibility in terms of number of chambers and number of layers in a system. Here the power and cost is calculated for a single 3-10 single chamber. A double layer super-chamber is also double the power of a single chamber. Table 6 shows the estimated power consumption of the principle electronic components used. These numbers can be considered an upper limit.

6.5 Project planning

Time planning The design of the front-end ASIC can be broken down into 4 phases as detailed in Table 7. Phase 1 covers the specification phase. This phase began in 2011 and is expected to be complete by the second quarter of 2012. Phase 2 is the design of the individual electronic modules while phase 3 is the integration of these modules into a complete chip. Following fabrication phase 4 covers the prototype testing phase. Table 7 gives the estimated man months for the different elements and phases totaling an estimated 8 man years for the project. These numbers

Table 6: Power estimate for the main components of a single chamber with 3·10 segmentation.

Element	Number of units	Voltage (V)	Power per chamber (W)	Power per chamber (W)	Power per chamber (W)
GdSP	30	1.5	GdSP<1	GdSP<10 (6.7A at 1.5V)	GdSP<30W
VFAT	30	1.5	VFAT<0.6	VFAT<0.6 (4A at 1.5V)	VFAT<18W
GBTx	3	1.5			4.242W at 1.5V
GBTIA	3	2.5			2.25W at 2.5V
GBLD	3	2.5			
DC/DC regulators	7 (2 per column + 1 for the GBT 2.5V)	In: 12 Out: 1.5/2.5			
LDOs (on or off chip)					
Total					GdSP<51W (12V, 4.25A) VFAT<34 W (12V, 2.8A)

are consistent with previous experience of the VFAT2 and PACE[39] chip designs.

Table 7: Silicon fabrication cost estimated for different elements and phases.

	Main Tasks	Estimated man month
Phase 1 “Specification”	Technology Choice	2
	DSP functionality & simulation	6
	Identify IP components, vendors & collaborators	1
	Specification (memory sizes, data packet structure etc)	3
	Specification document	4
	System high level simulation	6
Phase 2 “Module design”	Preamp + shaper	6
	Comparator + Sync	4
	ADC	2
	DSP	6
	CBM unit	4
	SRAMs	4
	Digital control	6
	GBT interface	4
	Verilog AMS modelling	6
Phase 3 “Full chip design”	Buy IP blocks if needed & simulate, DRC check	2
	Assembly of full chip	6
	Checking (DRC/LVS) of full chip	4
	Verilog and verilog AMS simulation of full chip MPW	6
hline Phase 4 “Testing”	MPW 1 testing	12
	Sub total	95 8 man years
Phase 5 “Production”	Engineering run submission	9

The Readout System development will continue throughout the design period of the front-end ASIC . The goal of the prototype readout systems is to both provide readout electronics for GEM prototype studies and to develop the final readout system. We can break this down into 3 periods of time; Present, Medium Term and Final. These are visualized together with the FE ASIC design as a timeline in Fig. 69.

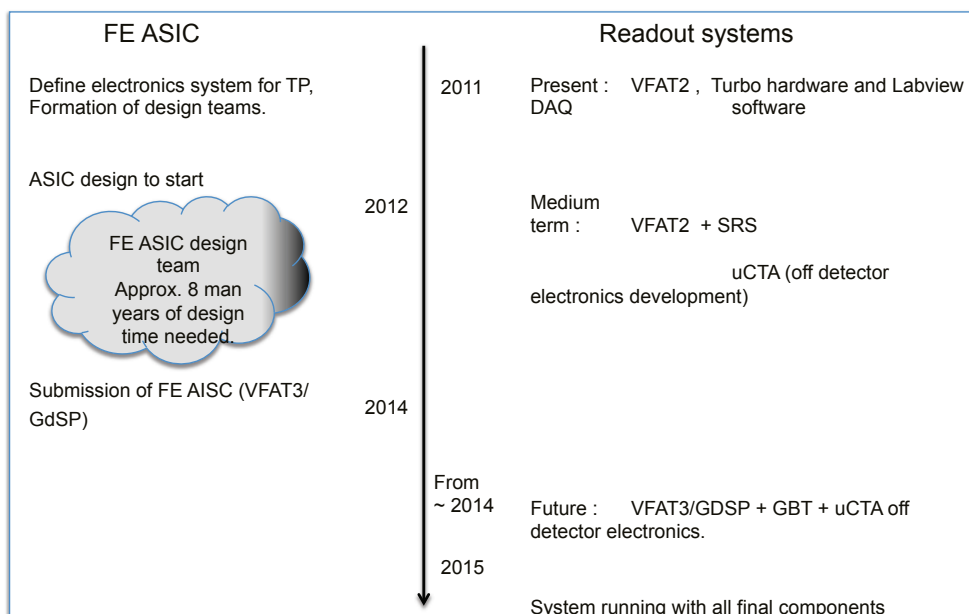


Figure 69: Time line for the front-end ASIC development and readout systems.

The Present readout system is based on the VFAT2 chip working together with the Turbo readout board. This system has been in use throughout 2011 and expected to continue into 2012. The SRS [15] readout system has been commonly used for small prototype systems for GEM detector development. An SRS system compatible with VFAT2 is foreseen for the medium term to enable collaborators easy access to electronics for GEM detector development. In addition the development of the final off-detector system will take place during this medium term period occupying 2012 and 2013. The time scale is such that the FE ASIC, GBT chipset and off-detector uCTA readout system should be ready for the assembly of the final system by 2015. The production of components should be started from 2015.

A one year production period is reasonable while a two year assembly period should be anticipated.

6.6 Cost:

6.6.1 On-detector costs

FE ASIC silicon costs: The technology currently foreseen for the fabrication of the front-end ASIC is a CMOS 130nm process. The reason for this choice was largely related to the existence of device libraries and many useful building blocks and cost. The cost of fabricating a design in 130nm is approximately half that of fabricating in a more advanced 65nm process. ASIC designs can be submitted to the foundry either as an (Multi Project Wafer) MPW run or as a dedicated engineering run. MPW runs shared the silicon mask cost with other projects and hence have reduced cost. This is ideal for prototyping small circuits and modules. The engineering run is for production. In an engineering run one project is submitted yielding many more chips. Table 8 summarises the current cost of an MPW run and an engineering run in this process.

Table 8: Silicon fabrication cost of an MPW run and an engineering run in this process.

Run Type	Cost	Number of chips	Use
MPW Run	\$ 3.25k/mm ² , (\approx 50k)	40	Prototyping
Engineering Run	\$ 400 + \$3k/wafer (min quantity = 24 wafers) therefore \$522k	6480 (assuming a slightly larger area compared to VFAT2)	Production

In order to make an estimate of the price per front-end chip from an engineering run we have to make a few assumptions on number of chips per wafer, yield, dicing and packaging cost. Hence assuming 300 chips per wafer, 90% yield, packaging cost at \$ 20k + \$ 2/piece the total price per chip is \$ 78 with a minimum investment of \$ 506.4k .

Cost for components for 3-10 chamber (single and super): The estimated cost of the main electronics elements for a single chamber is shown in Table 9.

Table 9: Estimated costs of the electronics components for a single chamber

Element	No. of elements	Cost/element (\$)	Cost/element (CHF)	Cost per GEM Single Chamber (CHF)
GdSP/VFAT3	30	78	69	2070
DC/DC reg.	7	80	90	632
GBT	3	88.6	100	300
Optical Link	3	265.8	300	900
Cables	2	886	1000	2000
Total				5902

All the estimates are very preliminary and subject to change as their individual developments projects advance. Having made the cost estimate for a single GEM chamber. It is now straight forward to calculate the estimated cost for a Super Chamber and then for a system. A Super chamber is essentially a double sided single chamber and simply has double the components except for the cables. Hence the table for a super chamber is as in Table 10

Table 10: Estimated costs of the electronics components for a super chamber.

Element	No. of elements	Cost/element (\$)	Cost/element (CHF)	Cost per GEM Super Chamber (CHF)
GdSP/VFAT3	60	78	69	4140
DC/DC reg.	14	80	90	1264
GBT	6	88.6	100	600
Optical Link	6	265.8	300	1800
Cables	2	886	1000	2000
Total				9804

6.6.2 Off-detector: components for a μ TCA crate

For the off-detector electronics, we plan to use standard μ TCA crates which can host up to 12 double width AMCs, such as the GLIB. The GLIB board, equipped with a mezzanine, can receive data from up to 8 optical links. Table 11 shows the cost estimate of the different components that will be used for the off-detector electronics. All the estimates are very preliminary and subject to change as their individual developments projects advance.

Table 11: Cost of the off-detector components

Component	Cost (CHF)
GLIB/AMC	2500
μ TCA crate	6200

Assuming the architecture B for the off-detector Electronics, a possible arrangement would be that one μ TCA crate receive the data from a 10° sector of GE1/1 and GE2/1. After data compression the data coming from three μ TCA crates corresponding to 3 subsequent 10° sectors would be transmitted through a fast link to a fourth μ TCA crate that would receive the data from a 30° sector of RE3/1, RE3/2, RE4/1 and RE4/2. On this crate the data from a high- η 30° sector would then be processed by a GemTB and local ghost-busting as well as the sorting of trigger candidates could be performed. Table 13 shows the cost estimate for a 30° sector equipped with single GEM chambers.

For super chambers, one additional GLIB board per crate would be needed to handle the additional optical links. Table 13 shows the cost estimate for a 30° sector equipped with super chambers.

Table 12: Estimated costs of the off-detector electronics components for a 30° sector equipped with single GEM chambers.

Element	No. of elements	Cost per 30° sector Single Chamber (CHF)
GLIB/AMC	12	30000
μ TCA crate	4	24800
Optical Link between crates	5	360
Total		55160

Table 13: Estimated costs of the off-detector electronics components for a 30° sector equipped super chambers.

Element	No. of elements	Cost per 30° sector Single Chamber (CHF)
GLIB/AMC	15	37500
μ TCA crate	4	24800
Optical Link between crates	5	360
Total		62660

6.6.3 GE1/1 system cost estimate (on and off-detector)

The GE1/1 system is comprised of an 36 super chambers in one ring per endcap. For the two end caps there will be two rings hence a total of 72 super chambers for the on-detector part. Table 14 shows the estimated cost of the GE1/1 system in both endcaps. The cost of the power supplies is also included assuming one super chamber is fed with separate channels of low and high voltage for each side of the super chamber.

Table 14: Estimated costs of the electronics components for a super chamber.

Element	No. of elements 72 super chambers (36 in each endcap) (CHF)	GE1/1
GdSP/VFAT3	4320	298080
DC/DC reg.	1008	91008
GBT	432	43200
Optical Link	432	31104
Cables	144	144000
Power supplies	144 HV & LV ch.	405162
On-detector total		1082538

At the time of writing the GE2/1 system segmentation is still to be defined so the on-detector electronics cost for GE2/1 cannot be done at present. The off-detector electronics however combines data from GE1/1 and GE2/1 together. For this reason provision has been made for including data from GE2/1 in the off-detector electronics design cost estimate. Table 15 shows the cost estimate of the off detector electronics components assuming 72 super chambers for the GE1/1 and making provision for links form GE2/1.

Table 15: Estimated costs of the electronics components for a super chamber.

Element	No. of elements 72 super chambers (36 in each endcap) (CHF)	GE1/1
GLIB/AMC	360	900000
μ TCA crate	96	595200
Optical Link between crates	120	8640
Off-detector total		1503840

7 Cooling, gas and cabling services

7.1 Gas

The GEM detector system for the CMS experiment has a total volume of about 3.4m^3 . The chambers are operated with a three component gas mixture made of $\text{Ar}/\text{CO}_2/\text{CF}_4$ (45:15:40). The basic function of the gas system is to mix the three components in the appropriate proportions and to distribute the gas mixture into the individual chambers. The expected flow regime is 5 volume changes per day equivalent to about 700 nl/h. The gas system for the GEM detector will re-use part of the infrastructure as they were foreseen for the innermost RPC end-cap station, in particularly the distribution racks located in the experimental cavern. The detector volume, the required gas flow and the use of a relatively expensive gas mixture make a closed-loop circulation system highly favorable. The system proposed consists of several modules, which are designed using the standard adopted in all the gas system for the LHC experiments. The gas system will be running on PLC and it will be controlled/monitored using the standard PVSS⁴⁾ interface.

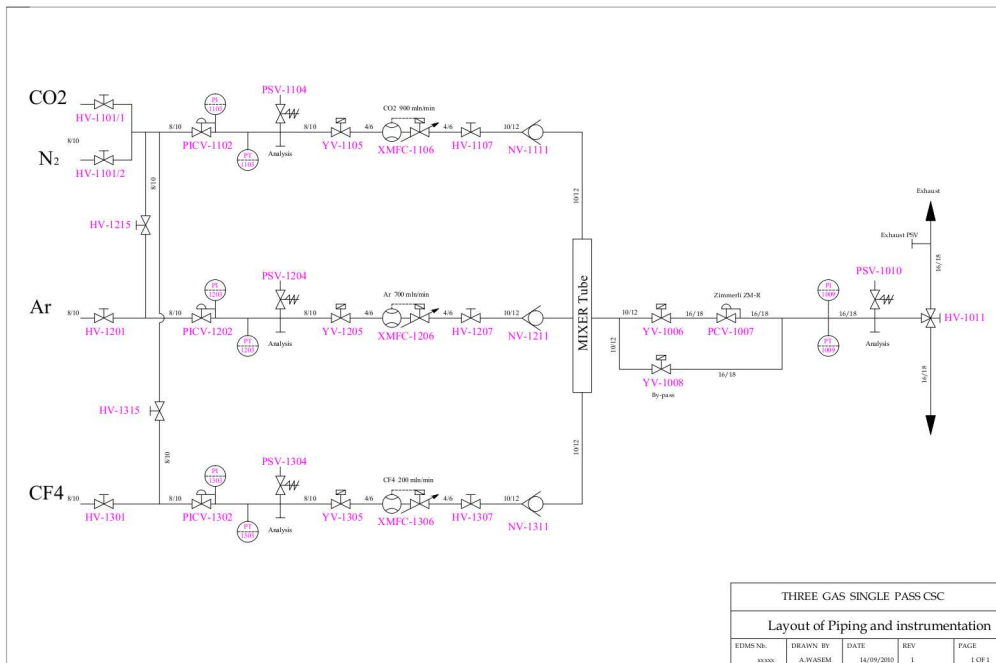


Figure 70: Layout of the mixer unit.

Primary supply The gas system will be connected to the existing primary supply network for Ar , CO_2 , CF_4 and N_2 (the latter it is mainly used to control pneumatic valves located inside the experimental cavern).

Mixer The mixer unit will be located in the SGX5 building. The flows of each gas component will be metered by mass flow controllers (MFC). The mixing ratio will be adjusted and monitored by the software control running on the PLC. The mixer unit will contain two sets of MFCs: the first called run will be used for normal operation, while for a fast filling of the detector a second set (fill) with higher flow capacity will be employed. Fig. ?? shows the drawing of a typical mixer unit, while an approximate price quotation is given in Table 16.

Closed-loop circulation In order to reduce the operational cost, the gas is circulated in a closed loop circuit. The circulation loop is distributor over three different areas:

1. Purifier (optional), gas input and exhausted gas connections are situated in the SGX building;

⁴⁾ Process visualization and control system

2. Pressure controllers, pre-distribution system (i.e. between negative and positive endcap) and pump compressor (Fig. 71) are located in the UGC and therefore accessible anytime;
3. The manifolds for the final gas distribution and the flow meters are mounted in the distribution racks on the detector.

The GEM gas system will re-use the pressure controllers, the pre-distribution system and the final distribution racks already available since they were installed as a part of the RPC gas system. The amount of work needed to adapt the present installation to the new system needs to be evaluated, but it is certainly a clear economical advantage. The available distribution rack (Fig. 72) has 13 channels that can be used by the GEM detector. Each channel is equipped with input and output flow-meter and a basic flow regulation system. Table 16 gives an overview of the modules needed for a closed-loop gas system for the GEM detector. An approximate cost estimate for each module is also given. The extra-cost due to the new modules needed for a closed-loop gas system with respect to an open-mode gas system is about 70 kCHF and it will be easily recuperated during the first 6 months of operation. At the present stage, the Purifier module remains as an option. Dedicated test during R&D and detector construction phase will indicate if an extra module for O₂ and H₂O removal is really needed.

CF₄ recuperation The CMS experiment will be soon equipped with a CF₄ recuperation system. The advantage of such a system is to allow controlling the N₂ concentration in the detector since it is basically impossible to filter N₂ from the gas stream. Future test will be carried out in order to understand if the GEM gas system will benefit from this plant that presently is under commissioning and, at the moment, it foreseen to be used only by the CMS-CSC.

Conclusion The CMS-GEM detector will be equipped with a closed loop gas system as the extra-cost needed for this solution will be easily recuperated during the first sixth months of operation. Table 16 gives an overview of the price quotation for each module (material and manpower). The GEM gas system will also need two new stainless-steel pipes from the SGX5 building to the UGC room. The cost for this item is not included in the present evaluation. Also the piping on the disk needs to be verified if present and/or reusable.

Table 16: Summary of the new and existing modules needed for the CMS-GEM gas system.

Module	Location	Status	Approximate price quotation (kCHF)
Primary supply	SGX5	existing module	-
Mixer	SGX5	New module	30
Chamber pre-distribution system	UGC55	existing module	Minor modifications
Chamber distribution system	UXC55	existing module	Minor modifications
Pump	UGC55	New module	25
Purifier (optional)	SGX5	New module	35
Exhaust	SGX5	New module	10
Connection to existing	SGX5	existing module	To be evaluated
CF ₄ recuperation plant			

7.2 Cooling

This chapter discusses the needs and the foreseen solutions for the GEM cooling system. The GEMs only heat source is the one dissipated by the electronics mounted on the detector surface. As in many other gaseous detectors, the temperature of the chamber affects the operation of the GEMs and the optimal working conditions are met when the chamber volume is kept between 18 and 24°C. As per design, the uniformity of such temperature shall be better than ±1°C over the whole chamber volume. Stability of the temperature shall be kept below 1°C. For this reason, the heat dissipated by the electronics shall be conveyed to an active cooling system and the transmission of such heat to the chamber shall be as much as possible limited. The power dissipation depends on the electronics design chosen. In case VFAT electronics is implemented, each one of the 72 chambers will dissipate 34W, for a total of about 2.5kW. In case the GdSP electronics design is adopted, each chamber will dissipate 51W, for a total of about 3.7kW.

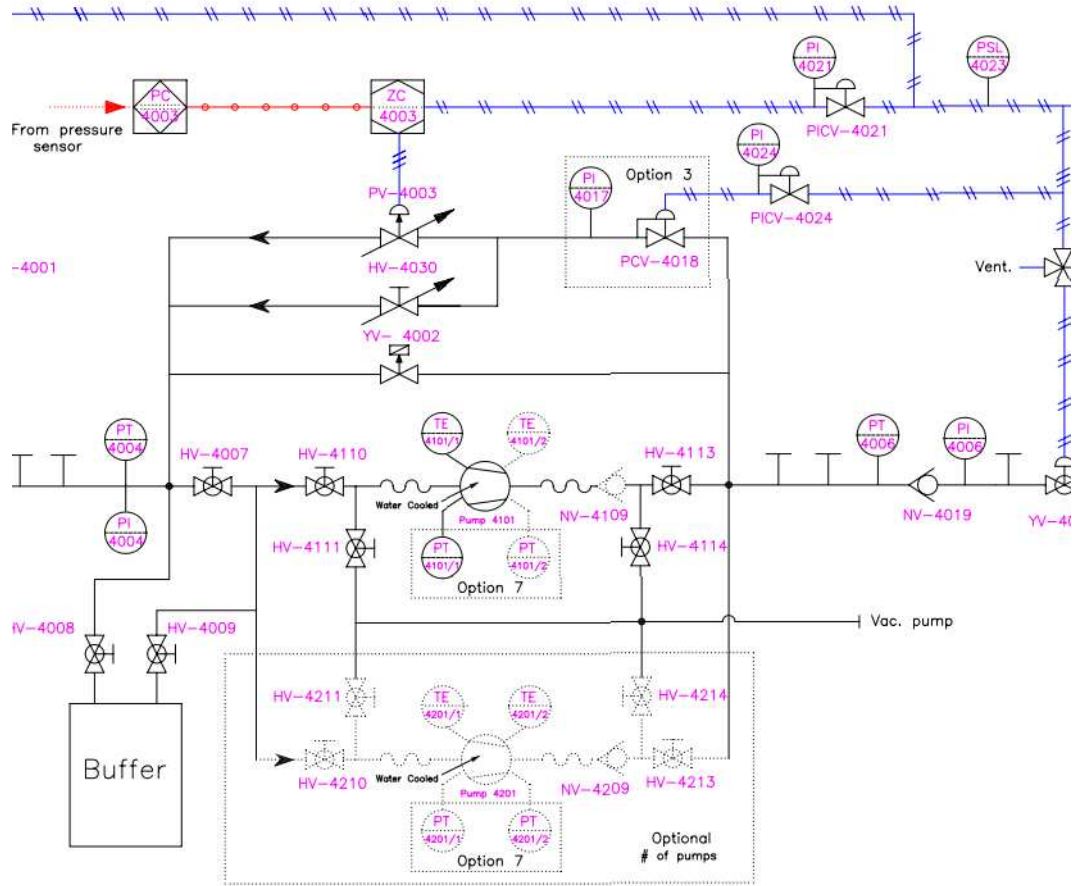


Figure 71: Layout of the pump compressor.

The baseline design of the detector on-board cooling foresees a copper pipe serpentine routed on the chamber surface between the electronics components. Optimization of the pipe routing is still under development to fine-tune the heat dissipation in the best possible manner. Thermal contact between the pipe and the electronics shall be optimized and tests must be performed on a prototype as soon as available.

Considering the location of the GEMs chambers, a very practical option for the cooling design would be to use the existing Endcap cooling circuit. Such system is presently feeding with demineralized water the existing CSC and RPC chambers. On such chambers, the cooling is now distributed through 6mm inner diameter copper pipes (to be cross-checked with Ian Crotty for RPC and Armando Lanaro for CSC). On such system, some power could be

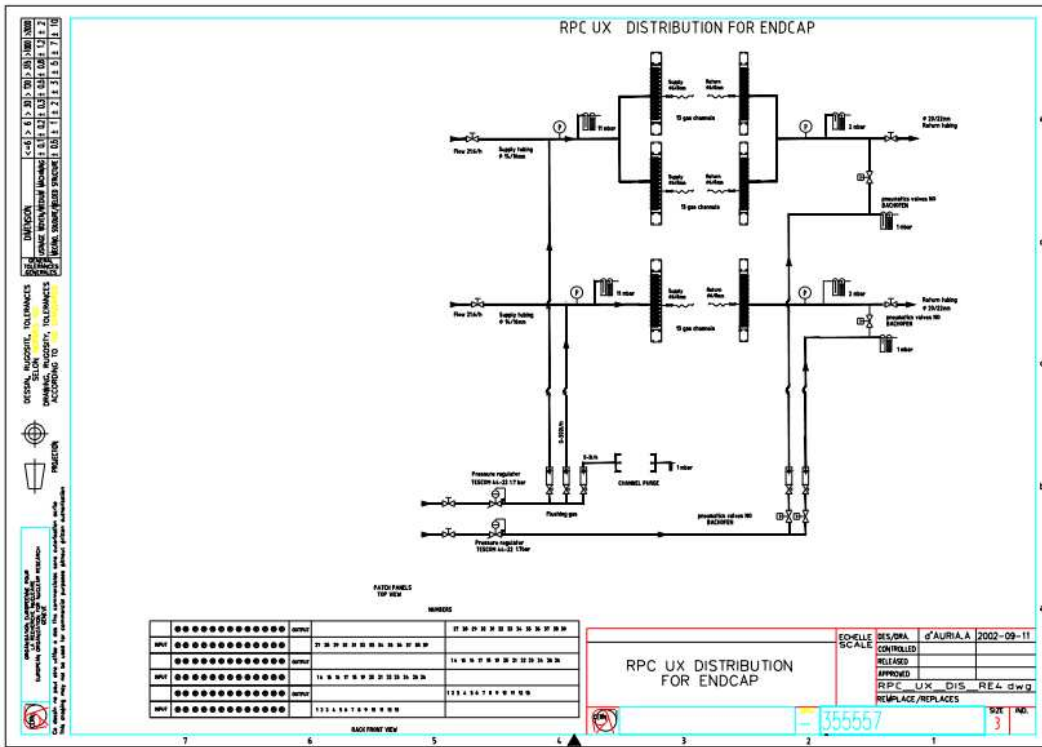


Figure 72: Layout of the gas distribution rack.

available for the cooling of the GEM chambers, provided the requirements of water purity, stability and DT does not exceed the one initially foreseen for the RPC chambers of YE1.

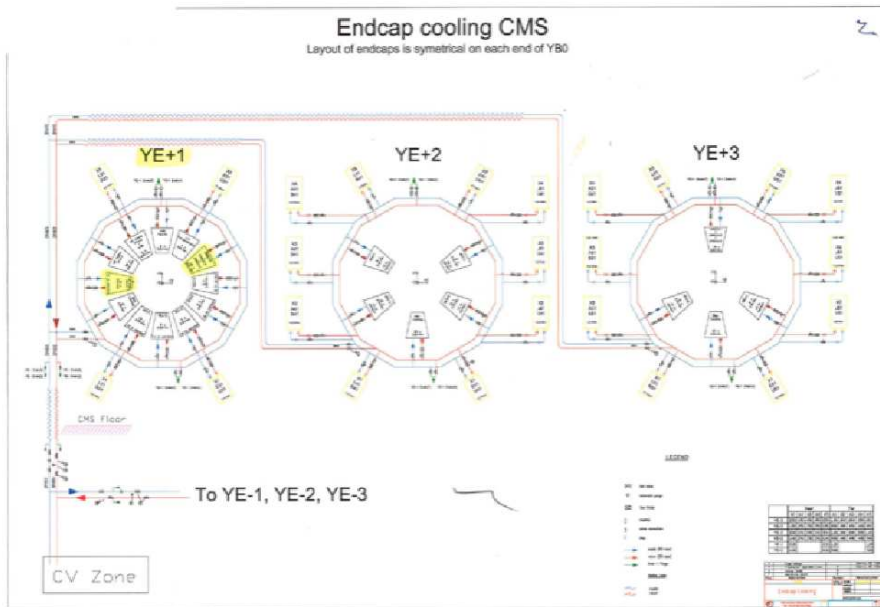


Figure 73: Endcap cooling system.

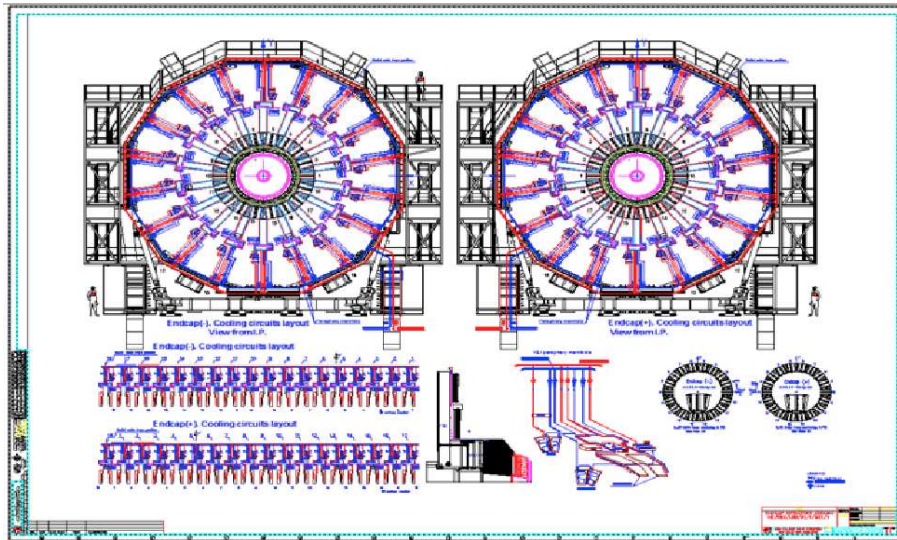


Figure 74: Endcap cooling system, main manifolds.

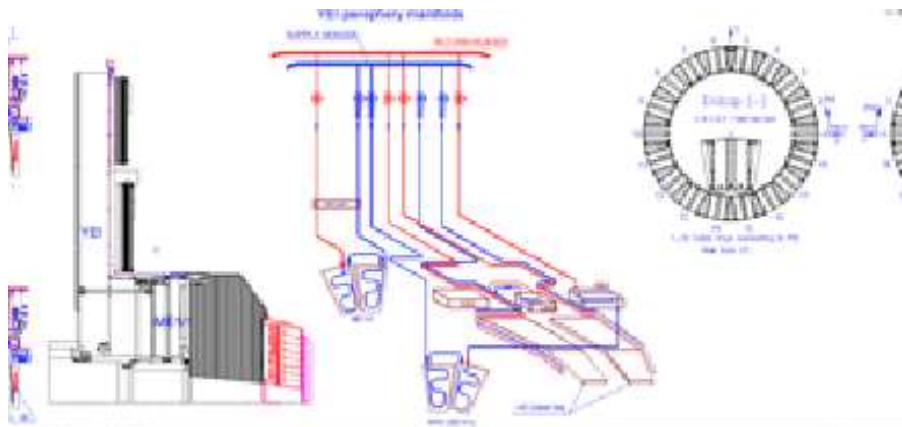


Figure 75: Endcap cooling system layout.

8 Schedule and milestones toward GE1/1 and 2/1 installation in LS2

The overall schedule for the production of two stations GE1/1 and GE2/1 is presented (next page) as a function of months and years from the approval of the construction project. It is assumed that the production of GEM foils will take place at CERN in the surface treatment workshop, as explained in Sect. 5.4.

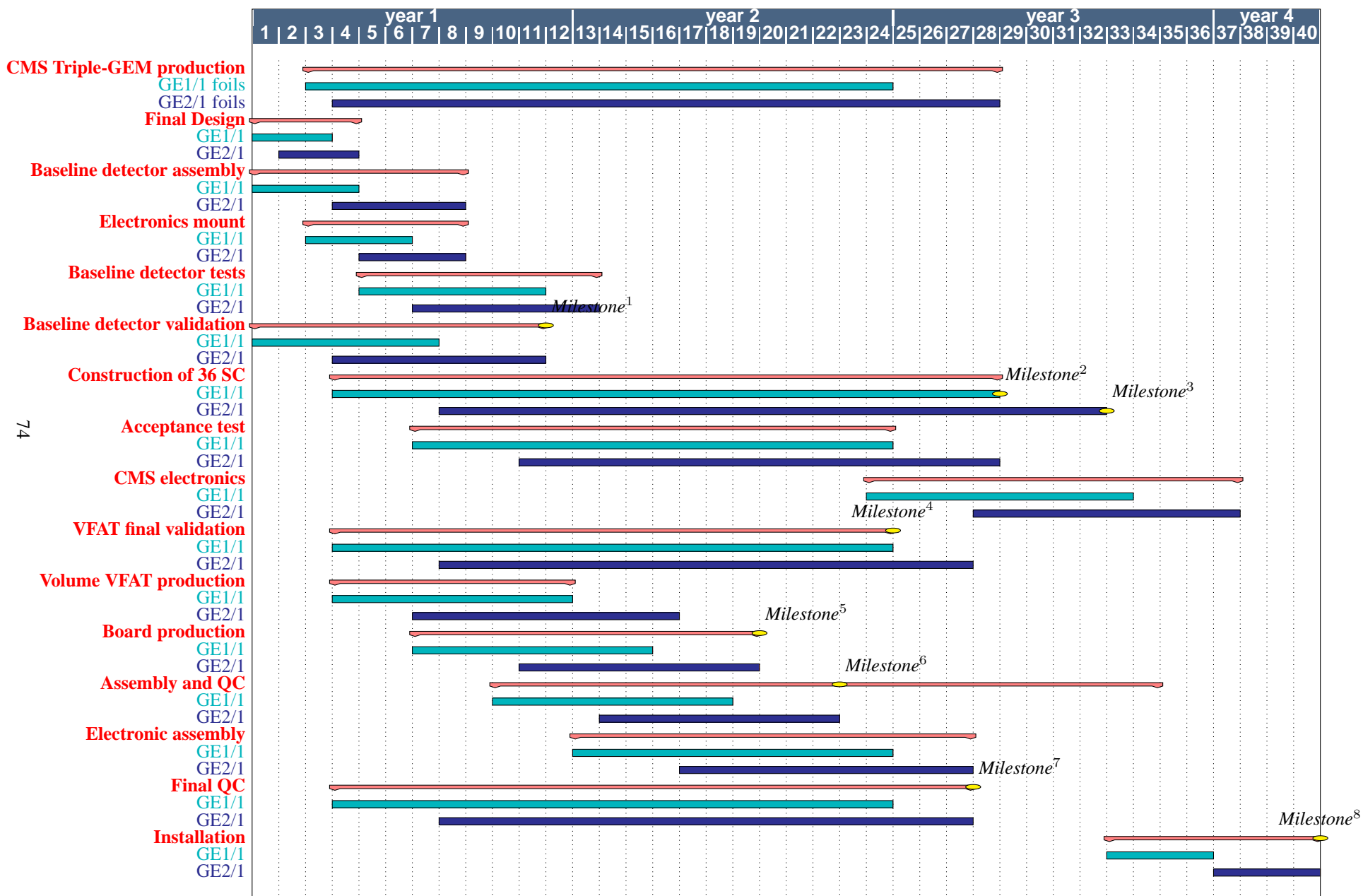
The two stations will be launched as soon as the project is approved and it is estimated that assembly tests and quality control procedures will be completed in two years per station. We will have two assembly lines in the new workshop and the TIF. Detector tests with final electronics will be done after the delivery of the final electronics in a final stage before installation in LS2.

Distributing the detector assembly in different sites and institutions to optimize time and resources has been considered. Detailed plan of sharing the tasks will be made after project approval.

The major milestones are shown in Table 17.

Table 17: Summary of milestones.

Milestones	Activities	Time (months)	Time (years)
Milestone 1	Baseline detector validation	11	0.9
Milestone 2	Construction of 36 GE1/1 SuperChambers (SC)	28	2.3
Milestone 3	Construction of 36 GE2/1 SuperChambers (SC)	32	2.7
Milestone 4	VFAT final validation	24	2
Milestone 5	Board production	19	1.6
Milestone 6	Assembly and QC	28	2.3
Milestone 7	Final QC	27	2.3
Milestone 8	Installation	40	3.3



9 Budget and resources

The budget and resources are shown in Table 18 for the construction of 160 Triple-GEM detectors. The price of the GEM foils has been largely reduced recently due to technological advances in the last two years. With most of the fabrication taking place at CERN using the new assembly and production facilities being prepared (see Section 5.4), the drift planes, readout planes and the complete detector assembly will be done under one roof lending an optimization of the resources shown under the heading “Detectors”.

The quality control of the detectors will be done as explained in Section 5.4 and the relevant cost is shown under the heading of ‘Chamber QC’. The installation of the two stations and services namely gas and cooling, comprise a large fraction of the costs as explained in items 3-6. These costs are extrapolated from the actual costs incurred in the installation and commissioning of the RPC stations.

The total cost is 7.5 MCHF, of which 4 MCHF is the cost of electronics. The number of channels that have been considered is 270 K for the GE1/1 station and 2.5 million for the GE2/1 station to enhance also the tracking and triggering option in the best possible manner, as discussed in Section 5. The cost for number of channel is marginal once the initial cost for electronics developments have been incurred.

The participating institute await the approval to approach their respective funding agencies for commitment to the project and initial indications are positive. In comparison the present RPC system readout is 70 K channels for the barrel and 40 K channels in the forward system.

Table 18: Budget and resources based on previous experience. We have considered approximately 2.2 MCHF for the electronics; this includes approximately 522 kCHF for the front-end ASIC silicon cost.

Item	GE1/1 80 detectors GE2/1 160 detectors	GE1/1 [kCHF]		GE2/1 [kCHF]		GE1/1 & GE2/1 [kCHF]
	Deliverables	price/detector	total station	price/detector	total station	total price
1	DETECTORS	5	400	5	800	1200
	Readout circuits	0.4		0.4		
	GEMs and drift planes	3.6		3.6		
	Drift board	0.5		0.5		
	Frames	0.05		0.05		
	Detector assembly	0.3		0.3		
	HV, connectors	0.05		0.05		
	Testing	0.1		0.1		
2	CHAMBER QC		500		500	1000
	Infrastructure at site		220		220	
	Assembly consumables		100		100	
	QC tools		130		130	
	Shipments		50		50	
3	INSTALLATION		350		350	700
	Consumables		50		50	
	Mechanics / tooling		100		100	
	Commissioning		150		150	
4	GAS SYSTEM		50		50	100
5	COOLING		50		50	100
6	POWER SUPPLIES					
7	HV&LV systems		170		220	390
	Cables		100		120	
	Signal		20		30	
	HV&LV DCS		20		30	
	LB Fiber		10		10	
	HV connectors / components		10		20	
	LV connector / components		10		10	
8	ELECTRONICS		2147	1955	1852	3999
	Electronics development		1240		1048	2288
	Chips	4.8	51	1.2	51	102
	Optoelectronics		51		51	102
	Electronics cards		557		660	1320
	Crates, Test Boards		66		66	132
	Control		30		30	60
	Pool rental		48		48	96
	GRAND TOTAL					7489

10 Collaboration structure

The proto-collaboration pursuing the GEM upgrade project for CMS described here constituted itself during the CMS week in March 2011 as the “GEM Collaboration (GEMs for CMS)”. We anticipate that the collaboration will rename itself simply as CMS GEM Collaboration (in analogy to the CMS DT, RPC, and EMU collaborations) if this technical proposal is accepted and the project moves forward. This international proto-collaboration currently comprises 20 institutions and ≈ 120 collaborators with 19 of the 20 institutions full CMS institutions and one associated institution. Ten additional CMS institutions have signaled their interest in joining the collaboration by signing this technical proposal.

An overview of its current organizational structure is shown in the organigram⁵⁾ in Fig.77.

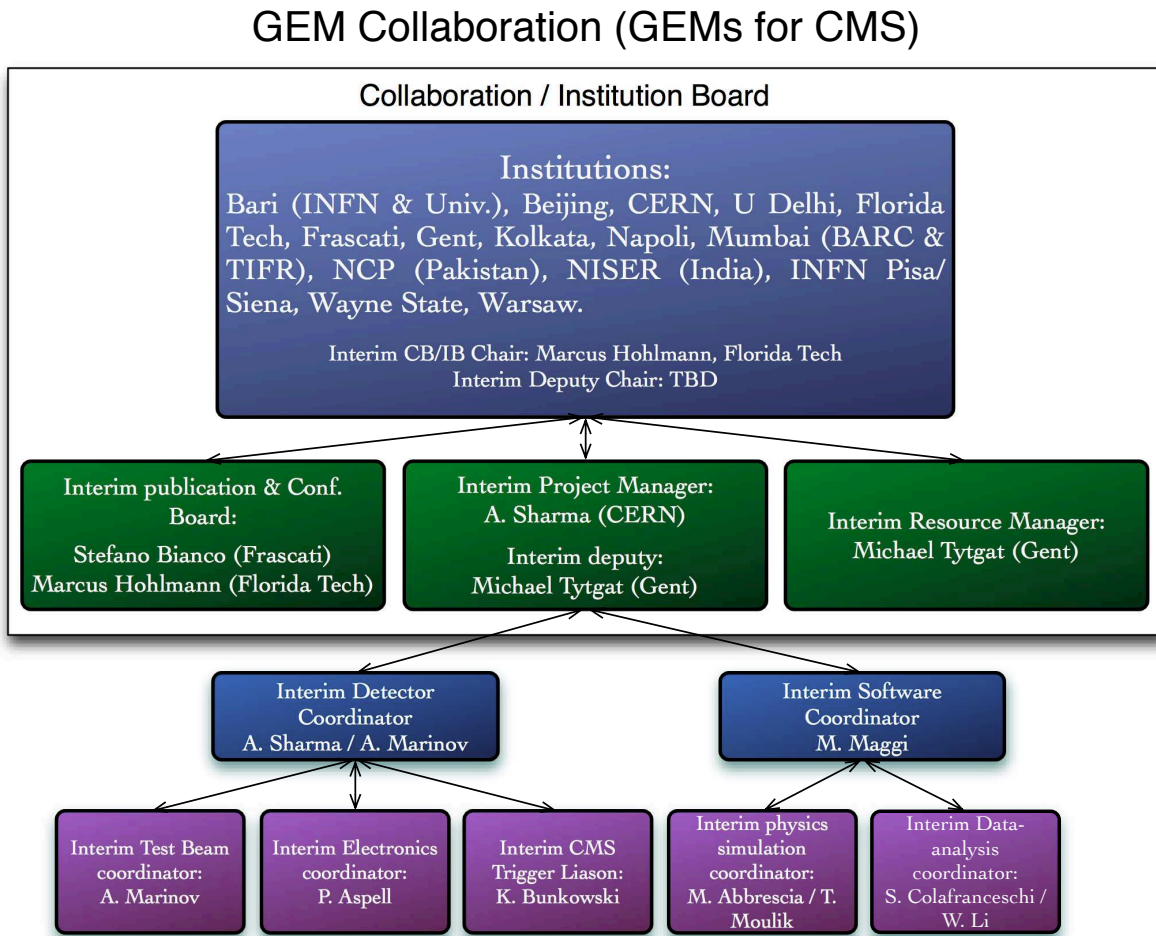


Figure 77: Current organigram of the proto-collaboration.

An interim management board was formed at the time of constitution that comprises the interim project manager, Archana Sharma (CERN), and her interim deputy, Michael Tytgat (Gent), and the interim chair of the collaboration board (Marcus Hohlmann, Florida Tech). Duccio Abbaneo (CERN) served as interim deputy chair of the collaboration in 2011, but cannot continue due to other obligations at CERN. A new interim deputy chair is to be named by the proto-collaboration in early 2012. Technical working groups on detector issues and software issues were formed that report to the project managers. Financial issues related to production and testing of prototypes are being overseen by a resource manager. A Publications and Conference Board coordinates review and submission of abstracts and proceedings to relevant conferences via the CMS CINCO system. In 2011, the collaboration contributed presentations to eight international conferences and published six proceedings papers. Project managers, resource manager, and Publication & Conferences Board report to the institution board.

⁵⁾ For this document the author list has been broadened to include collaborators who support the proposal and may join the project in future, while the structure and size of the collaboration that has carried out the feasibility studies so far is described here.

A twiki page (<https://twiki.cern.ch/twiki/bin/view/MPGD/CmsGEMCollaboration>) has been set up to facilitate communication within the proto-collaboration. It provides, for example, links to the conference contributions and publications produced by the proto-collaboration.

11 Summary and conclusion

Based on the results of the detailed R&D work presented here, we conclude that a radiation-tolerant GEM detector system represents a desirable and viable option for upgrading the $1.6 < |\eta| < 2.4$ region of the CMS muon endcap system for the era of the high-luminosity LHC. Adding the GEM subsystem improves momentum resolution for high- p_T endcap muons in the TeV region and increases the robustness of the muon trigger by providing an independent second trigger path for the forward muon region. Trigger turn-on curves will be much sharper for the GEM system than for the originally planned RPC system. These attributes of the proposed GEM system will strengthen the ability of CMS to control its muon trigger rates in the ever more challenging running environments of the future.

Extensive prototyping has demonstrated that the step from small prototypes to full-size GEM chambers as needed for CMS is clearly feasible. The full-size prototypes achieve the required efficiencies and resolutions. Integration and installation studies show that the GEM chambers can indeed be integrated into the given CMS high- η envelope. Our studies indicate that there are no known show-stoppers with respect to needed services, i.e. cooling, cabling, and gas distribution. A first design of on- and off-detector electronics for the readout of the GEM detector system addresses the major readout and trigger concerns. This design makes much use of ongoing generic electronics developments for the LHC upgrades within the community.

The ground work for launching into industrial GEM production has been laid. The projected chamber production and infrastructure schedule and milestones will allow the system to be installed during the second long LHC shutdown LS2 (currently anticipated for 2017/2018). Budget estimations and resources outlay show that two full GEM stations (GE1/1 and GE2/1) could be produced and commissioned at an equipment cost of 7.5 MCHF. An organisational structure is well in place for the multi-institutional collaboration that is proposing to take on this upgrade project.

Consequently, we conclude that this project is ready to move forward and request that this proposal of a “GEM detector system for an upgrade of the CMS muon endcaps” be approved. This will allow the project to be integrated into the official CMS upgrade program, which in turn will allow the participating institutions to approach their respective national agencies with funding requests for the project.

Acknowledgment This work has partly been performed in the framework of the RD51 Collaboration. The authors that are members of the CMS Collaboration would like to explicitly thank the RD51 Collaboration for its continuous support of this work, for the many fruitful discussions, for the close collaboration during the test beam campaigns and for dedicating part of their lab space at CERN to this project.

12 Publications

2010

1. Characterization of GEM Detectors for Application in the CMS Muon Detection System 2010 IEEE Nucl. Sci. Symp. Conf. Rec. 1416-1422; RD51 Note 2010-005; arXiv:1012.3675v1
2. Construction of the first full-size GEM-based prototype for the CMS high- η muon system 2010 IEEE Nucl. Sci. Symp. Conf. Rec. 1909-1913; RD51 Note 2010-008; arXiv:1012.1524v2
3. Gas Flow Simulations for Gaseous Detectors 2010 IEEE Nucl. Sci. Symp. Conf. Rec. 1454-1456; RD51 Note 2010-009

2011

1. Thermal Stretching of Large-Area GEM Foils Using an Infrared Heating Method; RD51 Note 2011-004.
2. Test Beam Results of the GE1/1 Prototype for CMS High- η Muon System Future Upgrade, NSS-MIC2011 N19-7; RD51-Note-2011-013; arXiv:1111.4883 [physics.ins-det].
3. Simulation of a Triple-GEM detector for a potential CMS muon tracking and trigger upgrade, Submitted to the Proc. of the Technology and Instrumentation in Particle Physics 2011 (TIPP 2011) Conference, 9-14 June, 2011, Chicago, IL, USA.
4. Performance studies of large-area Triple-GEM prototypes for future upgrades of the CMS forward muon system, Proc. of EPS-HEP 2011, July 21-27, 2011, Grenoble, France.
5. Construction and Performance of full scale GEM prototypes for future upgrades of the CMS forward Muon system, Proc. of the 13th ICATPP Conference on Astroparticle, Particle, Space Physics and Detectors for Physics Applications; Oct 3-7, 2011; Como, Italy.
6. Construction and Performance of Large-Area Triple-GEM Prototypes for Future Upgrades of the CMS Forward Muon System, NSS-MIC2011 N19-7; RD51-Note-2011-012; arXiv:1111.7249v1 [physics.ins-det]
7. Transport Properties of operational gas mixtures used at LHC: arXiv:1110.6761v1

13 Conference contributions

2010

1. IPRD Siena 2010, R&D for a high- η trigger and tracking detector for CMS, A. Sharma
2. 2010 IEEE Nuclear Science Symposium and Medical Imaging Conference, 23-29 October 2011, Valencia, Spain
 - (a) Characterization of GEM Detectors for Application in the CMS Muon Detection System, M. Tytgat
 - (b) Construction of the first full-size GEM-based prototype for the CMS high- η muon system, S. Colafranceschi
 - (c) Gas Flow Simulations for Gaseous Detectors, S. Colafranceschi

2011

1. CMS UPGRADE2010: Studies for the forward muon trigger algorithm, CMS Upgrade Workshop Fermilab Nov. 7-10, 2011. A. Sharma.
2. ANIMMA 2011: The Second International Conference on Advancements in Nuclear Instrumentation, Measurement Methods and their Applications, 6-9 June, 2011, Gent, Belgium Characterization of a Full-Size Triple-GEM Prototype for the CMS Muon Detection System, A. Marinov.
3. TIPP 2011: Technology and Instrumentation in Particle Physics, 9-14 June 2011, Chicago, IL, USA

- (a) Performance of a Large-Area Triple-GEM Detector in a Particle Beam, P. E. Karchin.
 - (b) Simulation of a Triple-GEM detector for a potential CMS muon tracking and trigger upgrade, T. Moulik.
4. EPS-HEP 2011: EPS High Energy Physics Conference, 21-27 Jul 2011, Grenoble, Isre, France
- (a) Performance studies of large-area Triple-GEM prototypes for future upgrades of the CMS forward muon system, S. Tupputi.
5. MPGD 2011: 2nd International Conference on Micro Pattern Gaseous Detectors, 29 Aug-1Sep 2011, Kobe University, Japan
- (a) An overview on the design, construction and performance of large area Triple-GEM prototypes for future upgrades of the CMS forward muon system, A Sharma.
6. ICATPP 2011: 3rd International Conference on on Advanced Technology and Particle Physics: Astroparticle, Particle, Space Physics, and Detectors for Physics Applications, 3-7 Oct 2011, Como, Italy
- (a) A dedicated beam test for the full scale GEMs for CMS prototype in a strong magnetic field, M. Zientek.
 - (b) Construction and Performance of full scale GEM prototypes for future upgrades of the CMS forward Muon system, S. Colafranceschi.
7. 2011 IEEE Nuclear Science Symposium and Medical Imaging Conference, 23-29 October 2011, Valencia, Spain
- (a) Construction and Performance of Large-Area Triple-GEM Prototypes for Future Upgrades of the CMS Forward Muon System, M. Tytgat.
 - (b) Test beam results of the GE1/1 prototype for CMS high- η muon system future upgrade, S. Colafranceschi.

References

- [1] S. Chatrchyan *et al.*, CMS Collaboration, The CMS experiment at the CERN LHC, *J. Instrum.* 3 (2008) S08004 9, 60
- [2] R. Santonico, “RPC: Status and perspectives”, <http://www.slac.stanford.edu/spires/find/hep/www?irn=3140032> In *Pavia 1993, Proceedings, The resistive plate chambers in particle physics and astrophysics 1-11. 10
- [3] F. Sauli, A. Sharma, Micropattern Gaseous Detectors, *Annu. Rev. Nucl. Part. Sci.* 1999.49:341-88. 10
- [4] RD51 Collaboration, <http://rd51-public.web.cern.ch/RD51-Public/>. 10, 20
- [5] Workshop on Resistive Plate Chambers and Related Detectors (RPC 2010) Volume 661, Supplement 1 (2012). 10
- [6] G. Abbiendi, *et al.*, Muon Reconstruction in the CMS Detector, *CMS AN 2008/097* (2009). 16
- [7] I. Giomataris, MICROMEAS: results and prospects, *Nucl. Instr. and Meth.* A419 (1998) 239. 20
- [8] F. Sauli, GEM: A new concept for electron amplification in gas detectors, *Nucl. Instr. and Meth.* A386 (1997) 531. 20
- [9] D. Abbaneo *et al.*, Characterization of GEM Detectors for Application in the CMS Muon Detection System, 2010 IEEE Nucl. Sci. Symp. Conf. Rec 1416-1422; RD51 Note 2010-005; arXiv:1012.3675v1. 20
- [10] D. Abbaneo *et al.*, Characterization of GEM Detectors for Application in the CMS Muon Detection System, 2010 IEEE Nucl. Sci. Symp. Conf. Rec 1416-1422; RD51 Note 2010-005; arXiv:1012.3675v1 [physics.ins-det]. 20
- [11] S. Duarte Pinto *et al.*, Progress on large area GEMs, *JINST* 4 (2009) P12009; M. Villa *et al.*, *Nucl. Instr. and Meth.* A628 (2011) 182-186. 20
- [12] P. Aspell *et al.*, VFAT2: A front-end system on chip providing fast trigger information, digitized data storage and formatting for the charge sensitive readout of multi-channel silicon and gas particle detectors, Proc. of the Topical Workshop on Electronics for Particle Physic (TWEPP2007), Prague, Czech Republic, September 3-7, 2007. 21
- [13] G. Antchev *et al.*, TOTEM Detector at LHC, *Nuclear Instr. Methods Phys. Res. A* 617(2010) 62-66. 21, 36
- [14] L. Jones *et al.*, The APV25 deep sub micron readout chip for CMS channels detectors, Proc. of 5th workshop on Chips electronics for LHC experiments, CERN/LHCC/99-09, 162-16. 30
- [15] S. Martoiu, H. Muller, J. Toledo, Front-End Electronics for the Scalable Readout System of RD51, Nuclear Science Symposium Conference Record (NSS/MIC), 2011 IEEE, Oct. 23-29 Oct.2011. 30, 65
- [16] R. Veenhof, Garfield - simulation of gaseous detectors, <http://garfield.web.cern.ch/garfield/>; S. Biagi, Magboltz - transport of electrons in gas mixtures, <http://consult.cern.ch/writeups/magboltz/>. 31, 35, 38
- [17] D. Abbaneo *et al.*, Test Beam Results of the GE1/1 Prototype for CMS High- η Muon System Future Upgrade, arxiv.org/pdf/1111.4883 31
- [18] M. Alfonsi *et al.*, High-rate particle triggering with Triple-GEM detector, *Nuclear Instruments and Methods A* 518 (2004) 106112. 35, 36, 38
- [19] R. Veenhof *et al.*, Understanding the gas gain in GEM detectors (in preparation). 38, 39
- [20] A. Sharma, Properties of some gas mixtures used in tracking detectors, *SLAC-JOURNAL-ICFA*, Vol. 16, 1998. (<http://www.slac.stanford.edu/pubs/icfa/>). 36
- [21] F. M. Penning, Über den Einfluß sehr geringer Beimischungen auf die Zündspannung der Edelgase, *Z.Phys.* 46, 1928, 10.1007/BF01390558, 335-348. 38

- [22] F. M. Penning, The starting potential of the glow discharge in neon argon mixtures between large parallel plates: II. Discussion of the ionisation and excitation by electrons and metastable atoms, *Physica* 1, 1028-1044, 1934, 10.1016/S0031-8914(34)80298-4. 38
- [23] K. Bunkowski, Optimization, Synchronization, Calibration and Diagnostic of the RPC PAC Muon Trigger System for the CMS detector, CMS TS-2010/009. 43
- [24] CMS Collaboration, Physics TDR Vol I. Detector Performance and Software, CERN/LHCC 2006-001. 45
- [25] CMS Software, <http://cmssw.cvs.cern.ch/cgi-bin/cmssw.cgi/CMSSW/> 44
- [26] T. Früboes, The RPC based trigger for the CMS experiment - emulation of an algorithm and patterns optimization, http://hep.fuw.edu.pl/cms/docs/theses/MSc_fru.pdf. 44
- [27] CMS Collaboration, The Muon Project, CMS Technical Design Report, CERN/LHCC 97-32; CMS-TDR-003. 44
- [28] P. Moreira *et al.*, The GBT SerDes ASIC prototype. Published in *J. Instrum.* 5 (2010) C11016, presented at: Topical Workshop on Electronics for Particle Physics 2010. Aachen, Germany September 2010. 56
- [29] J. Troska *et al.*, Versatile Transceiver developments, published in *J. Instrum.* 6 (2011) C01089. 56
- [30] F. Faccio *et al.*, Development of custom radiation-tolerant DCDC converter ASICs. Published in *J. Instrum.* 5 (2010) C11016, presented at :Topical Workshop on Electronics for Particle Physics 2010 Aachen, Germany September 2010. 56
- [31] P. Vichoudis *et al.*, The Gigabit Link Interface Board (GLIB), a flexible system for the evaluation and use of GBT-based optical links. Published in *J. Instrum.* 5 (2010) C110167 presented at :Topical Workshop on Electronics for Particle Physics 2010. Aachen, Germany September 2010. 56
- [32] TOTEM Experiment at the CERN Large Hadron Collider. The TOTEM Collaboration. *JINST* 3 S08007, 2008, Published as part of The CERN Large Hadron Collider Accelerator and Experiments. 57
- [33] P. Aspell *et al.*, VFAT2: A front-end system on chip providing fast trigger information and digitized data storage for charge sensitive readout of multi-channel silicon and gas particle detectors. Proceedings: 2008 IEEE Nuclear Science Symposium, Dresden, Germany, October 2008. 57
- [34] CMS TDR: the Trigger System, CMS Collaboration, CERN-LHCC-2000-038 TDR. 60
- [35] K. Bukowski, Optimisation Synchronization, Calibration and Diagnostic of the RPC PAC Muon Trigger System for the CMS detector, CMS TS-2010/009. 60
- [36] GOL Project, <http://proj-gol.web.cern.ch/proj-gol>. 60
- [37] K. Banzuzi, Link System and Crate Layout of the RPC Pattern Comparator Trigger for the CMS detector, CMS IN 2002/065. 61
- [38] M. Gorski, I. M. Kudla, K. T. Pozniak, Resistive Plate Chamber (RPC) based Muon Trigger System for CMS experiment - Data Compression/Decompression System, *NIM A* 419 (1998) 701-706. 61
- [39] P. Aspell *et al.*, PACE3: a large dynamic range analog memory front-end ASIC assembly for charge readout of silicon sensors. Proceedings: 52nd IEEE Nuclear Science Symposium, San Juan, Puerto Rico, October 2005. 60, 64

Appendices

A Parameters describing the GEi/1 systems

In this appendix we describe the parameters of the two proposed stations GE1/1 and GE2/1 in terms of mechanics, electronics and technical specification of services.

Table 19: GE1/1 Mechanics

Long side	440mm
Short side	220mm
Height	990mm
Area	0.32m ²
Chamber volume	2.2869l
Super Chamber volume	4.57l
Gas flow per chamber	0.48l/h

Table 20: GE1/1 Electronics

Eta partition	10
Phi columns	3
Chamber consumption (VFAT)	34W
Chamber consumption (GdSP)	51W
Total chips	30VFATs
Channels per chamber	3840ch
Channels per super chamber	7680ch
Area/chips	10.89·10 ⁻³ m ² /chip
Consumption/channel (VFAT)	8.85·10 ⁻³ W/channel
Consumption/channel (GdSP)	13.28·10 ⁻³ W/channel

Table 21: GE1/1 System overview

Surface	23.5224m ²
Gas volume	165l
Electronics ch.	276480ch
Power consumption (VFAT)	2.448kW
Power consumption (GdSP)	3.672kW

Table 22: GE2/1 Mechanics

GE2/1long	
Long side	1250.7mm
Short side	576.8mm
Height	1911mm
Area	1.74m ²
Chamber volume	12.22l
Volume super chamber	24.44l
Gas flow per chamber	2.54l/h
GE2/1short	
Long side	1250.7mm
Short side	799mm
Height	1281mm
Area	1.31m ²
Chamber volume	9.18l
Volume super chamber	18.37l
Gas flow per chamber	1.91l/h

Table 23: GE2/1 Electronics

GE2/1long	
Chamber consumption (VFAT)	182W
Chamber consumption (GdSP)	273W
Total chips	160VFATs
Channels per chamber	20524ch
Channels per super chamber	41049ch
Area/chips	10.89·10 ⁻³ m ² /chip
Consumption/channel (VFAT)	8.85·10 ⁻³ W/channel
Consumption/channel (GdSP)	13.28·10 ⁻³ W/channel
GE2/1short	
Chamber consumption (VFAT)	137W
Chamber consumption (GdSP)	205W
Total chips	121VFATs
Channels per chamber	15431
Channels per super chamber	30862
Area/chips	10.89·10 ⁻³ m ² /chip
Consumption/channel (VFAT)	8.85·10 ⁻³ W/channel
Consumption/channel (GdSP)	13.28·10 ⁻³ W/channel

Table 24: GE2/1 System overview

Surface	125.72m ²
Gas volume	1542l
Electronics ch.	2588781ch
Power consumption (VFAT)	23kW
Power consumption (GdSP)	34kW

B Integration and installation within CMS high- η envelope

This section describe the studies of integration and installation of detectors and services at CMS. This includes project documentation.

B.1 Scope

The design, dimensions and positioning for the GEM chambers to be mounted in the YE1 nose has been studied and preliminary results are presented in this section⁶⁾.

B.2 General description

The mechanical structure is divided into 2 circular sectors, one located in ME1/1 and the other one in +ME1/1. There are 36 Super-Chambers per sector, each one covering 10° of the circle. One SC is composed of 2 trapezoidal chambers. There are 2 types of SC: all chambers are strictly identical but they are joined via 2 different types of holders, this in order to match SC between them and to have a good overlap (6.5mm) of the active area of the GEMs, while allow them entering in the narrow space (100mm, to be confirmed if possible in the next opening of the detector) existing between the Back-Flange and the Muon Chambers, volume where the SCs will be mounted (Fig. 78). All screws and materials are not-magnetics. Heli-coils are not foreseeing in principle. The 3D modeller used is CATIA V5, standard at CERN. Few drawings have been printed for the first prototypes. Final execution drawings to be produced.

B.3 Documents

Table 25: System overview: Endcap disks 1

	GE1/1	RE1/2	RE1/3
Chambers	18·2·2=72		
η segments	8		
Φ coverage	20		
strips/ η segment	384		
Channels/chamber	3072		

Table 26: System overview: Endcap 2

	GE2/1	RE2/2	RE2/3
Chambers	36·2·2=144		
η segments	8		
Φ coverage	10		
strips/ η segment	384		
Channels/chamber	3072		

Table 27: System overview: Endcap 3

	GE3/1	RE3/2	RE3/3
Chambers	18·2·2=72		
η segments	4		
Φ coverage	20		
strips/ η segment	384		
Channels/chamber	3072		

⁶⁾ Adopted Acronyms: AD Applicable Document; PR Reference drawing; RD reference document; CMS Compact Muon Solenoid Experiment; SC Super-Chamber; CoG Centre of Gravity; TBC To be confirmed; TBD To be determined; PA Applicable drawing.

Table 28: System overview: Endcap 4

	GE4/1	RE4/2	RE4/3
Chambers	18·2·2=72		
η segments	4		
Φ coverage	20		
strips/ η segment	384		
Channels/chamber	3072		

Table 29: System overview: Dimensions

Station	R_i (mm)	R_o (mm)	A (mm)	B (mm)	C (mm)	D (mm)	Thickness	Z position detector
1/1	1363	2396	1037	526	345	1033	36	5651
2/1	1960	3241	1301	1251	799	1281	36	7865
3/1	2435	3241	819	1251	966	806	36	9775
4/1	2655	3241	595	1251	1044	586	36	10676

B.3.1 Applicable documents

B.3.2 Drawings

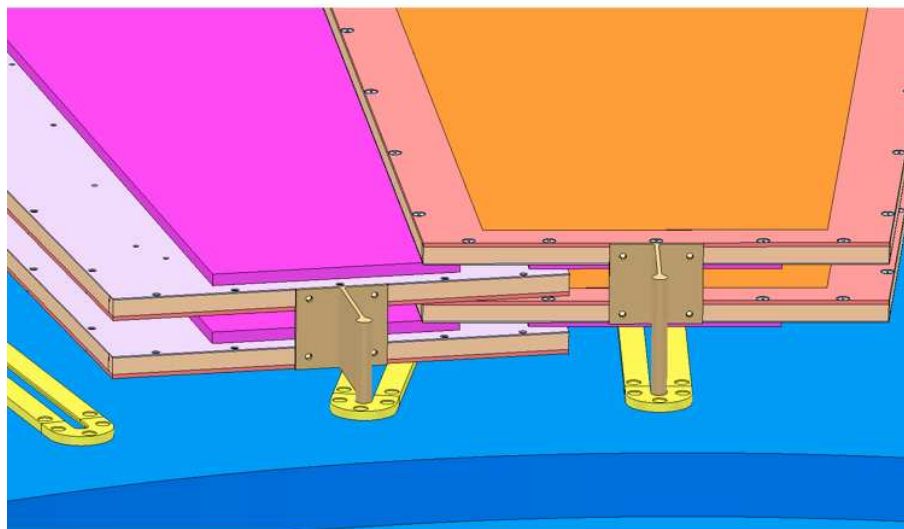


Figure 78: According to the integration studies there is enough space to insert a sandwich of two Triple-GEM detectors (Super-Chamber).

B.3.3 Reference documents

B.3.4 Super-chamber characteristics

Chamber weight : 18.2 kg (electronics & services not included) Centre of Gravity location : TBD Chamber referential definition: See drawing below

B.3.5 Super-chambers referential definition

The following sketch provides the definition of X, Y, Z directions and phi, eta angles:

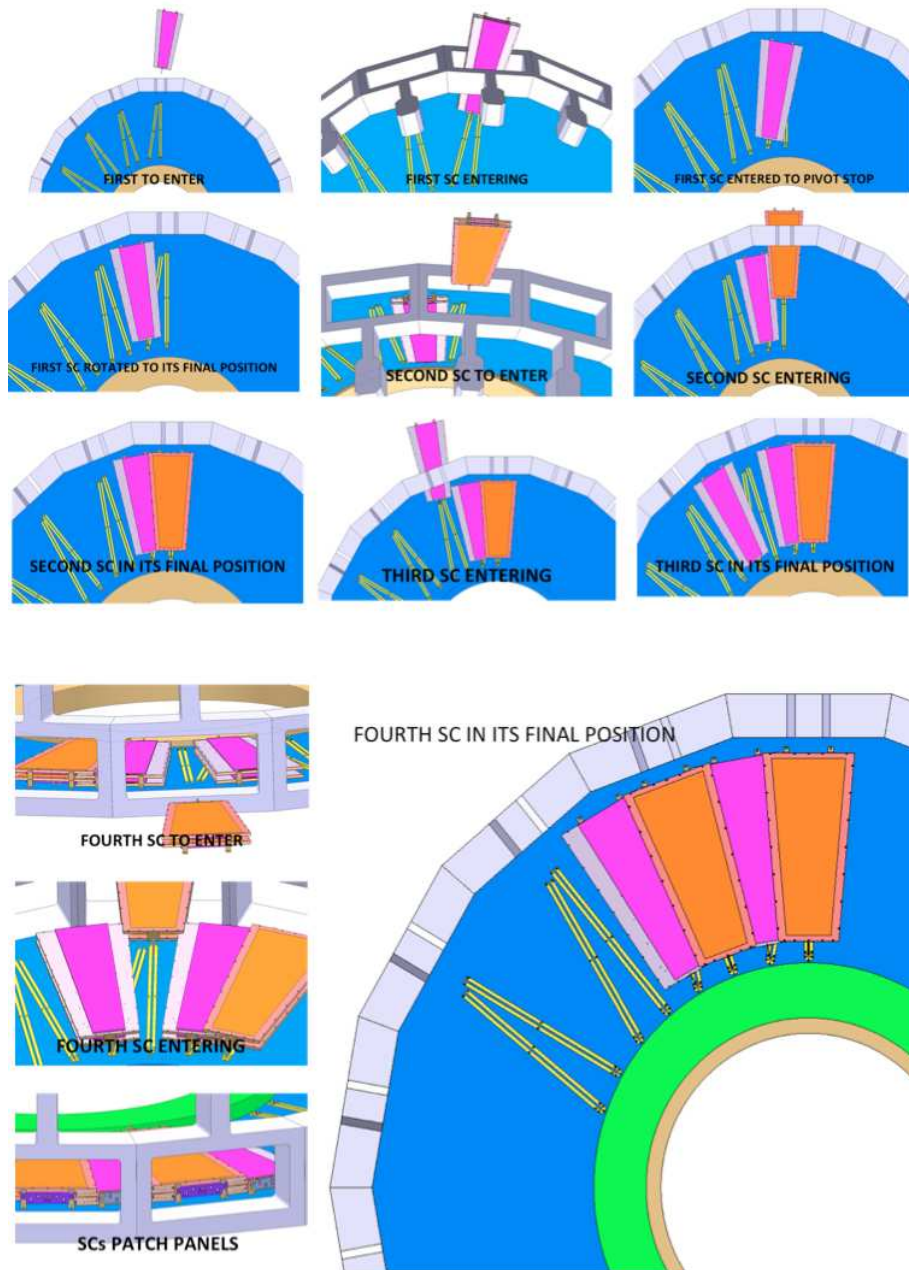


Figure 79: Installation sequence studies.

B.3.6 Envelope and location

B.3.7 Assembly sequence of a chamber

The geometry of the available volume where the chambers will be installed is a flat bored cylinder with an internal diameter of 2480mm, an external diameter of 4960mm, a minimum thickness of 100mm and a distance to the Interaction Point of 5641mm in Z direction. The distance from the beamline to the axis of the pivoting parts of the chambers is 1274mm in Y direction.

B.4 Assembly and installation

The overall dimensions of a chamber are in mm : 1038x530x17 (26 if you count the chimney).

The overall dimensions of the SCs, are in mm: 1170x530x98 for the higher SC (or straight SC) and 1170x530x80 for the lower SC (or pivoting SC).

Notice that pivot and feet must both be mounted with a rotation of 180° with respect to the chimney, depending on the type of SC. If better mounting precision would be needed, the central screws of the feet can be replaced by pins. Similar solution for pivots

Due to the weight of each SC, a jig could be necessary for the insertion. The one which was used for the Muon chambers could probably be adapted for that purpose (Fig. 78). The rails with T-grooves, for sliding and then stopping (eventually rotating) the SC, are already mounted in the back-flanges of CMS.

B.5 Preliminary considerations GE2/1

Based on the work accomplished for GE1/1, we have begun studies with the purpose of also installing GEM chambers in the zone ME2/1, more exactly on the backside of YE1 (compression side).

This zone was in principle foreseen for containing RE2/1 chambers but they have never being mounted there. In fact, only RE2/2 and RE2/3 were installed. In the following photo, the red painted circle on the yoke would be the place to be used for GE2/1 chambers:

In each side of the detector the set consists of 18 GE2/1 chambers, each spanning 20° in ϕ angle. As seen in GE1/1, the GE2/1 chambers overlap to provide continuous coverage in ϕ . There are 2 possible geometries to be envisaged. They depend on the possibility of cantilever a part of each chamber on top of the neutron shielding of YE/1 disk (short version in blue, long version in grey). As you can see above, the distance from the beamline to the bottom side of the chamber is 1960 (short version). Hereafter its shown the distance from the IP to the backside of the yoke (7869mm), but the gap between the yoke and the chambers is not definitely determined yet.

C Project organization

In this appendix we describe the organization of the project and its services for documentation and retrieval purposes

C.1 Project organization for retrieval & DB

Project: GEM Project

State: Active

G: [/Workspaces/c/cmsintegration/CMSinCATIA/Projects/GEMProject](G:/Workspaces/c/cmsintegration/CMSinCATIA/Projects/GEMProject)

Project Role(s)

Project Manager: SHARMA Archana 164875

Engineering Supervisor: CONDE GARCIA Antonio 160859 and BALLY Stephane 162854

Production Supervisor: CHATELAIN Jean-Paul 160903

Time Line

2011 0816 Done (Gas System Diagram, Cooling System Diagram, Electronics System Diagram)

2011 0817 Requested (Cooling 3D/2D Design Retrieval) Boki shall provide CATIA models from Racks to Periphery Patch Panels

2011 0817 Requested (Cooling 3D/2D Design Retrieval) Boki shall provide CATIA models of Manifold

Q&A

Where do I find documentation about the as-installed Gas RE1/1 Design?

Document 810786 v.1 YE+1 - AS BUILT GAS DRAWINGS

Document 826202 v.1 YE-1 - AS BUILT GAS DRAWINGS

These documents require COVERT TO CATIA process!

Where do I find documentation about the as-installed Cooling RE1/1 Design?

empty

Where do I find documentation about the as-installed Electronics RE1/1 Design?

empty

C.2 Task(s)

Meeting(s), Workshop(s): <https://indico.cern.ch/categoryDisplay.py?categId=1865>

System(s) involved

...

System Role(s)

...

RPC Detector Gas: GUIDA Roberto PH/DT 162146

Water Detector Cooling: FRANK Norbert PH/CMX 163618 and TROPEA Paola 164999

Electronics: ASPELL Paul PH/ESE 168526

Low Voltage: MARINOV Andrey PH/UCM 71656

High Voltage: ASPELL Paul PH/ESE 168526

Signal: ASPELL Paul PH/ESE 168526

Temperature/Humidity Sensor: COLAFRANCESCHI Stefano 162881

C.3 Electronics system

System Diagram (Physical)

...

C.4 Product(s) involved

1. GE 1/1 Single layer Chamber
2. GE 1/1 Double layer Chamber
3. GE 2/1 Chamber

G:/Workspaces/c/cmsintegration/CMS_Upgrades/RE_1_1_GEM

Products are described by a 3D model (CATIA file format). Optionally a Adobe Acrobat (pdf) file can be generated to ease the manipulation/visualization/measuring of such model.

GE 1/1 Single layer Chamber

Dimensions: 1 m x 2 m x 10 cm

Mass: 10 kg

Version(s): A, B

State: Obsolete, Released

Product Model

GE 1/1 Double layer Chamber

Dimensions: 1 m x 2 m x 10 cm

Mass: 15 kg

Version(s): A

State: In Work

Product Interface

	Physical Interface	Logical Interface
Gas	1 Supply + 1 Return	Idem
Cooling	1 Supply + 1 Return	Idem
Electronics	1 High Voltage	?
	1 Low Voltage	?
	6 Signal	?

Product Model

GE 2/1 Chamber

D Full simulation results for trigger studies with GEM

Fig. 80-91 show simulated trigger turn-on curves for trigger towers 14-16, i.e. the L1 trigger efficiencies for all geometry variations and for three different p_T thresholds (16, 50, and $140 \frac{\text{GeV}}{c}$) as a function of the true muon transverse momentum. Similar results for trigger tower 13 can be found in chapter 5.

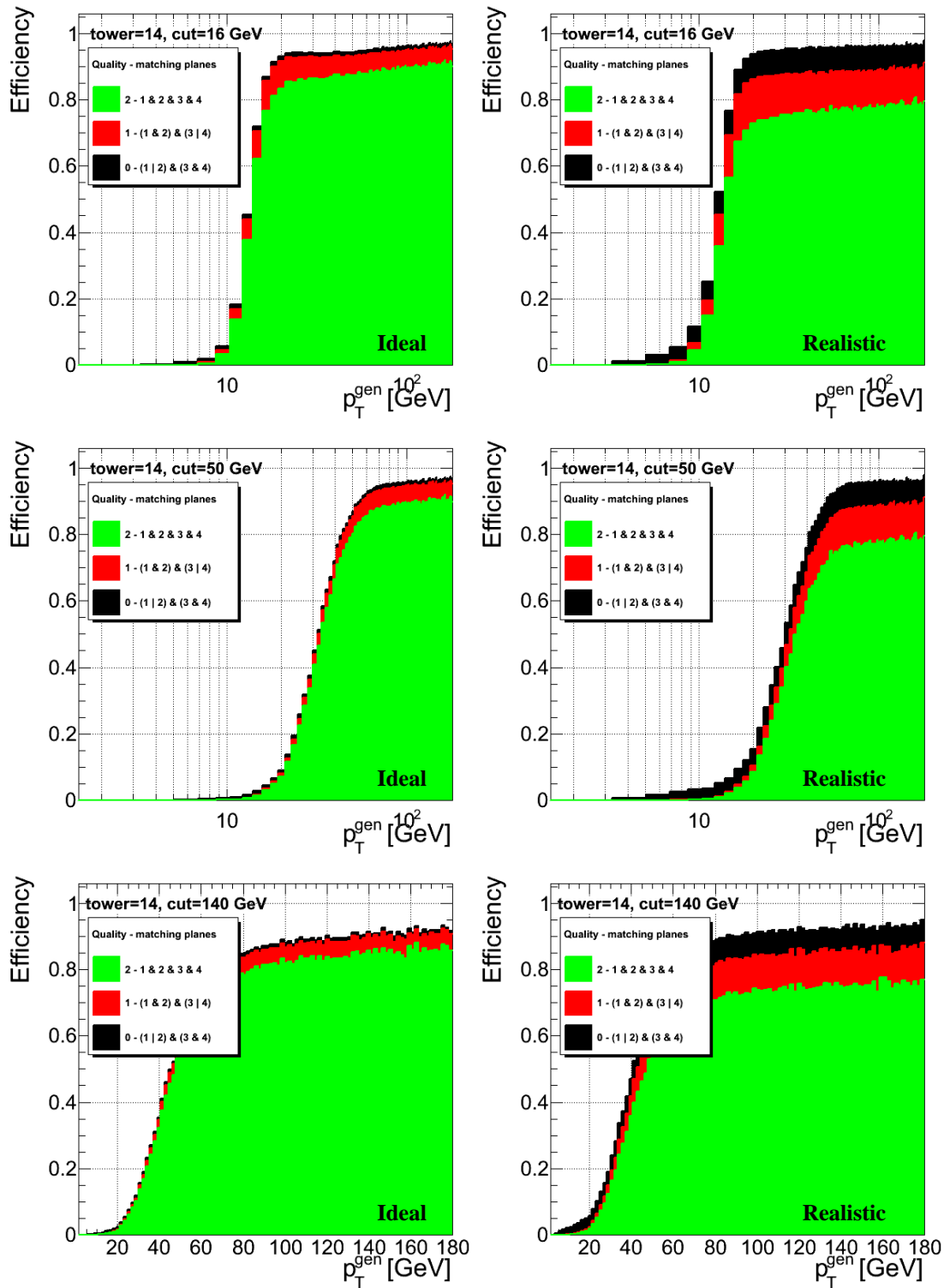


Figure 80: L1 GEM+RPC trigger efficiency curves in trigger tower 14 for base geometry. Rows correspond to 3 different p_T thresholds of 16, 50, and $140 \frac{\text{GeV}}{c}$, respectively. Left column shows results for ideal chamber model, right for realistic chamber model.

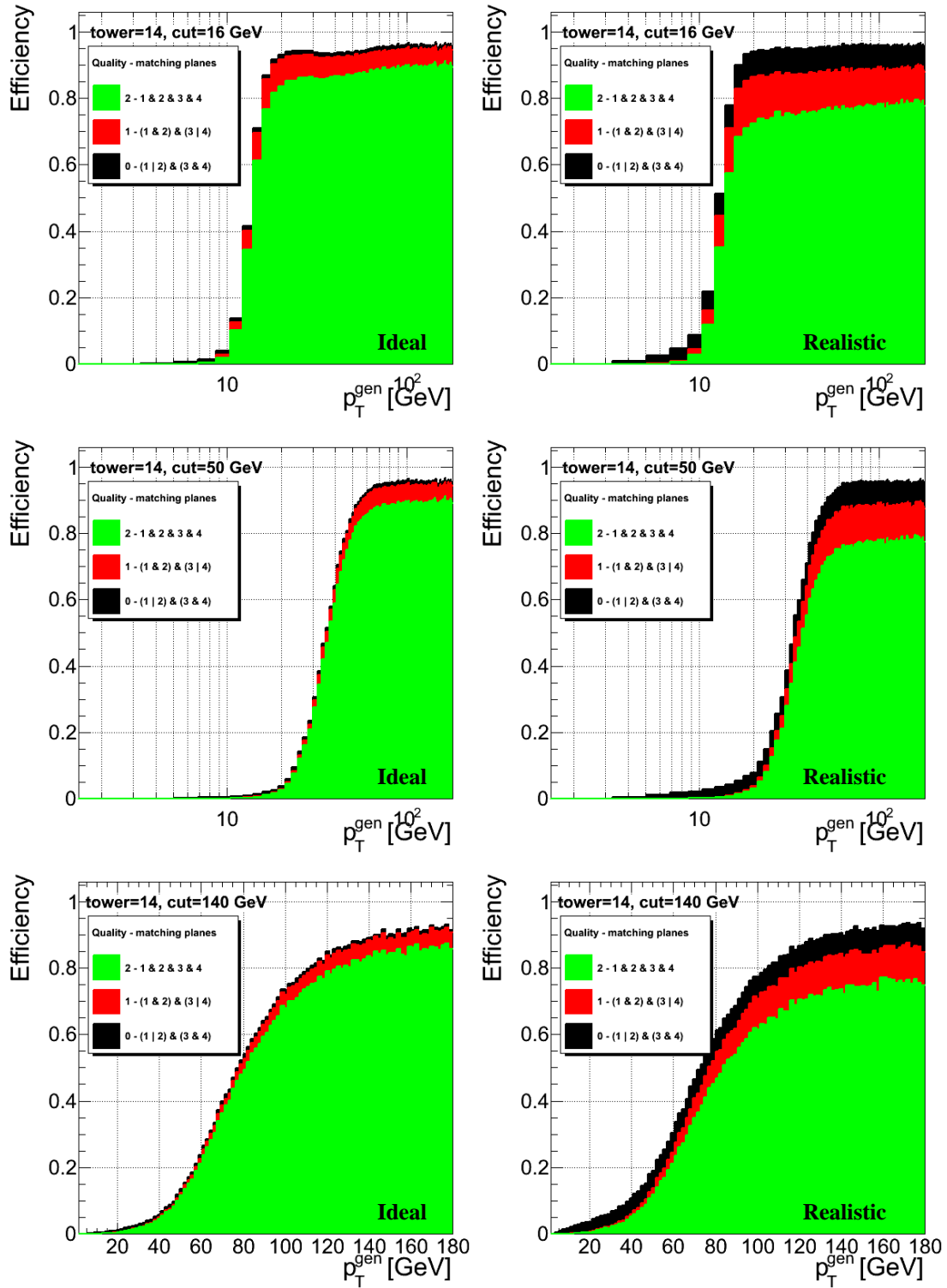


Figure 81: L1 GEM+RPC trigger efficiency curves in trigger tower 14 for $2\times$ geometry. Rows correspond to 3 different p_T thresholds of 16, 50, and $140 \frac{\text{GeV}}{c}$, respectively. Left column shows results for ideal chamber model, right for realistic chamber model.

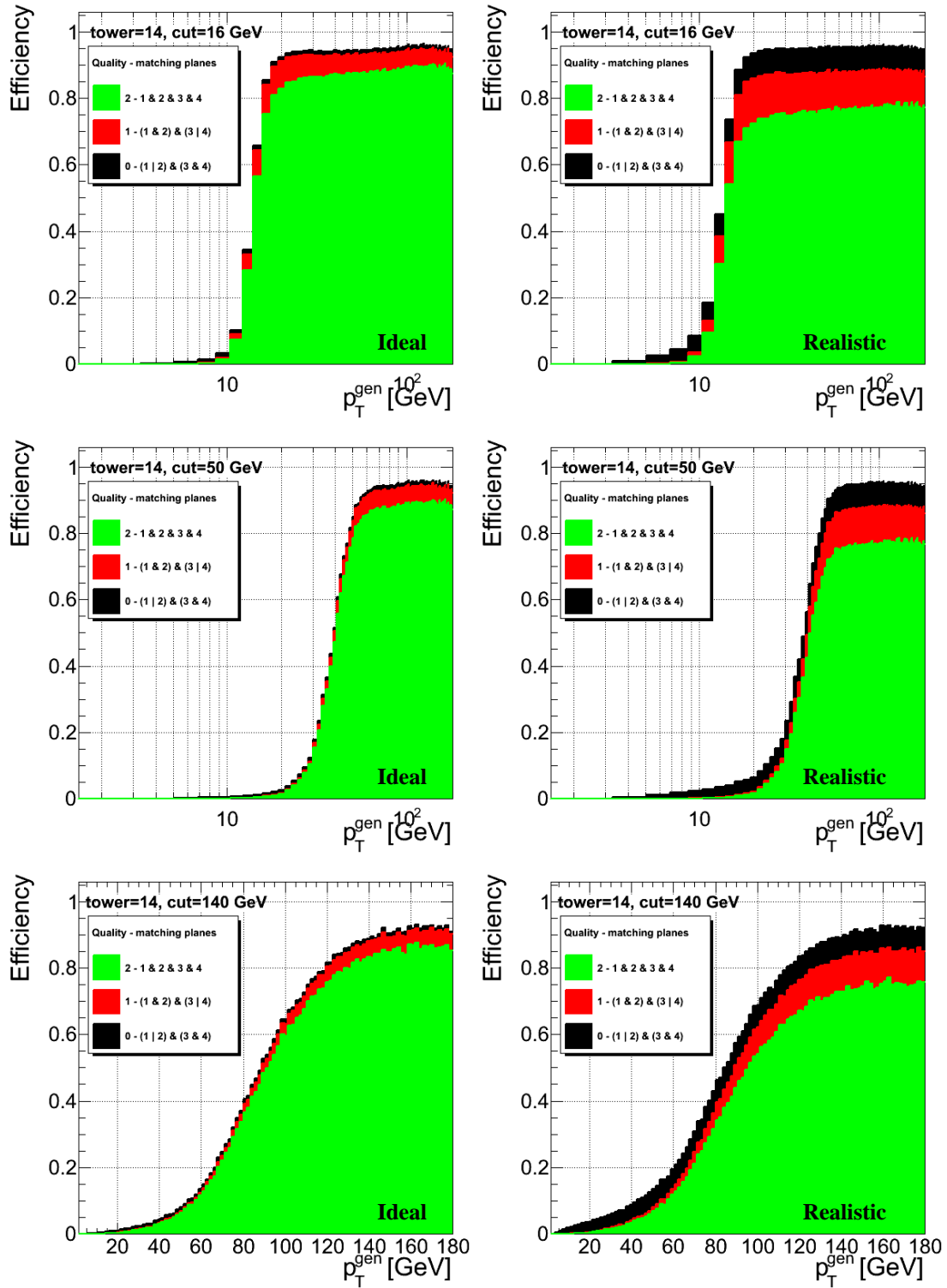


Figure 82: L1 GEM+RPC trigger efficiency curves in trigger tower 14 for $4 \times$ geometry. Rows correspond to 3 different p_T thresholds of 16, 50, and $140 \frac{\text{GeV}}{c}$, respectively. Left column shows results for ideal chamber model, right for realistic chamber model.

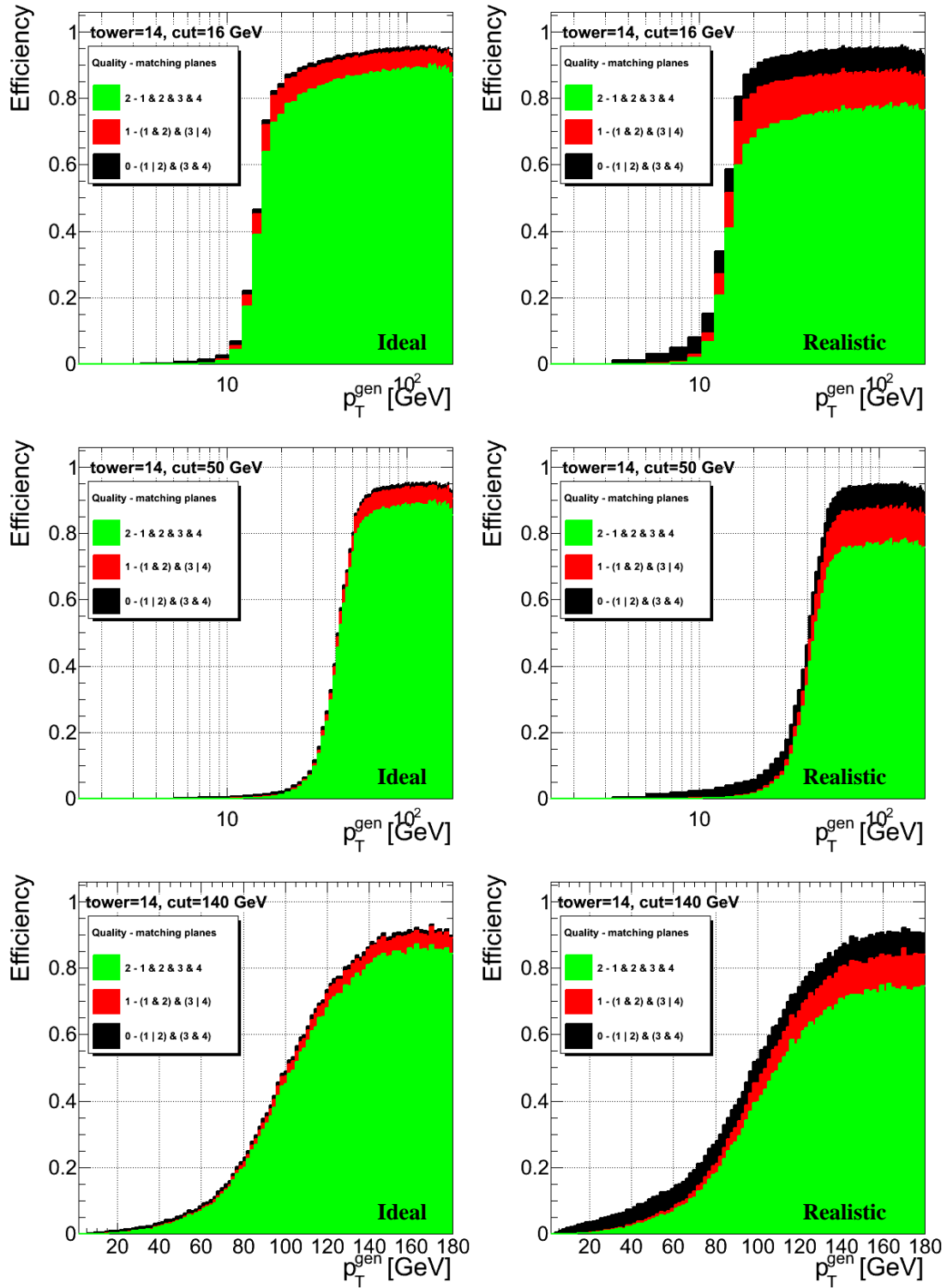


Figure 83: L1 GEM+RPC trigger efficiency curves in trigger tower 14 for $8 \times$ geometry. Rows correspond to 3 different p_T thresholds of 16, 50, and $140 \frac{\text{GeV}}{c}$, respectively. Left column shows results for ideal chamber model, right for realistic chamber model.

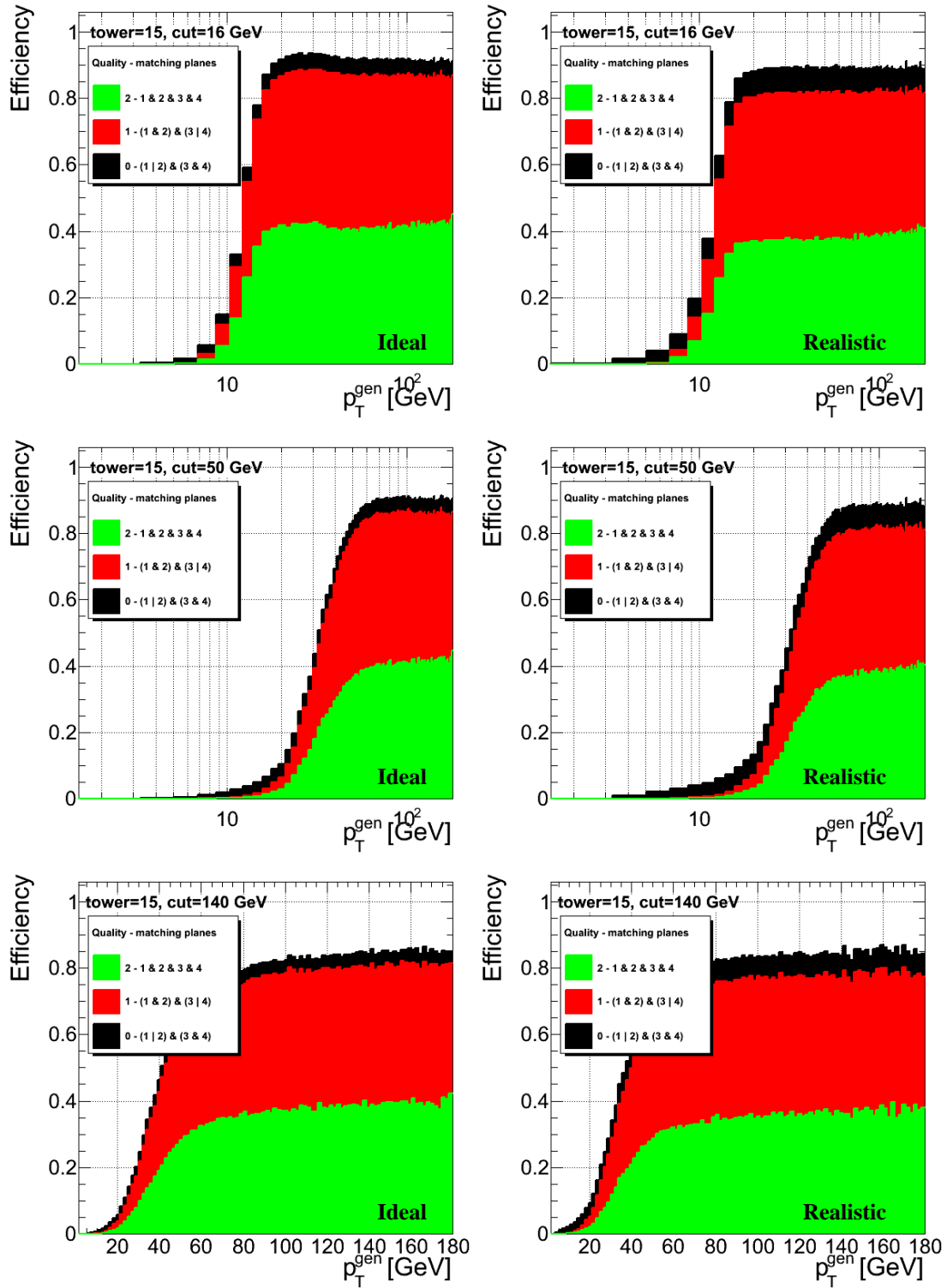


Figure 84: L1 GEM+RPC trigger efficiency curves in trigger tower 15 for base geometry. Rows correspond to 3 different p_T thresholds of 16, 50, and 140 $\frac{\text{GeV}}{c}$, respectively. Left column shows results for ideal chamber model, right for realistic chamber model.

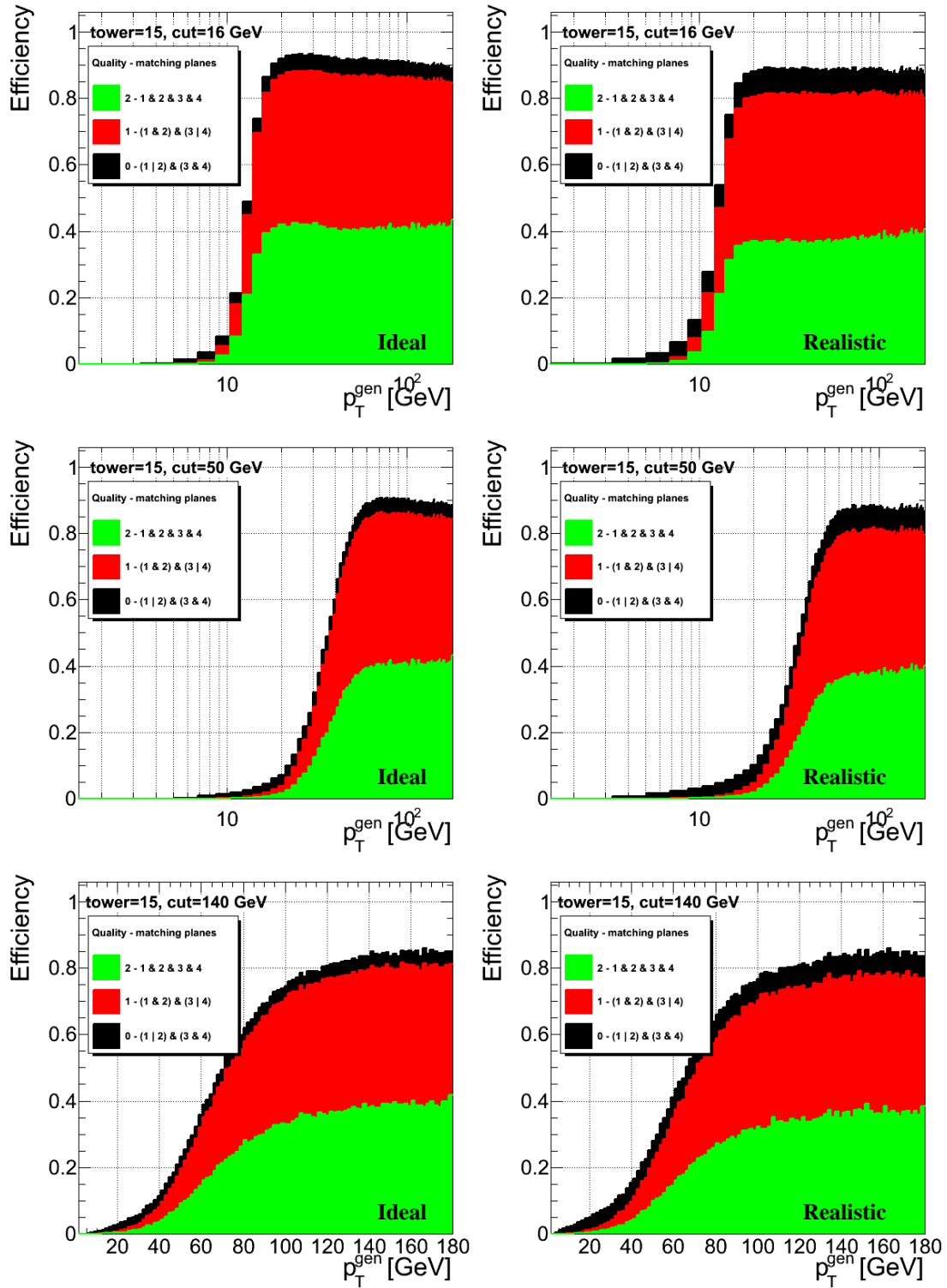


Figure 85: L1 GEM+RPC trigger efficiency curves in trigger tower 15 for $2 \times$ geometry. Rows correspond to 3 different p_T thresholds of 16, 50, and $140 \frac{\text{GeV}}{c}$, respectively. Left column shows results for ideal chamber model, right for realistic chamber model.

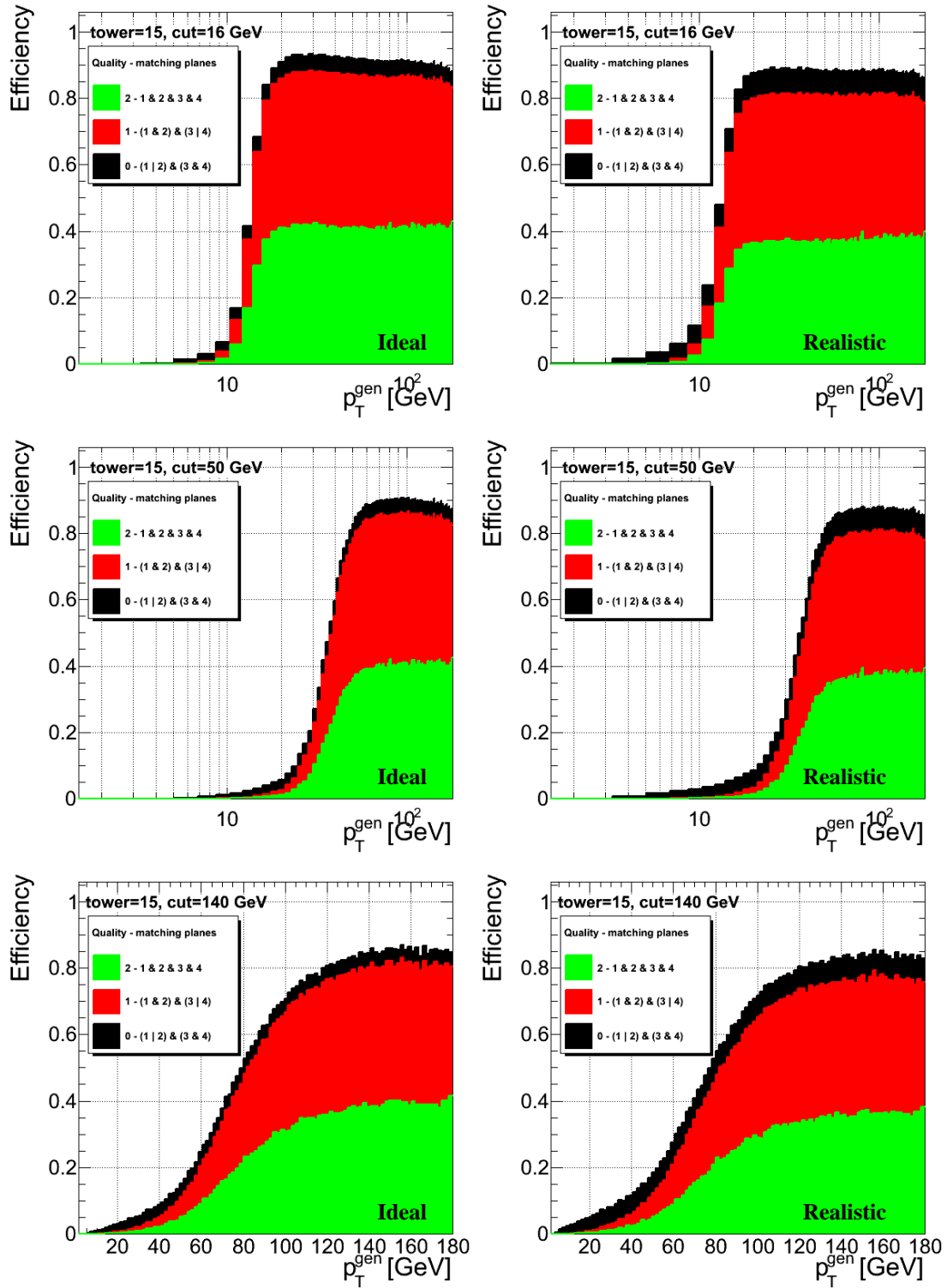


Figure 86: L1 GEM+RPC trigger efficiency curves in trigger tower 15 for $4\times$ geometry. Rows correspond to 3 different p_T thresholds of 16, 50, and $140 \frac{\text{GeV}}{c}$, respectively. Left column shows results for ideal chamber model, right for realistic chamber model.

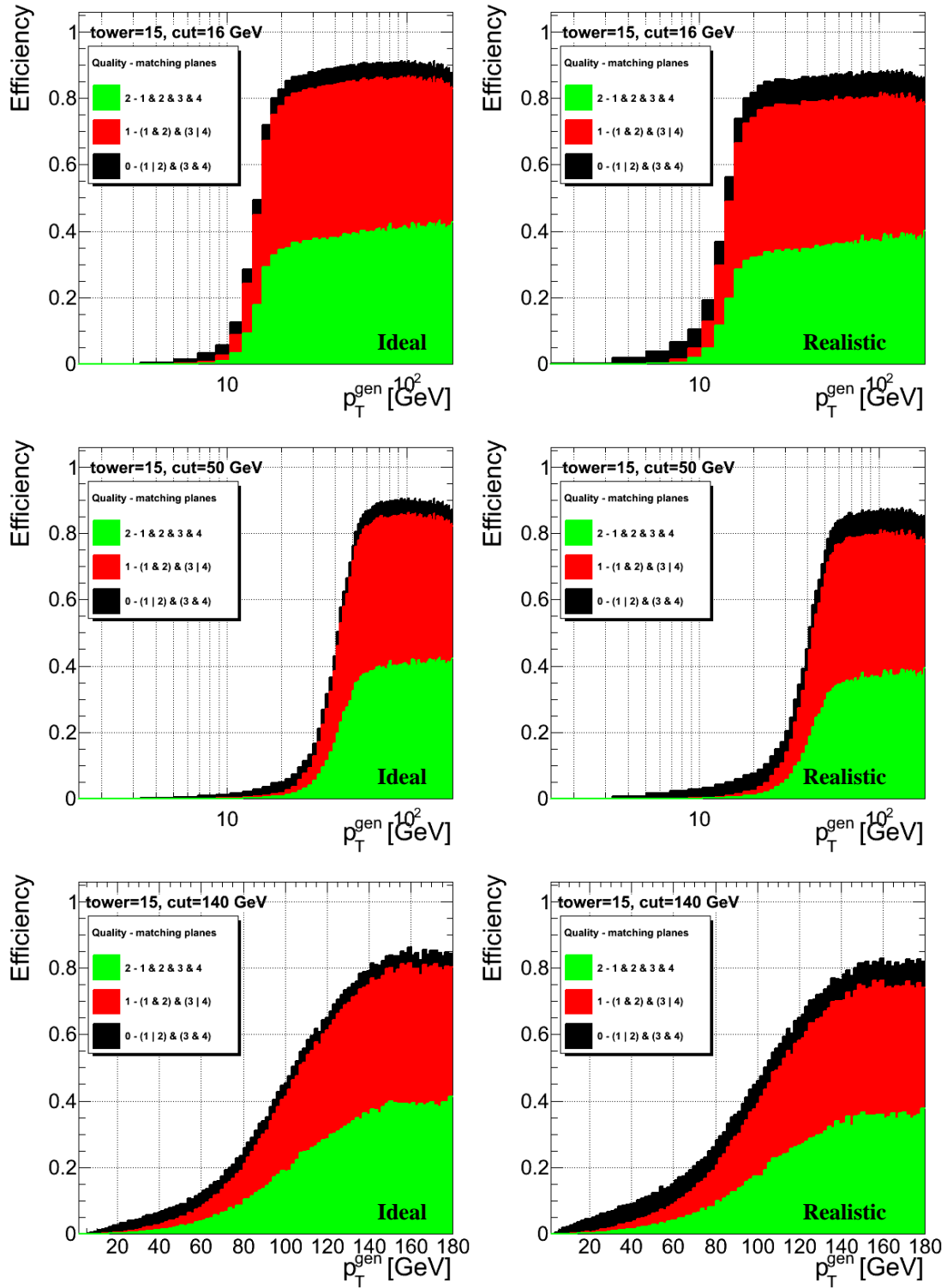


Figure 87: L1 GEM+RPC trigger efficiency curves in trigger tower 15 for $8 \times$ geometry. Rows correspond to 3 different p_T thresholds of 16, 50, and $140 \frac{\text{GeV}}{c}$, respectively. Left column shows results for ideal chamber model, right for realistic chamber model.

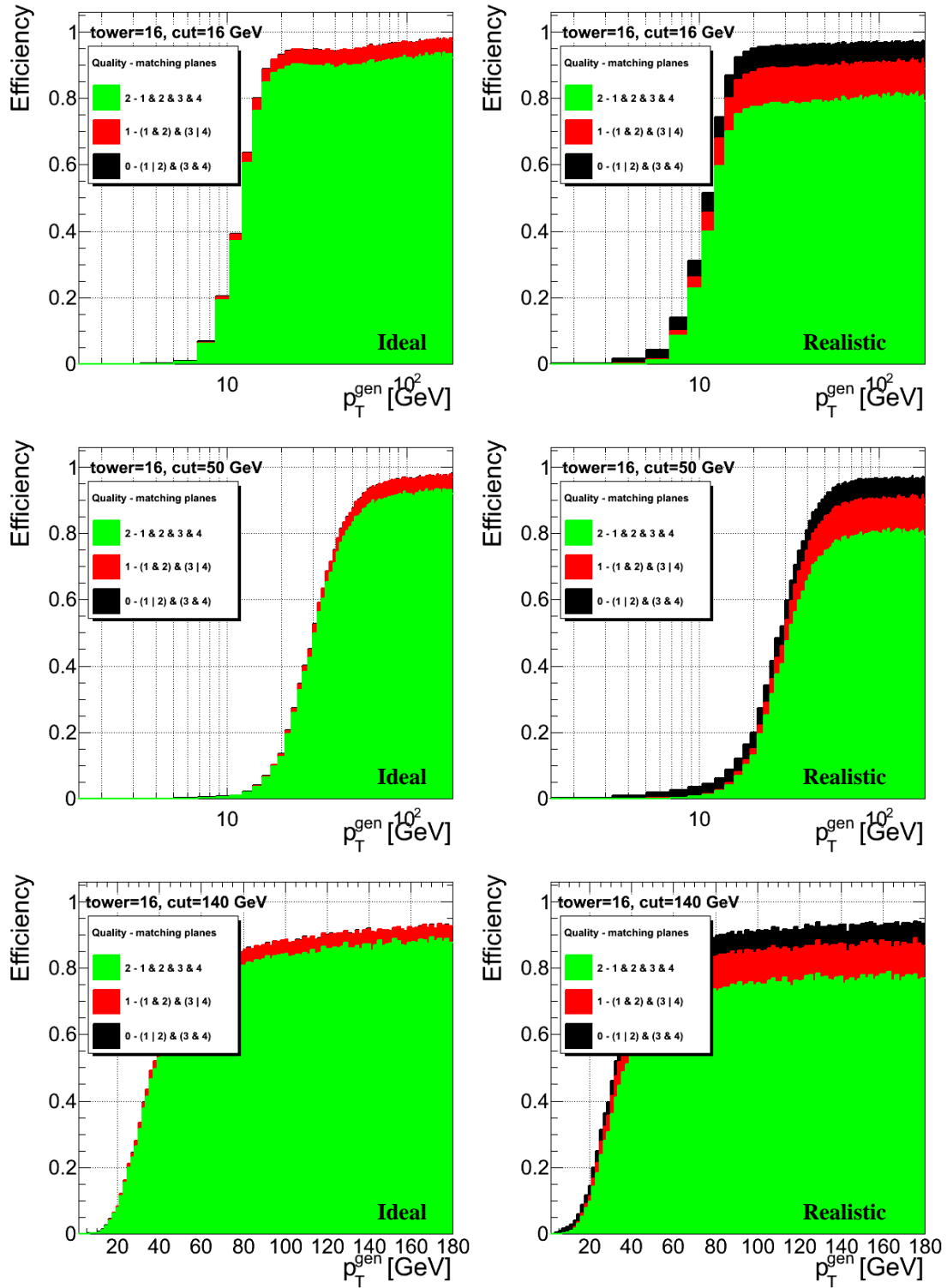


Figure 88: L1 GEM+RPC trigger efficiency curves in trigger tower 16 for base geometry. Rows correspond to 3 different p_T thresholds of 16, 50, and 140 $\frac{\text{GeV}}{c}$, respectively. Left column shows results for ideal chamber model, right for realistic chamber model.

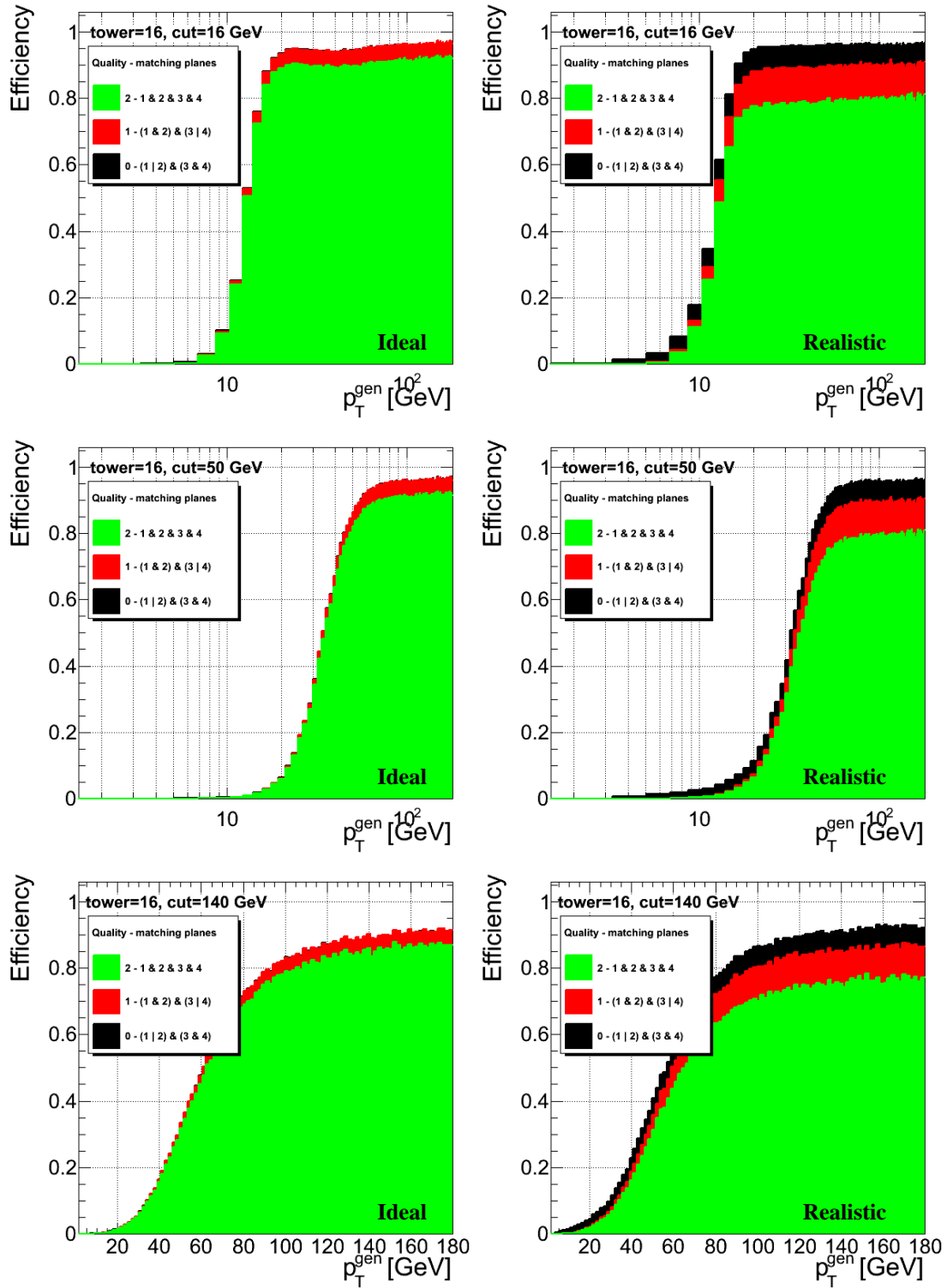


Figure 89: L1 GEM+RPC trigger efficiency curves in trigger tower 16 for $2\times$ geometry. Rows correspond to 3 different p_T thresholds of 16, 50, and $140 \frac{\text{GeV}}{c}$, respectively. Left column shows results for ideal chamber model, right for realistic chamber model.

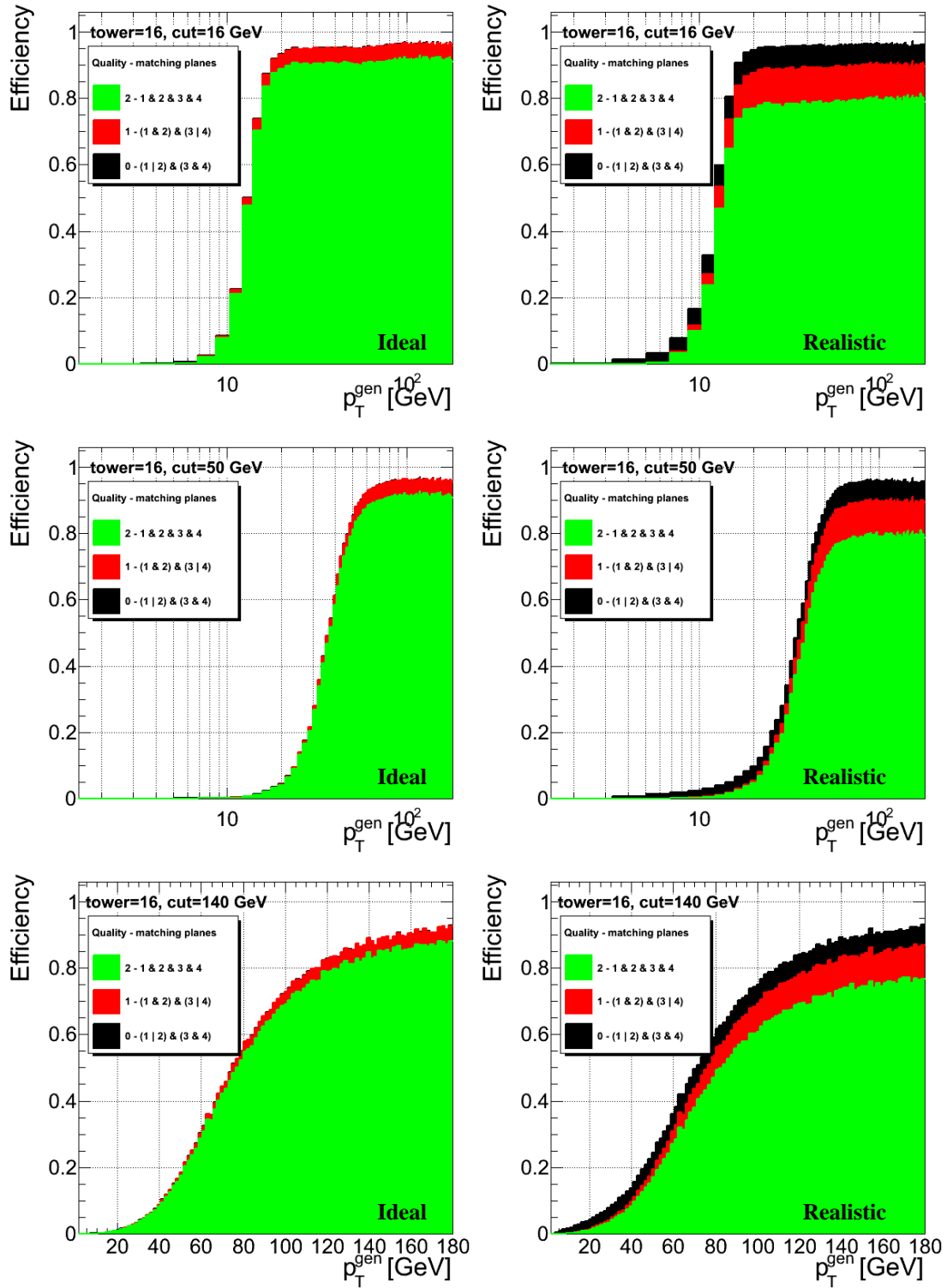


Figure 90: L1 GEM+RPC trigger efficiency curves in trigger tower 16 for $4\times$ geometry. Rows correspond to 3 different p_T thresholds of 16, 50, and $140 \frac{\text{GeV}}{c}$, respectively. Left column shows results for ideal chamber model, right for realistic chamber model.

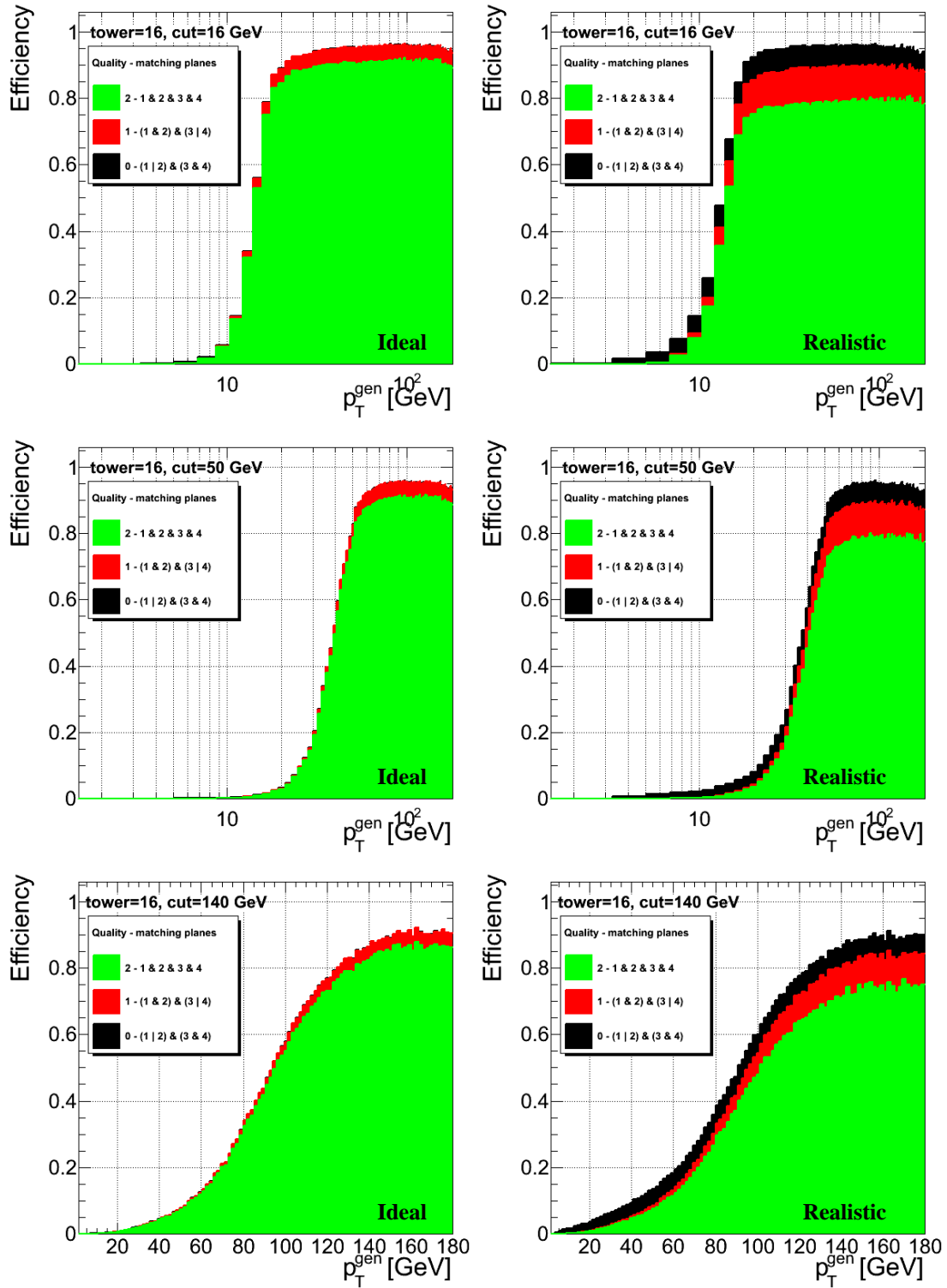


Figure 91: L1 GEM+RPC trigger efficiency curves in trigger tower 16 for $8 \times$ geometry. Rows correspond to 3 different p_T thresholds of 16, 50, and $140 \frac{\text{GeV}}{c}$, respectively. Left column shows results for ideal chamber model, right for realistic chamber model.